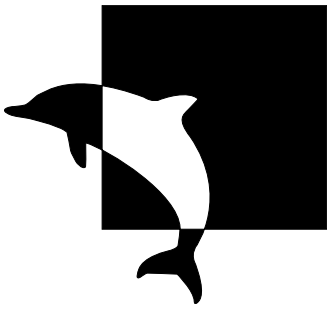

UNIVERSITY OF SOUTHAMPTON

FACULTY OF ENGINEERING, SCIENCE AND MATHEMATICS

OPTOELECTRONICS RESEARCH CENTRE

Frequency-Resolved Optical Gating in Periodically-Poled Lithium Niobate Waveguide Devices

Jerry Prawiharjo

A thesis submitted for the degree of
Doctor of Philosophy

September 2005

UNIVERSITY OF SOUTHAMPTON

ABSTRACT

FACULTY OF ENGINEERING, SCIENCE AND MATHEMATICS
OPTOELECTRONICS RESEARCH CENTRE

Doctor of Philosophy

Frequency-Resolved Optical Gating in Periodically-Poled Lithium Niobate Waveguide Devices

by Jerry Prawiharjo

Frequency-Resolved Optical Gating (FROG) is a well-established and widely-employed technique for the intensity and phase characterisation of ultrashort optical pulses. Essentially, FROG involves mixing an ultrashort optical pulse with its time-delayed replica, or another pulse, in a nonlinear material or device to yield a two dimensional data set called a spectrogram, from which the electric field of the ultrashort pulse can be retrieved by an iterative algorithm. The most commonly used configuration is based on second-order nonlinear interactions in bulk materials, mainly because of its high efficiency compared to other schemes based on third-order nonlinear interactions.

Although the FROG technique itself is extremely versatile, its sensitivity is limited by the efficiency of the nonlinear optical interactions it relies upon. This restricts its suitability for certain applications, such as optical telecommunications, in which the durations of the pulses used might be of the order a few picoseconds and the powers required are relatively low (milliwatt regime). Periodically-poled Lithium Niobate (PPLN) waveguides are attractive for the implementation of FROG devices. The guided-wave geometry provides higher efficiency due to tight optical confinements and long interaction lengths, whilst the PPLN structure gives access to the Lithium Niobate highest nonlinear coefficient and guarantees a wider wavelength operation range by proper engineering of the grating period.

The research work in this thesis led to the first successful implementation of an integrated Lithium Niobate for the FROG device, based on sum-frequency generation. We demonstrated simultaneous complete characterisation of two ultrashort pulses of durations 4-25 ps in the 1.55 μm-band with a coupled energy of 430 fJ in a 26 mm long PPLN waveguide device. The temporal walk-off between the interacting pulses in this interaction resulted in an acceptance bandwidth of 0.75 nm, limiting the measurable pulse duration to $\sim$ 4.5 ps. In order to overcome this limitation, we proposed and demonstrated a novel FROG configuration based on cascaded second-harmonic and difference-frequency generations. Theoretical and numerical analyses of this configuration revealed its robustness against the temporal walk-off effect, resulting in improved temporal resolutions. This was experimentally verified by characterising a 2.1 ps pulse train with a coupled average power (energy) of 72 μW (29 fJ) in the PPLN waveguide device previously mentioned.

Contents

Declaration of Authorship

I, Jerry Prawiharjo, declare that the thesis entitled:
Frequency-Resolved Optical Gating in Periodically-Poled Lithium Niobate Waveguide Devices
and the work presented in it are my own. I confirm that:

- this work was done wholly or mainly while in candidature for a research degree at this University;
- where any part of this thesis has previously been submitted for a degree or any other qualification at this University or any other institution, this has been clearly stated;
- where I have consulted the published work of others, this is always clearly attributed;
- where I have quoted from the work of others, the source is always given. With the exception of such quotations, this thesis is entirely my own work;
- I have acknowledged all main sources of help;
- where the thesis is based on work done by myself jointly with others, I have made clear exactly what was done by others and what I have contributed myself;
- parts of this work have been published as:
    1. J. Prawiharjo, F. Parmigiani, K. Gallo, P. Petropoulos, N. G. R. Broderick, and D. J. Richardson, (2005). To appear in Optics Letters.
    2. J. Prawiharjo, K. Gallo, N. G. R. Broderick, and D. J. Richardson, Journal of the Optical Society of America B **22**(9), 1985–1993 (2005).
    3. J. Prawiharjo, K. Gallo, B. C. Thomsen, M. A. F. Roelens, P. J. Almeida, N. G. R. Broderick, and D. J. Richardson, IEEE Photonics Technology Letters **17**(4), 849–851 (2005).

Signed:

Date: October 2, 2005

Acknowledgements

It has been a great honour for me to do my Ph.D in the ORC for the past three years. I have been very fortunate to work with several bright, motivated, and talented people in due course. Without the help of these people, my sole hardwork would have not been sufficient to reach this point. I believe that it would be impossible to express my sincere gratitude on this page, but I will attempt, to the very least, by saying a few words here.

It has been a wonderful experience to work with my co-supervisor Katia Gallo. She has not only been a fine tutor over the past three years, but also a good friend. Academically, I have learned a lot from her wealthy knowledge and distinctive skill, as well as her contagious enthusiasm and persistence in research. She is a friend with a unique and strong personality, and also a good source of free *tiramisu*.

My supervisor Neil Broderick has helped me in some ways. I am grateful for his loan of computing resources, and for his suggestions that made my thesis a better one. Despite of his busy schedule, Professor David Richardson always managed to allocate time helping me in many ways. I appreciate his willingness to help me finalising my journal as well as conference papers. His occasional visits to the laboratory helped boosting my and my fellow students' morales.

My life in the telecom laboratory would have been very difficult without the help from the post-docs: Benn Thomsen and Periklis Petropoulos, and from my fellow students: Francesca Parmigiani, Michaël Roelens, and Paolo Almeida. I miss our occasional "fights" for shared equipments, and the times when we had to pull all nighters to beat the deadlines.

I would like to thank Professors Peter Smith and John Dudley who served as the examiners for my viva voce. I appreciate their constructive suggestions and comments.

Eve Smith has been very helpful with the administrations, from the time before I arrived at the ORC, to the very end of my Ph.D. Neil Sessions provided a great support in the cleanroom while I was working there.

I had occasional escapes from my routine day to day research life for three years to the Southampton judo club. I always looked forward for the Sunday sessions with Christophe Codemard, Derek and Sarah Hopkins. I also have to mention people from the regular Tuesday sessions: Gary Hill, Alun Coker, and Owen Tutty. I improved my judo thanks to all of them.

Finally, the most important people in my life are my parents and my brothers. They have been very supportive throughout my life, and have constantly given me encouragements. I am sure they are proud of what I have become. I dedicated my thesis to them.

As a last note, I would like to thank Kubo Tite and Kishimoto Masashi for my weekly dose of Bleach and Naruto, respectively.

Abbreviations

AC	Autocorrelation
ASE	Amplified Spontaneous Emission
BPF	Band-Pass Filter
DFG	Difference-Frequency Generation
EAM	Electro-Absorption Modulator
EDFA	Erbium-Doped Fibre Amplifier
EOM	Electro-Optics Modulator
FDPM	Frequency-Domain Phase Measurement
FPC	Fibre Polarisation Controller
FRAC	Fringe-Resolved Autocorrelation
FROG	Frequency-Resolved Optical Gating
FT	Fourier Transform
FWHM	Full-Width at Half-Maximum
FWM	Four-Wave Mixing
GS-DFB	Gain-Switched Distributed Feedback
IWKB	Inverse-Wentzel-Kramers-Brillouin
LHS	Left-Hand-Side
OPA	Optical Parametric Amplification
OPO	Optical Parametric Oscillation
OSA	Optical Spectrum Analyser
PCGP	Principal Component Generalised Projection
PE	Proton Exchange
PPLN	Periodically-Poled Lithium Niobate
QPM	Quasi-Phase-Matching
RHS	Right-Hand-Side
SF	Sum-Frequency
SFG	Sum-Frequency Generation
SH	Second-Harmonic
SHG	Second-Harmonic Generation
SMF	Single-Mode Fibre
SOA	Semiconductor Optical Amplifier
SPIDER	Spectral Phase Interferometry for Direct Electric-Field Reconstruction
TDM	Time-Division Multiplexing
TL	Transform-Limited
STRUT	Spectrally and Temporally Resolved Upconversion Technique
SVD	Singular Value Decomposition

TASC	Temporal Analysis of Spectral Components
WDM	Wavelength-Division Multiplexing
XFROG	Cross-correlation Frequency-Resolved Optical Gating

Chapter 1

Introduction

1.1 Motivation

The rapid advance and tremendous progress of ultrafast optics over the past three decades has had a significant impact in both fundamental and applied studies. The typical time scale of ultrashort optical pulses makes them an ideal tool for the investigation of various processes with similar time scales (picoseconds to femtoseconds), e.g. ultrafast spectroscopy. Ultrafast spectroscopy has been used to study diverse processes, such as the motion of electrons, molecular vibrations, chemical reactions, phase changes in condensed matter, excitation across bandgaps, phonon dynamics in solid-state materials, photosynthesis, and human vision.[1] The uses of ultrafast optical pulses are not limited to the studies of ultrafast events in basic research. There have also been numerous practical applications, such as ultrafast imaging to provide non-invasive *in vivo* data,[2,3] quantum control of a material state,[4] coherent control for selective stimulation of chemical reactions,[5] and the realisation of femtosecond

Perhaps the most important use of ultrashort optical pulses in this multimedia era is in the realisation of ultrahigh capacity optical telecommunications systems by permitting faster data transfer. Optical time-division multiplexing (TDM)[7,8] is not the only system that heavily utilises ultrashort optical pulses, since recently wavelength-division multiplexing (WDM)[9] systems have also started to move toward higher bit rates.[10,11]

The ability to concentrate the light energy into a very short temporal span can yield an extremely high intensity at the centre of an ultrashort laser pulse. Such a high intensity gives access to a variety of nonlinear interactions, which can be used for micromachining,[12] writing waveguides[13] for three-dimensional integrated optics structures,[14] surgical applications,[15] as well as many others.

This tremendous progress in ultrafast optics has been driven by the maturing technology of ultrashort optical pulse generation. Essential to this are the ultrafast pulsed laser sources which, may or may not be accompanied by a subsequent pulse compression stage. The vast majority of such sources rely on a *mode-locking* mechanism,[1,16,17] whilst alternative approaches include both gain-switching[18,19] and external modulations of a continuous wave laser source.[20] Shorter pulses can be readily obtained from these sources by means of compression schemes.[21–23] These technologies have made the generation of ultrashort pulses in laboratories routine.

The sole ability to generate ultrashort optical pulses is not sufficient. The precise knowledge of the amplitude and phase distributions across an ultrashort pulse is crucial for several reasons. First and foremost, the detailed knowledge of the pulse properties is necessary to understand and optimise its source. Secondly, ultrafast spectroscopy experiments depend on the ability to precisely characterise the pulses.[24] Thirdly, some applications, such as quantum control of a material state[4] and coherent control for selective stimulations of chemical reactions,[5] rely on the ability to tailor the shape of the ultrashort pulses. Finally, in optical telecommunications systems, the pulse duration determines the upper limit of the bit rate, whilst the spectral content determines the maximum transmission length before the fibre dispersion distorts the pulse. Therefore, knowledge of both is necessary for designing a system.

The characterisation of ultrashort optical pulses, that is, the measurement of their instantaneous electric field is nontrivial. The difficulties in measuring the field distribution are, ironically, mainly caused by their duration which is much lower than the temporal resolution of standard electronic equipment. Furthermore, the direct measurement of their phase seemed beyond reach, since detectors at optical frequencies are only sensitive to the photon flux, i.e. intensity, such detectors are known as square-law detectors. The main tool for measuring the field distribution in the time domain has, for almost four decades, been the second-order intensity autocorrelator,[25] mainly due to the lack of better methods. In the frequency domain, the spectrometer measures the spectral density of ultrashort optical pulses but, unfortunately, not the instantaneous frequency across the pulse.

A great deal of effort was spent on solving the problem of ultrashort optical pulse characterisation resulting in three well-known approaches for the complete characterisation of ultrashort optical pulses: spectrographic, tomographic, and interferometric.[26,27]

Tomographic techniques[28] are the least appealing among the three, because of difficulties in creating the apparatus and the numerous two-dimensional data sets that must be collected. Nevertheless, simplified versions with some restrictions were demonstrated.[29,30] Interferometric techniques, such as spectral phase interferometry for direct electric field reconstruction (SPIDER)[31,32] and, more generally, spectral shearing interferometry,[33] measure the phase difference between a pulse and its spectrally sheared replica, resulting in a one-dimensional data set, which can be directly inverted to yield the electric field of an ultrashort optical pulse. The simple and direct inversion routine offered by interferometric techniques is at the expense of the experimental setup simplicity. Spectrographic techniques are the most promising approach for the complete characterisation of ultrashort optical pulses. Spectrographic techniques measure a set of two-dimensional data and employ an iterative algorithm to retrieve the ultrashort optical pulse electric fields. Several variants have been demonstrated, such as frequency-domain phase measurements (FDPM),[34] frequency-resolved optical gating (FROG),[35–37] spectrally and temporally resolved upconversion technique (STRUT),[38] and temporal analysis of spectral components (TASC).[39] The attractiveness of spectrographic techniques lies in the simplicity of their practical implementation. In addition, currently developed algorithms[40] and greater available computational power have overcome the drawback of the iterative algorithm, making real-time inversion possible.

The most popular among spectrographic techniques is FROG. The versatility, experimental simplicity, reliability, and robustness of FROG have made it a well-established and widely-employed ultrashort pulse characterisation technique. For example, FROG has been used to characterise ultrashort pulses in the near single-cycle limit,[41] to characterise complex supercontinuum pulses from a microstructure-fibre,[42] and to verify a theoretical model of ultrashort pulses creation.[43] In the recent years, the use of FROG in optical telecommunications research has increased quite significantly, including characterisation of ultrafast laser sources,[44–47] characterisation and optimisation of external modulators,[48,49] studies of pulse propagation in optical fibres,[50,51] and measurements of fibre properties.[52]

More precisely, FROG essentially involves spatially mixing an ultrashort pulse with its time-delayed replica, or another pulse, in a (usually) instantaneous nonlinear material or device, to yield a two-dimensional data set called a spectrogram, from which the electric-field of the ultrashort pulse can be retrieved with an iterative algorithm, as in

any other spectrographic techniques. Hence, the FROG performance is governed by the nonlinear interactions it relies on. In particular, FROG sensitivity is limited by the efficiency of nonlinear interactions, whilst its temporal resolution is determined by the acceptance bandwidth of the device.

Various nonlinear interactions have been used for FROG measurements, including second-order nonlinear interactions, such as second-harmonic generation (SHG),[53,54] and third-order nonlinear interactions such as polarisation gate,[35] self-diffraction,[36] transient grating,[55] and third-harmonic generation.[56] Since second-order nonlinear interactions are more efficient than third-order ones, SHG FROG is the most sensitive compared to the other standard configurations previously mentioned.

Nevertheless, high sensitivity FROG configurations in optical fibres[57,58] and in semiconductor optical amplifiers (SOA)[59] have been reported recently. Although these configurations are based on third-order nonlinear interactions, efficiency enhancement provided by the guided-wave geometries results in a higher efficiency compared to the second-order interactions in bulk materials. Guided-wave geometries such as fibres and waveguides prevent beam diffraction by providing tight optical confinement over a long interaction length. This fact suggests that higher sensitivity could be achieved by implementing a guided-wave geometry in second-order nonlinear materials. It is worth noting that an extremely sensitive characterisation technique in a linear device has been demonstrated recently.[60] Since this techniques requires the availability of synchronised short electrical pulses, its application is thus quite restricted.

Periodically-poled $LiNbO_3$ (PPLN) waveguide devices are of particular interest since they exhibit extremely high efficiencies for second-order nonlinear interactions.[61] Periodic poling of $LiNbO_3$ gives access to the highest nonlinear coefficient of $LiNbO_3$, and allows a broad tunable range by proper design of the structure, as described in detail in Chapter 3. Moreover, waveguides in this structure provide efficiency enhancement up to two orders of magnitude compared to bulk devices . Such high efficiency has been used to realise highly efficient optical frequency mixers in telecommunications systems.[62,63] In addition, sensitive intensity autocorrelations have been performed using such devices.[64]

The work in this thesis led to the first demonstration of the implementation of FROG technique in a QPM $LiNbO_3$ waveguide.[65] Efficiency improvement achieved by using guided-wave geometries instead of bulk materials is only significant in long devices.

Unfortunately, as the interaction length is increased, the acceptance bandwidth of the nonlinear interaction decreases, hence limiting the temporal resolution. Therefore, a trade-off between sensitivity and temporal resolution needs to be established. Engineering the poling structure to produce aperiodic gratings[66,67] can be used to broaden the acceptance bandwidth, providing a means to improve this trade-off. However, the complexities in designing and fabricating aperiodic gratings are significant, resulting in a more difficult implementation for the FROG technique.[67] A novel configuration based on cascaded second-order nonlinear interactions, offering better sensitivity and temporal resolution, is also a result of the work in this thesis. This novel configuration is theoretically and numerically analysed,[68] as well as demonstrated experimentally.[69]

1.2 Outline of This Thesis

This thesis is organised as follows. Chapter 2 reviews the fundamentals of FROG. A fundamental problem for the characterisation of ultrashort optical pulses is presented, along with the general concept of the FROG technique as a solution. Specific configurations based on second-order nonlinear interactions such as SHG FROG, cross-correlation FROG (XFROG) and blind-FROG will be discussed.

Chapter 3 reviews the basic theoretical framework of SHG, the simplest second-order nonlinear interaction. Differences and similarities between SHG interactions in bulk materials and waveguide devices will be highlighted here. This theoretical framework should serve as a foundation to understand more complex second-order nonlinear interactions and the experimental results presented in the subsequent chapters.

Chapter 4 presents the properties of the QPM $LiNbO_3$ waveguide device used throughout this thesis. The characterisation of its linear properties, including transverse mode profiles and propagation losses, is presented. Nonlinear properties define the working region in terms of wavelength and also the efficiency of the device. Characterisations of nonlinear properties were done via second-harmonic and sum-frequency generations. A brief overview of the fabrication is also presented in this chapter.

Chapter 5 presents the theory of parametric interactions of ultrashort optical pulses. The propagation of ultrashort pulses in a $LiNbO_3$ waveguide is described here, and ultrashort pulse SHG is theoretically and numerically analysed. These analyses are extended to sum- and difference-frequency generation (SFG and DFG), as well as the more complex cascaded second-order nonlinear interactions. The analyses in this chapter will be

used to understand the basics of the FROG technique.

Chapter 6 reports the first implementation of FROG technique in a QPM $LiNbO_3$ waveguide device. Description of the experiments along with the results will be given. Limitations of this technique will also be reported.

Chapter 7 proposes a novel FROG configuration based on cascaded second-order interactions. Theoretical and numerical analyses of this configuration are provided, as well as a report on the experimental realisation of this configuration.

Finally, the work of this thesis will be concluded in Chapter 8 along with a discussion on the direction of future work.

References

[1] J. C. Diels and W. Rudolph, *Ultrashort Laser Pulse Phenomena* (Academic Press, San Diego, 1996).

[2] J. Squier and M. Müller, "High Resolution Nonlinear Microscopy: A Review of Sources and Methods for Achieving Optimal Imaging," Review of Scientific Instruments **72**(7), 2855–2867 (2001).

[3] A. F. Fercher, W. Drexler, C. K. Hitzenberger, and T. Lasser, "Optical Coherence Tomography - Principles and Applications," Reports on Progress in Physics **66**(2), 239–303 (2003).

[4] B. Kohler, V. V. Yakovlev, J. Che, J. L. Krause, M. Messina, and K. R. Wilson, "Quantum Control of Wave Packet Evolution With Tailored Femtosecond Pulses," Physical Review Letters **74**(17), 3360–3363 (1995).

[5] A. Assion, T. Baumert, M. Bergt, T. Brixner, B. Kiefer, V. Seyfried, M. Strehle, and G. Gerber, "Control of Chemical Reactions by Feedback-Optimized Phase-Shaped Femtosecond Laser Pulses," Science **282**, 919–922 (1998).

[6] M. Lai, J. C. Diels, and M. L. Dennis, "Nonreciprocal Measurements in Femtosecond Ring Lasers," Optics Letters **17**(21), 1535–1537 (1992).

[7] S. Kawanishi, "Ultrahigh-Speed Optical Time-Division-Multiplexed Transmission Technology Based on Optical Signal Processing," IEEE Journal of Quantum Electronics **34**(11), 2064–2079 (1998).

[8] S. A. Hamilton, B. S. Robinson, T. E. Murphy, S. J. Savage, and E. P. Ippen, "100 Gb/s Optical Time-Division Multiplexed Networks," Journal of Lightwave Technology **20**(12), 2086–2100 (2002).

[9] S. J. B. Yoo, "Wavelength Conversion Technologies for WDM Network Applications," IEEE Journal of Lightwave Technology **14**(6), 955–966 (1996).

[10] W. S. Lee, B. Patel, Y. J. Zhu, C. Scahill, D. Watley, M. Jones, G. Pettitt, C. Fludger, B. Shaw, A. Hadjifotiou, and D. Way, "4 × 40 Gbit/s RZ ETDM Transmission Over 520 km of NDSF at 120 and 160 km Span Lengths with Raman Pre-Amplification," Electronics Letters **36**(8), 734–736 (2000).

[11] H. Ooi, K. Nakamura, Y. Akiyama, T. Takahara, T. Terahara, Y. Kawahata, H. Isono, and G. Ishikawa, "40-Gb/s WDM Transmission with Virtually Imaged Phased Array (VIPA) Variable Dispersion Compensators," Journal of Lightwave Technology **20**(12), 2196–2203 (2002).

[12] C. B. Schaffer, A. Brodeur, and E. Mazur, "Laser-Induced Breakdown and Damage in Bulk Transparent Materials Induced by Tightly Focused Femtosecond Laser Pulses," Measurement Science and Technology **12**(11), 1784–1894 (2001).

[13] K. M. Davis, K. Miura, N. Sugimoto, and K. Hirao, "Writing Waveguides in Glass with a Femtosecond Laser," Optics Letters **21**(21), 1729–1731 (1996).

[14] S. Nolte, M. Will, J. Burghoff, and A. Tünnermann, "Femtosecond Waveguide Writing: A New Avenue to Three-Dimensional Integrated Optics," Applied Physics A: Materials Science and Processing **77**(1), 109–111 (2003).

[15] S. Svanberg, "Some Applications of Ultrashort Laser Pulses in Biology and Medicine," Measurement Science and Technology **12**(11), 1777–1783 (2001).

[16] P. M. W. French, "Ultrafast Solid-State Lasers," Contemporary Physics **37**(4), 283–301 (1996).

[17] G. Steinmeyer, "A Review of Ultrafast Optics and Optoelectronics," Journal of Optics A: Pure and Applied Optics **5**, R1–R15 (2003).

[18] M. Nakazawa, K. Suzuki, and E. Yamada, "Femtosecond Optical Pulse Generation Using a Distributed-Feedback Laser Diode," Electronics Letters **26**(24), 2038–2040 (1990).

[19] R. P. Davey, K. Smith, R. Wyatt, D. L. Williams, M. J. Holmes, D. M. Pataca, M. L. Rocha, and P. Gunning, "Subpicosecond Pulse Generation from a 1.3 μm DFB Laser Gain-Switched at 1 GHz," Electronics Letters **32**(4), 349–351 (1996).

[20] M. Suzuki, H. Tanaka, K. Utaka, and Y. Matsushima, "Transform-Limited Optical Pulse Generation Up to 20-GHz Repetition Rate by a Sinusoidally Driven InGaAsP Electroabsorption Modulator," Journal of Lightwave Technology **11**(3), 468–472 (1993).

[21] L. F. Mollenauer, R. H. Stolen, J. P. Gordon, and W. J. Tomlinson, "Extreme Picosecond Pulse Narrowing by Means of Soliton Effect in Single-Mode Optical Fibers," Optics Letters **8**(5), 289–291 (1983).

[22] J. T. Ong, R. Takahashi, M. Tsuchiya, S. H. Wong, R. T. Sahara, Y. Ogawa, and T. Kamiya, "Subpicosecond Soliton Compression of Gain Switched Diode Laser Pulses Using an Erbium-Doped Fiber Amplifier," IEEE Journal of Quantum Electronics **29**(6), 1701–1707 (1993).

[23] M. Miyamoto, M. Tsuchiya, H. F. Liu, and T. Kamiya, "Generation of Ultrashort ($\sim$ 65 fs) Pulses from 1.55 μm Gain-Switched Distributed Feedback (DFB) Laser with Soliton Compression by Dispersion Arrangements," Japanese Journal of Applied Physics **35**(10B), L1330–L1332 (1996).

[24] P. Zhou, H. Schulz, and P. Kohns, "Atomic Spectroscopy with Ultrashort Laser Pulses Using Frequency-Resolved Optical Gating," Optics Communications **123**, 501–504 (1996).

[25] M. Maier, W. Kaiser, and J. Giordmaine, "Intense Light Bursts in the Stimulated Raman Effect," Physical Review Letters **17**(26), 1275–1277 (1966).

[26] I. A. Walmsley and V. Wong, "Characterization of the Electric Field of Ultrashort Optical Pulses," Journal of the Optical Society of America B **13**(11), 2453–2463 (1996).

[27] C. Iaconis, V. Wong, and I. A. Walmsley, "Direct Interferometric Techniques for Characterizing Ultrashort Optical Pulses," IEEE Journal of Selected Topics in Quantum Electronics **4**(2), 285–294 (1998).

[28] M. Beck, M. G. Raymer, I. A. Walmsley, and V. Wong, "Chronocyclic Tomography for Measuring the Amplitude and Phase Structure of Optical Pulses," Optics Letters **18**(23), 2041–2043 (1993).

[29] H. R. Lange, M. A. Franco, J. F. Ripoche, B. S. Prade, P. Rousseau, and A. Mysyrowicz, "Reconstruction of the Time Profile of Femtosecond Laser Pulses Through Cross-Phase Modulation," IEEE Journal of Selected Topics in Quantum Electronics **4**(2), 295–300 (1998).

[30] C. Dorrer and I. Kang, "Complete Temporal Characterization of Short Optical Pulses by Simplified Chronocyclic Tomography," Optics Letters **28**(16), 1481–1483 (2003).

[31] C. Iaconis and I. A. Walmsley, "Spectral Phase Interferometry for Direct Electric-Field Reconstruction of Ultrashort Optical Pulses," Optics Letters **23**(10), 792–794 (1998).

[32] C. Iaconis and I. A. Walmsley, "Self-Referencing Spectral Interferometry for Measuring Ultrashort Optical Pulses," IEEE Journal of Quantum Electonics **35**(4), 501–509 (1999).

[33] V. Wong and I. A. Walmsley, "Analysis of Ultrashort Pulse-Shape Measurement Using Linear Interferometers," Optics Letters **19**(4), 287–289 (1994).

[34] J. L. A. Chilla and O. E. Martinez, "Direct Determination of the Amplitude and the Phase of Femtosecond Light Pulses," Optics Letters **16**(1), 39–41 (1991).

[35] R. Trebino and D. J. Kane, "Using Phase Retrieval to Measure the Intensity and Phase of Ultrashort Pulses: Frequency-Resolved Optical Gating," Journal of the Optical Society of America A **10**(5), 1101–1111 (1993).

[36] D. J. Kane and R. Trebino, "Characterization of Arbitrary Femtosecond Pulses Using Frequency-Resolved Optical Gating," IEEE Journal of Quantum Electronics **29**(2), 571–579 (1993).

[37] R. Trebino, K. W. DeLong, D. N. Fittinghoff, J. N. Sweetser, M. A. Krumbügel, and B. A. Richman, "Measuring Ultrashort Laser Pulses in the Time-Frequency Domain Using Frequency-Resolved Optical Gating," Review of Scientific Instruments **68**(9), 3277–3295 (1997).

[38] J. K. Rhee, T. S. Sosnowski, A. C. Tien, and T. B. Norris, "Real-Time Dispersion Analyzer of Femtosecond Laser Pulses With Use of a Spectrally and Temporally Resolved Upconversion Technique," Journal of the Optical Society of America B **13**(8), 1780–1785 (1996).

[39] V. Wong and I. A. Walmsley, "Ultrashort-Pulse Characterization from Dynamic Spectrograms by Iterative Phase Retrieval," Journal of the Optical Society of America B **14**(4), 944–948 (1997).

[40] D. J. Kane, "Real-Time Measurement of Ultrashort Laser Pulses Using Principal Component Generalized Projections," IEEE Journal of Selected Topics on Quantum Electronics **4**, 278–284 (1998).

[41] A. Baltŭska, M. S. Pshenichnikov, and D. A. Wiersma, "Amplitude and Phase Characterization of 4.5-fs Pulses by Frequency-Resolved Optical Gating," Optics Letters **23**(18), 1474–1476 (1998).

[42] J. M. Dudley, X. Gu, L. Xu, M. Kimmel, E. Zeek, P. O'Shea, R. Trebino, S. Coen, and R. S. Windeler, "Cross-Correlation Frequency Resolved Optical Gating Analysis of Broadband Continuum Generation in Photonic Crystal Fiber: Simulations and Experiments," Optics Express **10**(21), 1215–1221 (2002).

[43] G. Taft, A. Rundquist, M. M. Murnane, I. P. Christov, H. C. Kapteyn, K. W. DeLong, D. N. Fittinghoff, M. A. Krumbügel, J. N. Sweetser, and R. Trebino, "Measurement of 10-fs Laser Pulses," IEEE Journal of Selected Topics in Quantum Electronics **2**(3), 575–585 (1996).

[44] L. P. Barry, J. M. Dudley, B. C. Thomsen, and J. D. Harvey, "Frequency-Resolved Optical Gating Measurement of 1.4 THz Beat Frequencies from Dual Wavelength Self-Seeded Gain-Switched Laser Diode," Electronics Letters **34**(10), 988–990 (1998).

[45] L. P. Barry, B. C. Thomsen, J. M. Dudley, and J. D. Harvey, "Characterization of 1.55-μm Pulses from a Self-Seeded Gain-Switched Fabry-Perot Laser Diode Using Frequency-Resolved Optical Gating," IEEE Photonics Technology Letters **10**(7), 935–937 (1998).

[46] P. G. Bollond, L. P. Barry, J. M. Dudley, R. Leonhardt, and J. D. Harvey, "Characterization of Nonlinear Switchcing in a Figure-of-Eight Fiber Laser Using Frequency-Resolved Optical Gating," IEEE Photonics Technology Letters **10**(3), 343–345 (1998).

[47] J. M. Dudley, L. P. Barry, J. D. Harvey, M. D. Thomson, B. C. Thomsen, P. G. Bollond, and R. Leonhardt, "Complete Characterization of Ultrashort Pulse Sources at 1550 nm," IEEE Journal of Quantum Electronics **35**(4), 441–450 (1999).

[48] L. P. Barry, S. D. Burgo, B. C. Thomsen, R. T. Watts, D. A. Reid, and J. D. Harvey, "Optimization of Optical Data Transmitters for 40-Gb/s Lightwave Systems Using Frequency Resolved Optical Gating," IEEE Photonics Technology Letters **14**(7), 971–973 (2002).

[49] B. C. Thomsen, D. A. Reid, R. T. Watts, L. P. Barry, and J. D. Harvey, "Characterization of 40-Gbit/s Pulses Generated Using a Lithium Niobate Modulator at 1550 nm Using Frequency Resolved Optical Gating," IEEE Transactions on Instrumentation and Measurement **53**(1), 186–188 (2004).

[50] L. P. Barry, J. M. Dudley, P. G. Bollond, J. D. Harvey, and R. Leonhardt, "Complete Characterisation of Pulse Propagation in Optical Fibres Using Frequency-Resolved Optical Gating," Electronics Letters **32**(25), 2339–2340 (1996).

[51] J. M. Dudley, L. P. Barry, P. G. Bollond, J. D. Harvey, R. Leonhardt, and P. D. Drummond, "Direct Measurement of Pulse Distortion Near the Zero-Dispersion Wavelength in an Optical Fiber by Frequency-Resolved Optical Gating," Optics Letters **22**(7), 457–459 (1997).

[52] L. P. Barry, J. M. Dudley, P. G. Bollond, J. D. Harvey, and R. Leonhardt, "Simultaneous Measurement of Optical Fibre Nonlinearity and Dispersion Using Frequency Resolved Optical Gating," Electronics Letters **33**(8), 707–708 (1997).

[53] J. Paye, M. Ramaswamy, J. G. Fujimoto, and E. P. Ippen, "Measurement of the Amplitude and Phase of Ultrashort Light Pulses from Spectrally Resolved Autocorrelation," Optics Letters **18**(22), 1946–1948 (1993).

[54] K. W. DeLong, R. Trebino, J. Hunter, and W. E. White, "Frequency-Resolved Optical Gating with the Use of Second-Harmonic Generation," Journal of the Optical Society of America B **11**(11), 2206–2215 (1994).

[55] J. N. Sweetser, D. N. Fittinghoff, and R. Trebino, "Transient-Grating Frequency-Resolved Optical Gating," Optics Letters **22**(8), 519–521 (1997).

[56] T. Tsang, M. A. Krumbügel, K. W. DeLong, D. N. Fittinghoff, and R. Trebino, "Frequency-Resolved Optical-Gating Measurements of Ultrashort Pulses Using Surface Third-Harmonic Generation," Optics Letters **21**(17), 1381–1383 (1996).

[57] M. D. Thomson, J. M. Dudley, L. P. Barry, and J. D. Harvey, "Complete Pulse Characterisation Using Cross-Phase Modulation in Optical Fibers," Optics Letters **23**(20), 1582–1584 (1998).

[58] P. A. Lacourt, J. M. Dudley, J. M. Merolla, H. Porte, J. P. Goedgebuer, and W. T. Rhodes, "Milliwatt-Peak-Power Pulse Characterization at 1.55 μm by Wavelength-Conversion Frequency-Resolved Optical Gating," Optics Letters **27**(10), 863–865 (2002).

[59] P. A. Lacourt, M. Hanna, and J. Dudley, "Broad-Band and Ultrasensitive Pulse Characterization Using Frequency-Resolved Optical Gating Via Four-Wave Mixing in a Semiconductor Optical Amplifier," IEEE Photonics Technology Letters **17**(1), 157–159 (2005).

[60] C. Dorrer and I. Kang, "Simultaneous Temporal Characterization of Telecommunication Optical Pulses and Modulators by Use of Spectrograms," Optics Letters **27**(15), 1315–1317 (2002).

[61] K. R. Parameswaran, R. K. Route, J. R. Kurz, R. V. Roussev, M. M. Fejer, and M. Fujimura, "Highly Efficient Second-Harmonic Generation in Buried Waveguides Formed by Annealed and Reverse Proton Exchange in Periodically Poled Lithium Niobate," Optics Letters **27**(3), 179–181 (2002).

[62] M. H. Chou, "Optical Frequency Mixers Using Three-Wave Mixing for Optical Fiber Communications," Ph.D. thesis, Department of Applied Physics, Stanford University (1999).

[63] K. R. Parameswaran, "Highly Efficient Optical Frequency Mixers," Ph.D. thesis, Department of Electrical Engineering, Stanford University (2002).

[64] S. D. Yang, A. M. Weiner, K. R. Parameswaran, and M. M. Fejer, "400-Photon-per-Pulse Ultrashort Pulse Autocorrelation Measurement with Aperiodically Poled Lithium Niobate Waveguides at 1.55 μm," Optics Letters **29**(17), 2070–2072 (2004).

[65] J. Prawiharjo, K. Gallo, B. C. Thomsen, M. A. F. Roelens, P. J. Almeida, N. G. R. Broderick, and D. J. Richardson, "Frequency Resolved Optical Gating in a Quasi-Phase-Matched $LiNbO_3$," IEEE Photonics Technology Letters **17**(4), 849–851 (2005).

[66] G. Imeshev, M. A. Arbore, M. M. Fejer, A. Galvanauskas, M. Fermann, and D. Harter, "Ultrashort-Pulse Second Harmonic Generation with Longitudinally Nonuniform Quasi-Phase-Matching Gratings: Pulse Compression and Shaping," Journal of the Optical Society of America B **17**(2), 304–318 (2000).

[67] S. D. Yang, A. M. Weiner, K. R. Parameswaran, and M. M. Fejer, "Ultra-Sensitive Second-Harmonic Generation Frequency-Resolved Optical Gating by Aperiodically Poled $LiNbO_3$ Waveguides at 1.5 μm," Optics Letters **30**(16), 2164–2166 (2005).

[68] J. Prawiharjo, K. Gallo, N. G. R. Broderick, and D. J. Richardson, "Frequency-Resolved Optical Gating in the 1.55 μm-Band Via Cascaded $\chi^{(2)}$ Processes," Journal of the Optical Society of America B **22**(9), 1985–1993 (2005).

[69] J. Prawiharjo, F. Parmigiani, K. Gallo, P. Petropoulos, N. G. R. Broderick, and D. J. Richardson, "Cascaded $\chi^{(2)}$ Interaction Frequency-Resolved Optical Gating in a Periodically-Poled Lithium Niobate Waveguide," (2005). To appear in Optics Letters.

Chapter 2

Frequency-Resolved Optical Gating

The time scale of ultrashort optical pulses is much shorter than the resolution of available standard electronic instruments, making it difficult to measure their temporal intensity profile. In addition, their instantaneous frequency is often more important than the temporal intensity profile, but it is more difficult to obtain. These essentially have been the problems in the characterisation of ultrashort optical pulses for decades. In principle, frequency-resolved optical gating (FROG)[1–4] solves this problem by making measurements in the time-frequency domain. Its accuracy and reliability have made it a well-established and widely-employed technique for the complete (intensity and phase) characterisation of ultrashort optical pulses.

In this chapter, a review of the fundamentals of the FROG technique will be given, with particular attention to the configurations based on $\chi^{(2)}$ interactions. The review starts with the problems concerning the characterisation of ultrashort optical pulses in section 2.1. These problems were solved with the introduction of FROG, whose general concepts are given in section 2.2. In section 2.3, SHG FROG,[5,6] the most widely used FROG configuration, is presented. Next, Cross-correlation FROG (XFROG) and blind-FROG, variations of the FROG configuration based on $\chi^{(2)}$ interactions, are described in section 2.4. Finally, an algorithm to retrieve the complex amplitudes of ultrashort optical pulses from FROG measurements is given in section 2.5.

2.1 Characterisation of Ultrashort Optical Pulses

An ultrashort pulse is described by its electric field, which can be a complicated vectorial function of space and time (see Section 5.1). In this chapter, we are only interested in the temporal features of the pulse, and thus we can write the temporal dependence of

the electric field as follows:

$$E(t) = A(t) \exp\left(-i\omega_0 t\right) + \text{c.c.}, \tag{2.1}$$

where $A(t)$ is the slowly varying complex amplitude, and ω_0 is the carrier frequency of the pulse. The complex amplitude $A(t)$ can be written as:

$$A(t) = \Psi(t) \exp\left[i\phi(t)\right], \tag{2.2}$$

where $\Psi(t) \in \mathbb{R}$, $\Psi(t) > 0$ is the temporal profile, and $\phi(t) \in \mathbb{R}$ is the phase. The spectral envelope counterpart of the above slowly-varying amplitude in the time-domain, which comprises the spectral profile $\psi(\Omega)$ and spectral phase $\varphi(\Omega)$, is given by the Fourier transform of Eq. (2.2) as follows:

$$\mathcal{F}[A(t)] = \hat{A}(\Omega) = \psi(\Omega) \exp\left[i\varphi(\Omega)\right], \tag{2.3}$$

with $\Omega = \omega - \omega_0$ being the frequency detuning coordinate from the central frequency ω_0 of an ultrashort optical pulse. The instantaneous frequency of the pulse, which describes the frequency distribution across the pulse, is given by:

$$\omega(t) = \omega_0 + \Omega_c(t) = \omega_0 - \frac{\partial\phi(t)}{\partial t}, \tag{2.4}$$

and the quantity

$$f(t) = \frac{1}{2\pi}\Omega_c(t) = -\frac{1}{2\pi}\frac{\partial\phi(t)}{\partial t} \tag{2.5}$$

is known as the chirp. An ultrashort optical pulse is said to be completely characterised if one knows its profile [$\Psi(t)$ or $\psi(\Omega)$] and phase [$\phi(t)$ or $\varphi(\Omega)$] in either domains, as they are related by a Fourier transform. In general, the knowledge of profiles in both temporal [$\Psi(t)$] and spectral domains [$\psi(\Omega)$] is sufficient to uniquely determine the phases in either domains using Gerchberg-Saxton algorithm,[7] apart from occasional ambiguities as discussed more fully in Ref. 4.

Let us examine the detection of these four quantities one-by-one. In principle, in the time domain, the power distribution of an optical pulse [$\mathcal{P}(t) = |A(t)|^2 = \Psi^2(t)$] could be measured by a photodetector (provided its response would be faster than the time-scale of the optical pulse). Its phase [$\phi(t)$], however, is difficult to measure, since photodetectors at optical frequencies, known as the square-law detectors, are responsive only to the photon flux. Nevertheless, it is possible to measure the complex amplitude $A(t)$ of an optical pulse by interfering it with a local oscillator, that is, another coherent

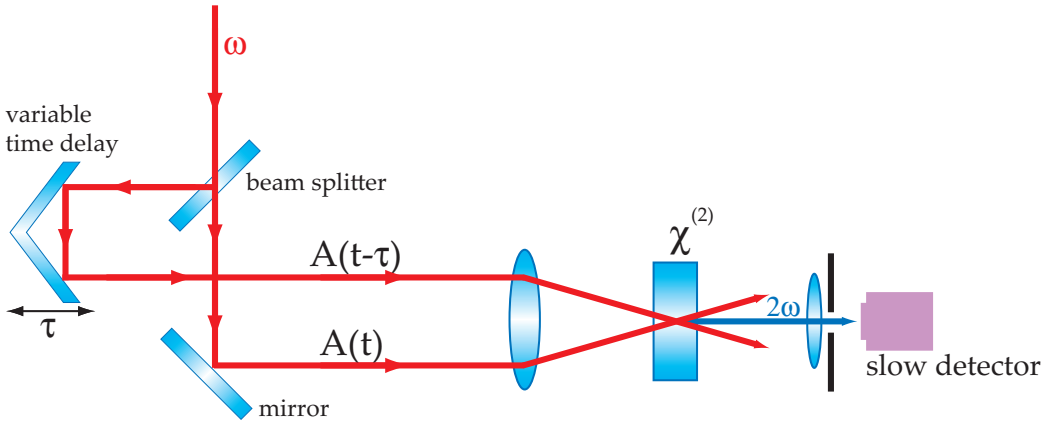

Figure 2.1: Schematic illustration of an intensity autocorrelator.

reference pulse of known stable phase, and detecting it using a photodetector. This technique is known as heterodyne detection.[8] However, as the time scale of ultrashort optical pulses is much shorter than the response of currently available photodetectors, the measurement of its power distribution and phase become almost impossible. In frequency domain, the spectral profile $\psi(\Omega)$ of ultrashort optical pulses can be trivially measured by a spectrometer due to its broad nature. Again, square-law detectors prevent one from measuring the spectral phase $\varphi(\Omega)$. In addition, one cannot determine the phase $[\phi(t)$ or $\varphi(\Omega)]$ from the sole knowledge of its profile $[\Psi(t)$ or $\psi(\Omega)]$, i.e. the so-called *one-dimensional phase-retrieval problem*.[9,10] In short, of these four quantities, only the knowledge of the spectral profile $\psi(\Omega)$ can be easily obtained, which is not sufficient to completely characterise an optical pulse.

The lack of shorter events gave rise to the notion of using the ultrashort pulse to measure itself. Intensity autocorrelation[11] is an attempt to measure the temporal profile of ultrashort pulses. It became the standard measurement technique for decades, mainly due to the lack of better techniques. Figure 2.1 shows an illustration of this technique. It involves creating a replica of the pulse, introducing a variable time-delay τ to one of the pulses, and finally spatially mixing them in an instantaneous nonlinear material, such as a $\chi^{(2)}$ material. In a sufficiently short $\chi^{(2)}$ material such that the temporal walk-off is negligible, and using a sufficiently low input power such that the pump depletion is negligible, the output SH pulse envelope A_{sig} is given by:

$$A_{\text{sig}}(t,\tau) \propto A(t)A(t-\tau). \tag{2.6}$$

Since the detectors are slow compared to the time-scale of the pulse, an autocorrelator

yields the so-called autocorrelation trace:

$$\begin{aligned}\mathcal{P}_{\mathrm{AC}}(\tau) &= \int_{-\infty}^{\infty} |A(t)A(t-\tau)|^2 \, dt \\ &= \int_{-\infty}^{\infty} \mathcal{P}(t)\mathcal{P}(t-\tau)dt,\end{aligned} \tag{2.7}$$

This SHG based autocorrelation is often called the second-order intensity autocorrelation. Unfortunately, there is no way to obtain precise information about $\Psi(t)$ from the above expression, even with additional information concerning the temporal profile, such as $\Psi(t) > 0$ and $\Psi(t) \to 0$, as $t \to \infty$, and spectral measurements.[12]

The inadequacies of second-order autocorrelation prompted a search for other more advanced techniques to completely characterise optical pulses, such as third-order autocorrelation[13] and fringe-resolved autocorrelation (FRAC).[14] A third-order autocorrelation is similar to the second-order one, but it involves mixing the test pulse and its replica in $\chi^{(3)}$ materials. Fringe-resolved autocorrelation involves performing a second-order autocorrelation with a collinear geometry, such that the trace is given by:

$$\mathcal{P}_{\mathrm{FRAC}}(\tau) = \int_{-\infty}^{\infty} \left|[A(t) + A(t-\tau)]^2\right|^2 \, dt, \tag{2.8}$$

which can be expanded into:

$$\begin{aligned}\mathcal{P}_{\mathrm{FRAC}}(\tau) = 2\int_{-\infty}^{\infty} \mathcal{P}(t)\mathcal{P}(t-\tau)dt + \int_{-\infty}^{\infty} \mathcal{P}^2(t)dt + \int_{-\infty}^{\infty} \mathcal{P}^2(t-\tau)dt \\ + 4\int_{-\infty}^{\infty} [\mathcal{P}(t) + \mathcal{P}(t-\tau)] \, \mathrm{Re}\left[A(t)A^*(t-\tau)\right] dt \\ + 2\int_{-\infty}^{\infty} \mathrm{Re}\left\{A^2(t)[A^*(t-\tau)]^2\right\} dt.\end{aligned} \tag{2.9}$$

One can readily identify the first term as the standard autocorrelation trace, whilst the second and the third terms are constant and delay-dependent backgrounds, respectively. The last two terms, on the other hand, can be identified as rapidly varying interferometric terms, which create difficulties in the interpretation of the measurement results. Since none of these techniques managed to obtain the phase information of the pulses, they cannot completely solve the ultrashort pulse characterisations problem.

2.2 Time-Frequency Distribution and FROG

Whilst the broad extent of an ultrashort pulse spectrum makes it easy to be measured, we have seen that the measurement of its temporal profile is difficult. Autocorrelation

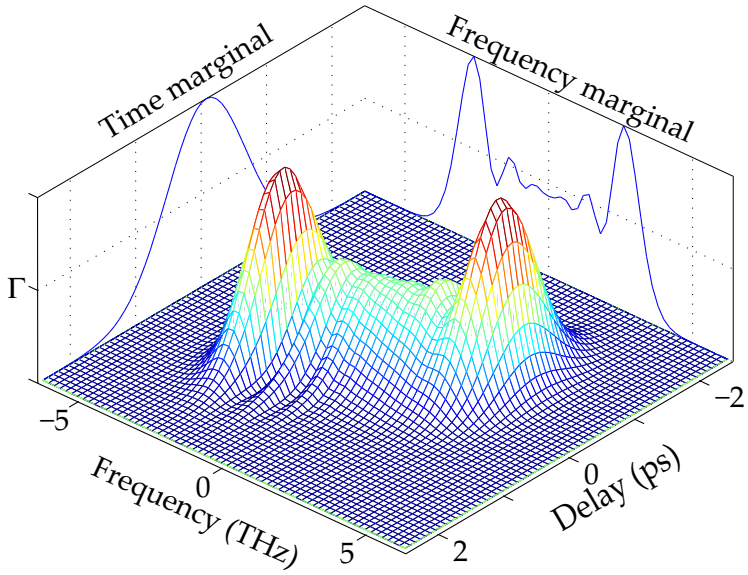

Figure 2.2: Example of a spectrogram [Eq. (2.12)] with its time and frequency marginals [Eq. (2.15)].

and other measurement techniques worked purely in the time-domain in an attempt to extract the temporal profile of an ultrashort pulse. Since the temporal and spectral domains are not independent, the broad spectrum of an ultrashort pulse can be utilised for its characterisation. Hence, instead of purely working in one domain, the time-frequency distribution of such pulses should be considered. The concept of time-frequency distribution is simple and powerful. The spectrum of an ultrashort pulse only identifies its spectral density, but not its instantaneous frequency $[\omega(t)]$. In order to ascertain the instantaneous frequency, one can break the pulse into segments and Fourier transform them.

In order to study the property of an ultrashort pulse $A(t)$ around time τ, one can window it with a complex gate function

$$G(t) = g(t) \exp\left[i\varsigma(t)\right], \tag{2.10}$$

which is similarly defined as Eq. (2.2), and $|G(t)| \to 0$ as $t \to \infty$, to produce the following signal field:

$$A_{\text{sig}}(t, \tau) = A(t)G(t - \tau). \tag{2.11}$$

Fourier transform of the signal field yields the distribution of frequency around time τ, i.e. the so-called spectrogram:[15]

$$\Gamma(\Omega, \tau) = \left|\mathcal{F}\left[A_{\text{sig}}(t, \tau)\right]\right|^2 = \left|\hat{A}_{\text{sig}}(\Omega, \tau)\right|^2. \tag{2.12}$$

Figure 2.2 shows a typical example of a spectrogram constructed from a self-phase-modulated (SPM) Gaussian test pulse and a transform-limited (TL) Gaussian gate pulse. One can intuitively observe the phase modulation in the spectrogram.

Spectrogram measurements of ultrashort optical pulses essentially make up half of the frequency-resolved optical gating (FROG) technique. Obviously, the final goal of the FROG technique is to retrieve the complex amplitude $A(t)$ from the measured spectrogram. If the phase information of the signal field Fourier transform $\hat{A}_{\text{sig}}(\Omega,\tau)$ is available, the complex amplitude $A(t)$ can be easily obtained by choosing $\tau = t$, such that:

$$\mathcal{F}^{-1}\left[\hat{A}_{\text{sig}}(\Omega,\tau=t)\right] = A_{\text{sig}}(t,\tau=t) = A(t)G(0). \tag{2.13}$$

In other words, the complex amplitude $A(t)$ has been completely determined up to a constant multiplicative factor $G(0)$ from the knowledge of $\hat{A}_{\text{sig}}(\Omega,\tau)$. However, the measured spectrogram $\Gamma(\Omega,\tau)$ only yields the magnitude of $\hat{A}_{\text{sig}}(\Omega,\tau)$, its phase is yet to be found. Hence, the problem is to find $\arg\left[\hat{A}_{\text{sig}}(\Omega,\tau)\right]$ from $\left|\hat{A}_{\text{sig}}(\Omega,\tau)\right|$, i.e. the so-called *two-dimensional phase retrieval problem*.[16–19] In contrast to the one-dimensional phase retrieval problem which has infinitely many solutions, the two-dimensional one essentially has a unique solution, apart from trivial ambiguities.[16] These trivial ambiguities mean that the FROG technique is not to be able to distinguish between $A(t)$ and:

$$A(t)\mathrm{e}^{(ic_0)} \qquad \text{(constant phase factor)}, \tag{2.14a}$$

$$A(t)\mathrm{e}^{(ic_1 t)} \qquad \text{(linear phase shift)}, \tag{2.14b}$$

$$A(t-t_0) \qquad \text{(absolute time reference)}, \tag{2.14c}$$

where $c_0, c_1 \in \mathbb{R}$ are arbitrary constants. The two-dimensional phase retrieval is usually done by an iterative algorithm,[20] whose implementation for retrieving ultrashort pulse complex amplitudes is given in section 2.5.

It is easy to reduce the time-frequency distribution to a distribution in either domain, by performing an integration with respect to the other domain:

$$\mathcal{M}_{\Omega}^{\Gamma}(\tau) = \int_{-\infty}^{\infty} \Gamma(\Omega,\tau)d\Omega, \qquad \text{and} \qquad \mathcal{M}_{\tau}^{\Gamma}(\Omega) = \int_{-\infty}^{\infty} \Gamma(\Omega,\tau)d\tau. \tag{2.15}$$

These quantities are called the time and frequency *marginals*,[15,21] respectively. For a spectrogram, the time marginal yields the cross-correlation between the test pulse and the gate function magnitudes:

$$\mathcal{M}_{\Omega}^{\Gamma}(\tau) = \int_{-\infty}^{\infty} \Psi^2(t)g^2(t-\tau)dt, \tag{2.16}$$

whilst the frequency marginal yields the convolution between the test pulse and the gate function spectra:

$$\mathcal{M}_{\tau}^{\Gamma}(\Omega) = \int_{-\infty}^{\infty} \psi^2(\Omega') \left|\hat{G}(\Omega - \Omega')\right|^2 d\Omega'. \tag{2.17}$$

Figure 2.2 also shows the temporal and and frequency marginals of a spectrogram. These marginals will later prove to be powerful tools for self-consistency error checks in the FROG technique.

Apart from the spectrogram, there are other classes of time-frequency distribution:[15] Wigner, Choi-Williams, Rihaczek, and Born-Jordan distributions, to name a few. Some of these distributions are considered to be better and more elegant than the spectrogram. The Wigner distribution is of particular importance and is worth mentioning briefly here. Given a complex amplitude $A(t)$ of an ultrashort pulse, its Wigner distribution is given by:

$$W(\Omega, \tau) = \int_{-\infty}^{\infty} A^*\left(\tau + \frac{t}{2}\right) A\left(\tau - \frac{t}{2}\right) \exp(-i\Omega t) dt. \tag{2.18}$$

The Wigner distribution is always real, but, unlike a spectrogram, it can have negative values. Compared to the spectrogram, a Wigner distribution gives a clearer picture of an ultrashort pulse. Its time marginal yields the power, $M_{\Omega}^{W}(\tau) = \Psi^2(t) = \mathcal{P}(t)$, whilst its frequency marginal yields its spectrum, $M_{\tau}^{W}(\Omega) = \psi^2(\Omega)$. A Wigner distribution can also be easily inverted to obtain the complex amplitude $A(t)$:[15]

$$A(\tau = t) \propto \int_{-\infty}^{\infty} W\left(\Omega, \frac{\tau}{2}\right) \exp(i\Omega\tau) d\Omega. \tag{2.19}$$

However, the elegance of a Wigner distribution is not accompanied with practicality, as it involves the creation of time-reversed replica of the test pulse and the measurement of negative values. What FROG lacks in mathematical elegance, it makes up for in practical experimental elegance.

2.3 SHG FROG

Experimentally, a spectrogram is a spectrally-resolved autocorrelation measurement [Eq. (2.12)], as the gate function is usually chosen to be the test pulse itself. A spectrogram can therefore be easily produced by spectrally-resolving the signal field of any autocorrelation type measurements. As different autocorrelation type measurements rely on different nonlinear interactions to achieve the mixing between the test pulse and its replica, the general form of their signal field [Eq. (2.11)], and thus their spectrogram

Table 2.1: Several FROG configurations, the nonlinear interactions they used, the mathematical form of their generated signal fields, and the frequency of the signal fields.

FROG configuration	Nonlinearity	Signal Field	Signal Frequency
Polarisation gate (PG)[1]	$\chi^{(3)}$	$A(t)\,\lvert A(t-\tau)\rvert^2$	ω
Self diffraction (SD)[2]	$\chi^{(3)}$	$A^2(t)A(t-\tau)$	ω
Transient grating (TG)[22]	$\chi^{(3)}$	$A^2(t)A^*(t-\tau)$	ω
Second-harmonic generation (SHG)[5,6]	$\chi^{(2)}$	$A(t)A(t-\tau)$	2ω
Third-harmonic generation (THG)[23]	$\chi^{(3)}$	$A(t)A^2(t-\tau)$	3ω

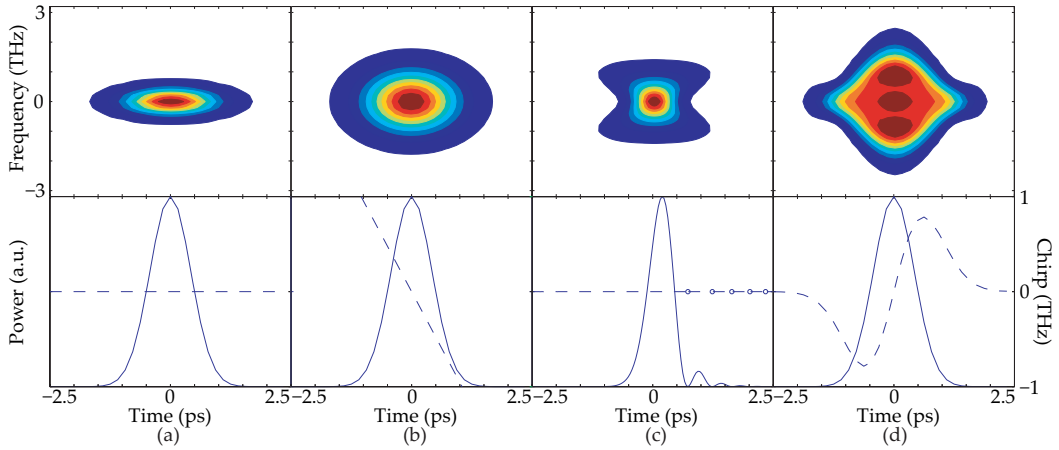

Figure 2.3: SHG FROG spectrograms [Eq. (2.20)] for several common pulses: a) a TL Gaussian, b) a linearly-chirped Gaussian, b) a Gaussian with a cubic spectral phase, and d) a self-phase-modulated Gaussian. Note that open circles in b) correspond to nondifferentiable π phase jumps.

[Eq. (2.12)], also varies. Table 2.1 shows several common FROG configurations and the mathematical form of their generated signal fields.

Since most of the common FROG configurations rely on, generally weak, $\chi^{(3)}$ interactions, SHG FROG, which relies on a $\chi^{(2)}$ interaction, offers the best sensitivity. Moreover, SHG FROG (and THG FROG) achieves the best signal-to-noise ratio (SNR), as the generated signal field is at a different frequency, making scattered light easier to filter out. In addition, a SHG FROG device can be easily made from a second-order intensity autocorrelation setup, by replacing the detector with a spectrometer (Fig. 2.1). The SHG FROG spectrogram is given by:

$$\Gamma^{(\mathrm{SHG})}(\Omega,\tau) \propto \left| \int_{-\infty}^{\infty} A(t)A(t-\tau)\exp\left(-i\Omega t\right)dt \right|^2 . \tag{2.20}$$

From the above expression, it can be directly seen that the expected frequency marginal

is equivalent to the autoconvolution of the test pulse spectrum. Figure 2.3 shows SHG FROG spectrograms for several common pulses: a TL Gaussian, a linearly-chirped Gaussian, a Gaussian with a cubic spectral phase, and a SPM Gaussian.

It can be easily shown, that the time-reversal and complex-conjugate of the complex amplitude $A(t)$, i.e. $A^*(-t)$, also yields the same spectrogram. A simple way to get around this ambiguity is to perform another characterisation after introducing some known distortion to the test pulse, such as a leading satellite pulse from a surface reflection.[24]

The accuracy and validity of Eq. (2.20) is an important consideration for the experiments. Equation (2.20) was written with the assumptions that the input pulse powers are sufficiently low, i.e. no-pump-depletion limit, to guarantee its linearity, and that the $\chi^{(2)}$ material is sufficiently short to avoid the temporal walk-off effect. In order to maintain the linear relationship in Eq. (2.20) to within 1%, the peak (energy) conversion efficiency must be kept below 3% (2.1%).[6] This, however, is not a very restrictive constraint. A more restrictive constraint comes from the interaction length of the $\chi^{(2)}$ material, which causes the spectrogram to be corrupted by the SHG transfer function [discussed in detail in Chapter 5] due to the temporal walk-off effect. Fortunately, the distortion in the spectrogram arising from the temporal walk-off effect can be corrected by forcing the agreement between the measured and the expected frequency marginals [Eq. (2.17)], that is, by multiplying the spectrogram by the ratio between the expected and measured frequency marginals.[21] This procedure does not only correct the distortion due to the acceptance bandwidth insufficiency, but also corrects for other unknown effects. Obviously, since this procedure involves multiplication, it only works if there are no zeros in the frequency-dependent transfer functions. Since there are zeros in the SHG transfer function, as explained in Section 5.2, this method cannot be used to completely lift the interaction length restriction. Correction of the frequency marginals has been used to aid the characterisations of several femtoseconds long pulses.[25,26] Another way to circumvent this acceptance bandwidth restriction is to angle-dither the $\chi^{(2)}$ material.[27]

The noncollinear geometry in SHG FROG limits its application in a number of cases where a collinear geometry is imposed, such as in the focus planes of microscope objectives[28–30] or in guided-wave geometries. Similar to the FRAC [Eq. (2.9)], a collinear SHG FROG configuration yields an interferometric term.[31,32] As this interferometric

term is highly sensitive to phase changes, it is experimentally more complex than standard SHG FROG. The simplest approach to avoid these terms is to use a type-II SHG interaction,[28–30] in which there is a $\frac{\pi}{2}$-difference between the polarisations of the test pulse and its replica. This configuration is not interferometric, and its spectrogram is exactly the same as that of standard SHG FROG [Eq. (2.20)].

2.4 XFROG and Blind-FROG

Although the standard SHG FROG configuration works extremely well for a wide range of test pulses and proves to be more sensitive than other common FROG configurations, it is still limited in some ways. Since SHG FROG still relies on a nonlinear interaction, its sensitivity is still limited to pulse energies of the order of picojoules. Furthermore, its implementation in the near UV or the mid-IR is restricted, due to the unavailability of sensitive detectors at the SH wavelength and/or the limited transparency range of the nonlinear material used in the configuration. In addition, type-II SHG FROG configurations cannot be implemented in a number of cases, such as in waveguides that support only one polarisation. Finally, the characterisation of relatively long pulses, which have a very narrow spectral bandwidth, is restricted by the resolution of a spectrometer.

These limitations can be overcome by gating the unknown test pulse with an intense well-characterised reference pulse, i.e. the so-called cross-correlation FROG (XFROG) technique.[33,34] Using this technique, characterisations of weak ultrashort pulses have been demonstrated using both sum-frequency[33,35] and difference-frequency[34,36] generation (SFG and DFG). For example, it was used to characterise ultrashort pulses in the mid-IR by sum-frequency mixing with near-IR pulses.[35] Characterisations of relatively long pulses is also possible, by mixing them with shorter ones, and thus mapping their spectra onto the broader one of the reference pulse.

The generated XFROG spectrogram is given by:

$$\Gamma^{(\mathrm{XFROG})}(\Omega,\tau) \propto \begin{cases} \left|\int_{-\infty}^{\infty} A(t)G(t-\tau)\exp\left(-i\Omega t\right)dt\right|^2 & \text{(for SFG)} \\ \left|\int_{-\infty}^{\infty} A^*(t)G(t-\tau)\exp\left(-i\Omega t\right)dt\right|^2 & \text{(for DFG with } \omega_{\mathrm{T}} < \omega_{\mathrm{R}}\text{)} \\ \left|\int_{-\infty}^{\infty} A(t)G^*(t-\tau)\exp\left(-i\Omega t\right)dt\right|^2 & \text{(for DFG with } \omega_{\mathrm{T}} > \omega_{\mathrm{R}}\text{).} \end{cases} \tag{2.21}$$

In the above expressions, $A(t)$ is the complex amplitude of the test pulse at a central frequency ω_{T}, and $G(t)$ is the complex amplitude of the reference pulse at a central

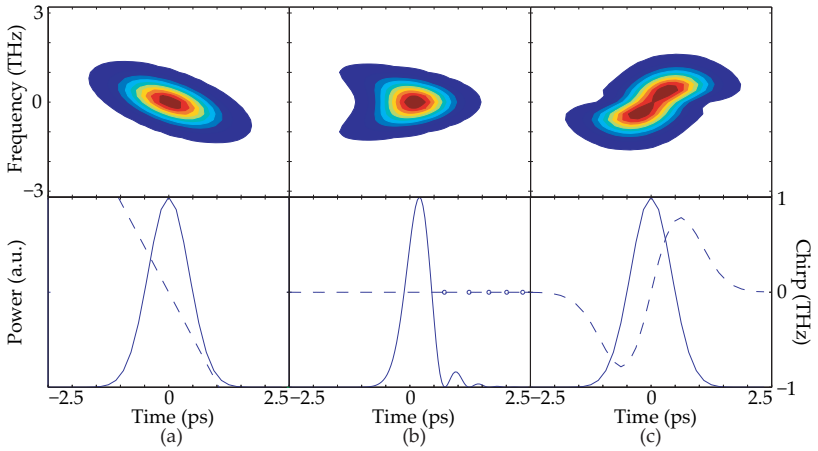

Figure 2.4: SFG XFROG/blind-FROG spectrograms [Eq. (2.21)] for a TL Gaussian pulse mixed with several other common pulses: a) a linearly-chirped Gaussian, b) a Gaussian with a cubic spectral phase, and c) a self-phase-modulated Gaussian. Note that open circles in b) correspond to nondifferentiable π phase jumps.

frequency ω_{R}. The complex amplitude of the test pulse $A(t)$ can be retrieved from the measured spectrogram by incorporating the well-characterised reference pulse into the numerical (iterative) algorithm. Figure 2.4 shows SFG XFROG spectrograms generated from a TL Gaussian pulse mixed with several other common pulses: a linearly chirped Gaussian pulse, a Gaussian with a cubic spectral phase, and a self-phase-modulated Gaussian pulse. It can be easily observed, that XFROG yields asymmetric spectrograms, which are more intuitive than SHG FROG ones (Fig. 2.3).

Similar to SHG FROG, the experimental considerations for XFROG configurations also concern the accuracy of Eq. (2.21). The power level of the reference pulse must be sufficiently low such that the linear relationships in Eq. (2.21) are maintained. Temporal walk-off effects arising in sufficiently long crystals have different implications on the SFG and DFG XFROG configurations, as discussed in Chapter 5. The effect of temporal walk-off on SFG XFROG is similar to that on SHG FROG, i.e. a distorted spectrogram due to the insufficiency of acceptance bandwidth. This distortion can be corrected by forcing the agreement between the measured and the expected frequency marginals, provided that there are no zeros in the transfer functions, as previously described. For DFG XFROG, the temporal walk-off effect yields a filter function for the pulse at a higher frequency [Eq. (5.25)], causing incorrect pulse retrieval. The distortion in the spectrogram cannot be rectified by simply forcing the agreement between the measured and the expected frequency marginals. Hence, the use of a sufficiently short (less than one walk-off length) $\chi^{(2)}$ material is imperative in XFROG configurations.

The requirement for $G(t)$ to be a well-characterised pulse is not necessary to retrieve the test pulse complex amplitude $A(t)$ from the XFROG spectrograms [Eq. (2.21)]. Without *a priori* knowledge of both $A(t)$ and $G(t)$, their retrieval is still possible with the use of a blind-deconvolution type algorithm,[37,38] which will be described in detail in the next section. This technique, called blind-FROG, is a more general form of the XFROG and SHG FROG configurations. The experimental considerations for blind-FROG are the same as those for XFROG, with the exception of crystal length restriction for DFG blind-FROG. The use of long $\chi^{(2)}$ material allows only the pulse at a lower frequency to be correctly retrieved due to the filtering from the temporal walk-off effect [Eq. (5.25)], whilst the pulse at a higher frequency cannot be correctly retrieved. In general, unless the temporal walk-off effect is negligible, the gate pulse is not equal to the input reference pulse, as the latter is modified during its propagation, as described in Section 5.4.

The generality of blind-FROG is actually accompanied by more ambiguities.[39] In addition to the trivial ambiguities of the FROG technique, the exchange of the $A(t)$ and $G(t)$ pair with $G^*(-t)$ and $A^*(-t)$ pair yields the same spectrogram. For the special case of a symmetric spectrogram, i.e. $\Gamma^{(\mathrm{XFROG})}(\Omega,\tau) = \Gamma^{(\mathrm{XFROG})}(\Omega,-\tau)$, the exchange between $A(t)$ and $G(t)$, or the pulses with their time-reverse complex-conjugate, also yields the same spectrogram. In addition to these trivial ambiguities, there exist nontrivial ambiguities, i.e. there exist other pulse pairs which yield **exactly** identical spectrograms to the original pair $A(t)$ and $G(t)$. Siefert, *et al.*[39] showed the existence of a pair of linearly chirped Gaussian pulses which generate an identical spectrogram with a different pair of linearly chirped Gaussian pulses. The spectra of those pairs are identical. They also show the existence of approximate nontrivial ambiguities, i.e. there exist other pulse pairs which yield **nearly** identical spectrograms to the original pair $A(t)$ and $G(t)$. Therefore, additional constraints in the retrieval algorithm, such as spectra of both pulses, are usually necessary. Siefert, *et al.* also found that asymmetric spectrograms are more likely to yield unique solutions without additional constraints.

2.5 Retrieval Algorithm

The measurement of a spectrogram only makes up half of the FROG technique, whilst the retrieval of the complex amplitudes $A(t)$ and $G(t)$ from the spectrogram makes up the other half. Since there is no known analytical expression to directly recover these

amplitudes from a spectrogram, an iterative algorithm is necessary. The simplest retrieval algorithm is based on the iterative Fourier transforms.[1] As this algorithm was unstable, some modifications were introduced[40] at the expense of computational time. A more reliable and faster algorithm, whose convergence is guaranteed, is based on the generalised projection method.[41] Yet, this algorithm was still considered slow, largely due to the line minimisation step in the algorithm. Fortunately, there exists a powerful method that eliminates the need for minimisation called the principal component generalised projection (PCGP) algorithm.[42,43] This algorithm converts the minimisation problem into an eigenvector problem, solved via singular value decomposition (SVD), and thus significantly reduces the computational time such that real-time pulse retrieval is made possible. We discuss the PCGP algorithm below in more detail.

Practically, the data acquisition and processing rely on the discretisation of the time t, delay τ, and frequency Ω. Hence, the amplitudes $A(t)$ and $G(t)$ are represented as complex vectors of size N, i.e.

$$|A\rangle = [A_1, A_2, \ldots, A_N], \qquad \text{and} \qquad |G\rangle = [G_1, G_2, \ldots, G_N], \tag{2.22}$$

where the components $A_j, G_j \in \mathbb{C}$, whilst the measured spectrogram $\Gamma(\Omega, \tau)$ is represented numerically as an $N \times N$ real-valued matrix, i.e.

$$\Gamma \equiv \begin{bmatrix} \Gamma_{11} & \Gamma_{12} & \ldots & \Gamma_{1N} \\ \Gamma_{21} & \ddots & & \Gamma_{2N} \\ \vdots & & \ddots & \vdots \\ \Gamma_{N1} & \ldots\ldots\ldots & & \Gamma_{NN} \end{bmatrix}, \tag{2.23}$$

in the so-called Fourier grid, that is, a grid where the product of the frequency span and the temporal spacing equals unity. The objective of the retrieval process is to find $|A\rangle$ and $|G\rangle$ which generate a spectrogram Γ^{c}_{ij} that matches the measured spectrogram Γ^{m}_{ij}. In other words, this is a minimisation problem with respect to the following metric function:

$$Z = \left[\frac{1}{N^2} \sum_{ij}^{N} \left| \Gamma^{(\mathrm{m})}_{ij} - \Gamma^{(\mathrm{c})}_{ij} \right|^2 \right]^{\frac{1}{2}}. \tag{2.24}$$

The constraint in this problem is that the peaks of both the amplitudes $[|A\rangle, |G\rangle]$ and the spectrogram (Γ) are unity. This problem can also be considered as a deconvolution problem.

It is worth noting that there is an inherent redundancy in this problem, which can be described as follows. The spectrogram matrix Γ contains N^2 real variables, and yet

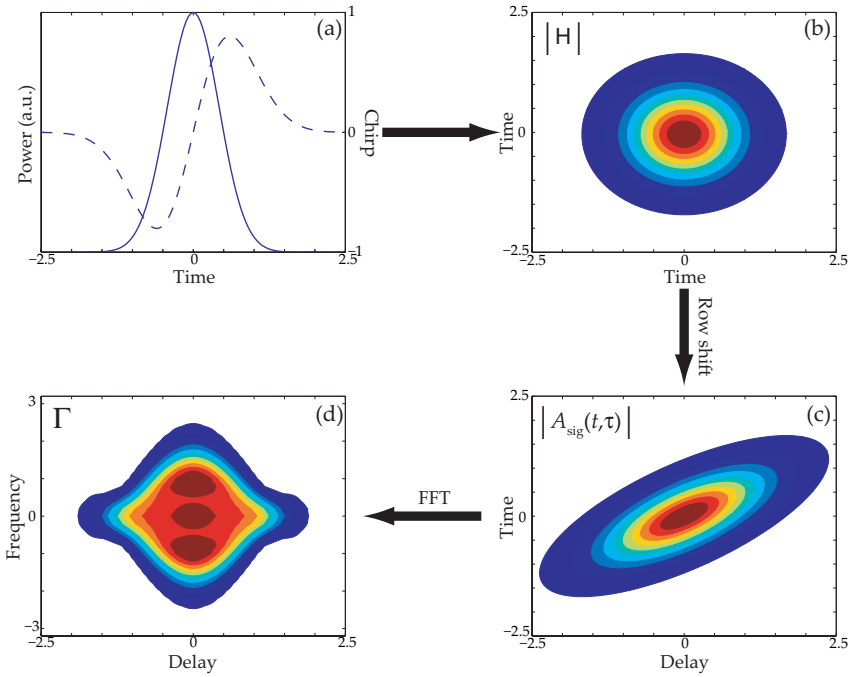

Figure 2.5: Illustration of the construction of a numerical spectrogram.

one wants to determine $2N$ real variables from it, N for each amplitude and phase of vector $|A\rangle$, for a standard FROG problem, where the pulse is gated by itself. This redundancy also makes possible the retrieval of an additional $2N$ real variables for the gate vector $|G\rangle$ in the blind-FROG configuration.

Figure 2.5 illustrates a numerical spectrogram construction from the complex vectors $|A\rangle$ and $|G\rangle$, where $|A\rangle = |G\rangle$ is an SPM Gaussian pulse [Fig. 2.5(a)]. The spectrogram construction starts with the outer product

$$\mathsf{H} = |A\rangle^* \langle G| \,, \tag{2.25}$$

of the amplitudes $|A\rangle$ and $|G\rangle$, where $|A\rangle^*$ is the complex conjugate of $|A\rangle$ [Fig. 2.5(b)]. Next, the signal field matrix $A_{\mathrm{sig}}(t,\tau)$ [Fig. 2.5(c)] can be obtained by shifting row j above the central row of matrix H by the following procedure:

$$[H_{j1}, H_{j2}, \ldots, H_{jN}] \rightarrow [0, \ldots, 0, H_{j1}, H_{j2}, \ldots, H_{j(N-j)}], \tag{2.26}$$

and row j below the central row of matrix H by the following procedure:

$$[H_{j1}, H_{j2}, \ldots, H_{jN}] \rightarrow [H_{j(1+j)}, H_{j(2+j)}, \ldots, H_{jN}, 0, \ldots, 0]. \tag{2.27}$$

Finally, the sought after spectrogram Γ can be obtained by taking the magnitude-squared of the Fourier transform of the signal field matrix rows [Fig. 2.5(d)].

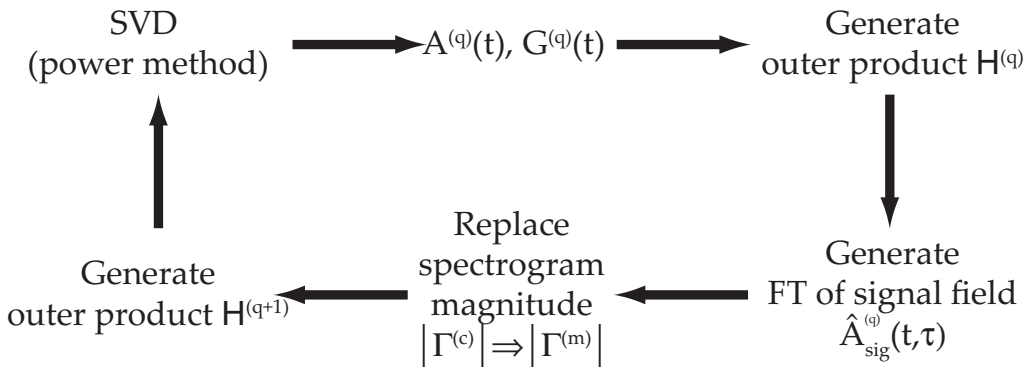

Figure 2.6: Flowchart of the principal component generalised projection algorithm.

Figure 2.6 shows an illustration of the PCGP algorithm. An iteration of the algorithm starts with the amplitudes $|A\rangle^{(q)}, |G\rangle^{(q)}$, followed by the generation of the FT of the signal field from the outer product of these amplitudes. The next step is to replace the intensity of the FT of the signal field by the measured spectrogram:

$$\hat{A}_{\mathrm{sig}}^{(q+1)}(\Omega,\tau) = \sqrt{\Gamma^{(\mathrm{m})}}\arg\left[\hat{A}_{\mathrm{sig}}^{(q)}(\Omega,\tau)\right]. \tag{2.28}$$

Afterwards, the new outer product H must be generated from the FT of the signal field. The application of SVD to the outer product H results in several sets of eigenvalues and eigenvectors. Keeping the pair of eigenvectors with the largest eigenvalue, i.e. the principal component, gives us the next guesses for the amplitudes $|A\rangle^{(q+1)}, |G\rangle^{(q+1)}$. These steps are repeated until a convergence is achieved, which is defined as when there is no significant change to the error [Eq. (2.24)].

Crucial to the PCGP algorithm is the SVD step. Given a complex matrix H, its singular value decomposition (SVD) takes the following form:[44]

$$\mathsf{H} = \mathsf{U}^{\dagger}\mathsf{D}\mathsf{V}, \tag{2.29}$$

where U and V are orthogonal matrices which contain the so-called left and right singular vectors of H, $|u\rangle_j$ and $|v\rangle_j$, respectively, $\mathsf{U}^{\dagger}$ is the Hermitian adjoint of U, and D is a diagonal matrix whose components ζ_j are the singular values of matrix H. For our matrix H, given by Eq. (2.25), this decomposition should yield only one nonzero singular value ζ_p,[42] which corresponds to one left eigenvector $|u\rangle_p = |A\rangle^*$ and one right eigenvector $|v\rangle_p = |G\rangle$.

The direct application of SVD to H to obtain the left and right eigenvectors is computationally expensive . The fact that the matrix H has only one eigenvalue, can

be exploited to obtain the eigenvectors pair. The eigenvalue problem for the left and right eigenvectors can be written as:

$$\mathsf{H}\mathsf{H}^{\dagger}\left|u\right\rangle_{j} = \zeta_{j}\left|u\right\rangle_{j}, \qquad \text{and} \qquad \mathsf{H}^{\dagger}\mathsf{H}\left|v\right\rangle_{j} = \zeta_{j}\left|v\right\rangle_{j}. \tag{2.30}$$

Suppose one takes an arbitrary vector constructed from the orthogonal basis:

$$\left|w\right\rangle = \sum_{j}^{N} c_{j}\left|u\right\rangle_{j}, \tag{2.31}$$

where c_j is an arbitrary constant. Multiplication by $\mathsf{H}\mathsf{H}^{\dagger}$ yields

$$\mathsf{H}\mathsf{H}^{\dagger}\left|w\right\rangle = \sum_{j}^{N} c_{j}\zeta_{j}\left|u\right\rangle_{j}. \tag{2.32}$$

Performing this operation several times directly yields

$$\left(\mathsf{H}\mathsf{H}^{\dagger}\right)^{n}\left|w\right\rangle = \sum_{j}^{N} c_{j}\zeta_{j}^{n}\left|u\right\rangle_{j}. \tag{2.33}$$

Obviously, as n becomes large, the largest eigenvalue dominates the summation, i.e.

$$\left(\mathsf{H}\mathsf{H}^{\dagger}\right)^{n}\left|w\right\rangle \approx c_{p}\zeta_{p}^{n}\left|u\right\rangle_{p}, \tag{2.34}$$

allowing $\left|u\right\rangle_{p}$ to be easily found. Similarly, the same procedure applies to the right eigenvector $|v\rangle$, and thus the principal left and right eigenvector can be easily obtained using this so-called power method. In the algorithm, the next guesses for the amplitudes $|A\rangle$ and $|G\rangle$ are obtained by applying the power-method as:

$$\left(\left|A\right\rangle^{(q+1)}\right)^{*} = \left(\mathsf{H}\mathsf{H}^{\dagger}\right)^{n}\left(\left|A\right\rangle^{(q)}\right)^{*}, \qquad \text{and} \qquad \left|G\right\rangle^{(q+1)} = \left(\mathsf{H}^{\dagger}\mathsf{H}\right)^{n}\left|G\right\rangle^{(q)}. \tag{2.35}$$

While a better result for the eigenvectors can be obtained by applying the operators $\mathsf{H}\mathsf{H}^{\dagger}$ or $\mathsf{H}^{\dagger}\mathsf{H}$ several times, once per iteration is adequate in practice.

Because the presence of noise cannot be avoided in practice, analysing its effect on the retrieval algorithm is essential. The effect of noise on the retrieval algorithm has been discussed in great detail.[38,45] In general, it was found that the presence of some noise can actually improve the retrieval quality, due to the inherent redundancy in the spectrogram.[45] However, in the presence of somewhat larger amounts of noise, the algorithm does not return a satisfying solution. Therefore, the noise in the measured spectrogram must be reduced. Common sources of noise, such as stray light and biases

in dark current, are additive and can be easily removed by simple subtraction with a background spectrum. Corner suppression, that is, multiplication of the spectrogram with a radially symmetric super-Gaussian, may also improve the retrieval quality from additive noise. Fourier low-pass filtering of the two-dimensional Fourier transform of the measured spectrogram is also another common technique to suppress both additive and multiplicative noise.[45] The low-pass filtering must be done with great care such that high spatial frequencies corresponding to the actual phase fluctuations are not filtered out. Other more sophisticated image processing techniques, e.g. Wiener filtering, wavelet noise reduction, etc., may prove to be useful for noise suppression in the spectrogram.

2.6 Summary

The characterisation of ultrashort optical pulses is limited by the temporal resolution of currently available measurement devices. The broad nature of their spectrum cannot be directly used to retrieve their complex temporal amplitudes, due to the unsolvable one-dimensional phase retrieval problem. Attempts to solve this problem failed, mainly because they worked purely in either the temporal or spectral domain, creating an unsolvable one-dimensional phase retrieval problem. FROG solves this problem by measuring a time-frequency distribution, i.e. a spectrogram. Unlike previous attempts, this creates a solvable two-dimensional phase-retrieval problem. The complex amplitude of ultrashort pulses can be retrieved from a spectrogram by means of an iterative algorithm. A detailed description of this algorithm, which is based on the generalised projection method, has been given.

Due to the sensitivity it offers, SHG FROG has become a standard in laboratories worldwide. Sensitivity improvement can still be made possible by gating a weak ultrashort pulse with an intense well-characterised reference pulse, i.e. XFROG configurations. The cross-correlation between the pulses is still achieved by $\chi^{(2)}$ interactions, either SFG and DFG. A more general form of XFROG is blind-FROG, which does not require the reference pulse to be well-characterised. Instead, a blind-deconvolution algorithm can be used to retrieve the test pulse and the gate pulse simultaneously without *a priori* knowledge.

References

[1] R. Trebino and D. J. Kane, "Using Phase Retrieval to Measure the Intensity and Phase of Ultrashort Pulses: Frequency-Resolved Optical Gating," Journal of the Optical Society of America A **10**(5), 1101–1111 (1993).

[2] D. J. Kane and R. Trebino, "Characterization of Arbitrary Femtosecond Pulses Using Frequency-Resolved Optical Gating," IEEE Journal of Quantum Electronics **29**(2), 571–579 (1993).

[3] R. Trebino, K. W. DeLong, D. N. Fittinghoff, J. N. Sweetser, M. A. Krumbügel, and B. A. Richman, "Measuring Ultrashort Laser Pulses in the Time-Frequency Domain Using Frequency-Resolved Optical Gating," Review of Scientific Instruments **68**(9), 3277–3295 (1997).

[4] R. Trebino, ed., *Frequency-Resolved Optical Gating: The Measurement of Ultrashort Laser Pulses* (Kluwer Academic Publishers, Dordrecht, 2000).

[5] J. Paye, M. Ramaswamy, J. G. Fujimoto, and E. P. Ippen, "Measurement of the Amplitude and Phase of Ultrashort Light Pulses from Spectrally Resolved Autocorrelation," Optics Letters **18**(22), 1946–1948 (1993).

[6] K. W. DeLong, R. Trebino, J. Hunter, and W. E. White, "Frequency-Resolved Optical Gating with the Use of Second-Harmonic Generation," Journal of the Optical Society of America B **11**(11), 2206–2215 (1994).

[7] R. W. Gerchberg and W. O. Saxton, "A Practical Algorithm for the Determination of Phase from Image and Diffraction Plane Pictures," Optik **35**(2), 237–246 (1972).

[8] B. E. A. Saleh and M. C. Teich, *Fundamentals of Photonics* (John Wiley and Sons, Inc., Chichester, 1991).

[9] R. H. T. Bates, "On Phase Problems." Optik **51**(2), 161–170 (1978).

[10] R. H. T. Bates, "On Phase Problems. II," Optik **51**(3), 223–234 (1978).

[11] M. Maier, W. Kaiser, and J. Giordmaine, "Intense Light Bursts in the Stimulated Raman Effect," Physical Review Letters **17**(26), 1275–1277 (1966).

[12] J. H. Chung and A. M. Weiner, "Ambiguity of Ultrashort Pulse Shapes Retrieved From the Intensity Autocorrelation and the Power Spectrum," IEEE Journal on Selected Topics in Quantum Electronics **7**(4), 656–666 (2001).

[13] H. Schulz, H. Schüler, T. Engers, and D. V. der Linde, "Measurement of Intense Ultraviolet Subpicosecond Pulses Using Degenerate Four-Wave Mixing," IEEE Journal of Quantum Electronics **25**(12), 2580–2585 (1989).

[14] J. C. M. Diels, J. J. Fontaine, I. C. McMichael, and F. Simoni, "Control and Measurement of Ultrashort Pulse Shapes (in Amplitude and Phase) with Femtosecond Accuracy," Applied Optics **24**(9), 1270–1282 (1985).

[15] L. Cohen, *Time-Frequency Analysis* (Prentice Hall, New Jersey, 1995).

[16] R. H. T. Bates, "Fourier Phase Problems are Uniquely Solvable in More Than One Dimension. I: Underlying Theory," Optik **61**(3), 247–262 (1982).

[17] K. L. Garden and R. H. T. Bates, "Fourier Phase Problems are Uniquely Solvable in More Than One Dimension. II: One-Dimensional Considerations," Optik **62**(2), 131–142 (1982).

[18] W. R. Fright and R. H. T. Bates, "Fourier Phase Problems are Uniquely Solvable in More Than One Dimension. III: Computational Examples for Two Dimensions," Optik **62**(3), 219–230 (1982).

[19] R. P. Millane, "Phase Retrieval in Crystallography and Optics," Journal of the Optical Society of America A **7**(3), 394–411 (1990).

[20] J. R. Fienup, "Phase Retrieval Algorithms: A Comparison," Applied Optics **21**(15), 2758–2769 (1982).

[21] K. W. DeLong, D. N. Fittinghoff, and R. Trebino, "Practical Issues in Ultrashort-Laser-Pulse Measurement Using Frequency-Resolved Optical Gating," IEEE Journal of Quantum Electronics **32**(7), 1253–1264 (1996).

[22] J. N. Sweetser, D. N. Fittinghoff, and R. Trebino, "Transient-Grating Frequency-Resolved Optical Gating," Optics Letters **22**(8), 519–521 (1997).

[23] T. Tsang, M. A. Krumbügel, K. W. DeLong, D. N. Fittinghoff, and R. Trebino, "Frequency-Resolved Optical-Gating Measurements of Ultrashort Pulses Using Surface Third-Harmonic Generation," Optics Letters **21**(17), 1381–1383 (1996).

[24] G. Taft, A. Rundquist, M. M. Murnane, H. C. Kapteyn, K. W. DeLong, R. Trebino, and I. P. Christov, "Ultrashort Optical Waveform Measurements Using Frequency-Resolved Optical Gating," Optics Letters **20**(7), 743–745 (1995).

[25] G. Taft, A. Rundquist, M. M. Murnane, I. P. Christov, H. C. Kapteyn, K. W. DeLong, D. N. Fittinghoff, M. A. Krumbügel, J. N. Sweetser, and R. Trebino, "Measurement of 10-fs Laser Pulses," IEEE Journal of Selected Topics in Quantum Electronics **2**(3), 575–585 (1996).

[26] A. Baltŭska, M. S. Pshenichnikov, and D. A. Wiersma, "Amplitude and Phase Characterization of 4.5-fs Pulses by Frequency-Resolved Optical Gating," Optics Letters **23**(18), 1474–1476 (1998).

[27] P. O'Shea, M. Kimmel, X. Gu, and R. Trebino, "Increased-Bandwidth in Ultrashort-Pulse Measurement Using an Angle-Dithered Nonlinear-Optical Crystal," Optics Express **7**(10), 342–349 (2000).

[28] D. N. Fittinghoff, J. A. Squier, C. P. J. Barty, J. N. Sweetser, R. Trebino, and M. Müller, "Collinear Type II Second-Harmonic-Generation Frequency-Resolved Optical Gating for Use with High-Numerical-Aperture Objectives," Optics Letters **23**(13), 1046–1048 (1998).

[29] D. N. Fittinghoff, A. C. Millard, J. A. Squier, and M. Müller, "Frequency-Resolved Optical Gating Measurement of Ultrashort Pulses Passing Through a High Numerical Aperture Objective," IEEE Journal of Quantum Electronics **35**(4), 479–486 (1999).

[30] J. Jasapara and W. Rudolph, "Characterization of Sub-10-fs Pulse Focusing with High-Numerical-Aperture Microscope Objectives," Optics Letters **24**(11), 777–779 (1999).

[31] I. Almat-Roldán, I. G. Cormack, P. Loza-Alvarez, E. J. Gualda, and D. Artigas, "Ultrashort Pulse Characterisation with SHG Collinear-FROG," Optics Express **12**(6), 1169–1178 (2004).

[32] G. Stibenz and G. Steinmeyer, "Interferometric Frequency-Resolved Optical Gating," Optics Express **13**(7), 2617–2626 (2005).

[33] S. Linden, H. Giessen, and J. Kuhl, "XFROG – A New Method for Amplitude and Phase Characterization of Weak Ultrashort Pulses," Physica Status Solidi B **206**(1), 119–124 (1998).

[34] S. Linden, J. Kuhl, and H. Giessen, "Amplitude and Phase Characterization of Weak Blue Ultrashort Pulses by Downconversion," Optics Letters **24**(8), 569–571 (1999).

[35] D. T. Reid, P. Loza-Alvarez, C. T. A. Brown, T. Beddard, and W. Sibbett, "Amplitude and Phase Measurement of Mid-Infrared Femtosecond Pulses by Using Cross-Correlation Frequency-Resolved Optical Gating," Optics Letters **25**(19), 1478–1480 (2000).

[36] J. Y. Zhang, A. P. Shreenath, M. Kimmel, E. Zeek, R. Trebino, and S. Link, "Measurement of the Intensity and Phase of Attojoule Femtosecond Light Pulses Using Optical-Parametric-Amplification Cross-Correlation Frequency-Resolved Optical Gating," Optics Express **11**(6), 601–609 (2003).

[37] K. W. DeLong, R. Trebino, and W. E. White, "Simultaneous Recovery of Two Ultrashort Laser Pulses from a Single Spectrogram," Journal of The Optical Society of America B **12**(12), 2463–2466 (1995).

[38] D. J. Kane, G. Rodriguez, A. J. Taylor, and T. S. Clement, "Simultaneous Measurement of Two Ultrashort Laser Pulses from a Single Spectrogram in a Single Shot," Journal of the Optical Society of America B **14**(4), 935–943 (1997).

[39] B. Seifert, H. Stolz, and M. Tasche, "Nontrivial Ambiguities for Blind Frequency-Resolved Optical Gating and The Problem of Uniqueness," Journal of The Optical Society of America B **21**(5), 1089–1097 (2004).

[40] K. W. DeLong and R. Trebino, "Improved Ultrashort Pulse-Retrieval Algorithm for Frequency-Resolved Optical Gating," Journal of the Optical Society of America A **11**(9), 2429–2437 (1994).

[41] K. W. DeLong, D. N. Fittinghoff, R. Trebino, B. Kohler, and K. Wilson, "Pulse Retrieval in Frequency-Resolved Optical Gating Based on the Method of Generalized Projections," Optics Letters **19**(24), 2152–2154 (1994).

[42] D. J. Kane, "Real-Time Measurement of Ultrashort Laser Pulses Using Principal Component Generalized Projections," IEEE Journal of Selected Topics on Quantum Electronics **4**, 278–284 (1998).

[43] D. J. Kane, "Recent Progress Toward Real-Time Measurement of Ultrashort Laser Pulses," IEEE Journal of Quantum Electronics **35**(4), 421–431 (1999).

[44] D. C. Lay, *Linear Algebra and Its Applications*, 2nd ed. (Addison-Wesley, Harlow, England, 1999).

[45] D. N. Fittinghoff, K. W. DeLong, R. Trebino, and C. L. Ladera, "Noise Sensitivity in Frequency-Resolved Optical Gating Measurements of Ultrashort Pulses," Journal of the Optical Society of America B **12**(10), 1955–1967 (1995).

Chapter 3

Second-Harmonic Generation in Quasi-Phase-Matched Waveguides

As discussed in the previous chapter, FROG relies on nonlinear interactions to achieve the mixing between the test and the gate pulses. We are particularly interested in second-order nonlinear interactions, whose theoretical framework, with the emphasis on second-harmonic generation (SHG, the simplest among all) using continuous-wave (CW) sources, is briefly presented in this chapter. The framework starts with the description of Maxwell's equations, and the nonlinear polarisation, which are the fundamentals of this work, in Section 3.1. Qualitative descriptions of several second-order nonlinear interactions, including SHG, sum- and difference-frequency generation (SFG and DFG), are given in Section 3.2. Section 3.3 develops a more detailed analysis of CW SHG in bulk materials based on the coupled mode equations. Second-harmonic generation in waveguide is addressed in Section 3.4. Phase-matching, an important concept for second-order nonlinear interactions, is discussed in Section 3.5.

3.1 Maxwell's Equations and the Nonlinear Polarisation

The most fundamental equations which govern all of macroscopic electromagnetism, including the propagation of light, are the four macroscopic Maxwell's equations:[1]

$$\nabla \cdot \mathbf{D} = \rho_f, \tag{3.1a}$$

$$\nabla \times \mathbf{E} = -\frac{\partial \mathbf{B}}{\partial t}, \tag{3.1b}$$

$$\nabla \cdot \mathbf{B} = 0, \tag{3.1c}$$

$$\nabla \times \mathbf{H} = \mathbf{J} + \frac{\partial \mathbf{D}}{\partial t}. \tag{3.1d}$$

In this set of equations, **E** and **H** are the macroscopic electric and the magnetic field vectors, **D** and **B** are the electric displacement and the magnetic induction, and the quantities ρ_f and **J** are the free electric charge and the current density, which may be considered as the sources of the fields **E** and **H**. Most dielectric materials have no free electric charge, and hence we can set $\rho_f = 0$. We shall further assume that there is no external current such that $\mathbf{J} = 0$.

For a particular set of boundary conditions, Maxwell's equations [Eq. (3.1)] cannot be solved uniquely unless the relationship between **B** and **H** and that between **E** and **D** are known. To obtain a unique determination of the field vectors, Maxwell's equations must be supplemented by the constitutive equations,

$$\mathbf{D} = \varepsilon_0 \mathbf{E} + \mathbf{P}, \tag{3.2a}$$

$$\mathbf{B} = \mu_0 \mathbf{H} + \mathbf{M}, \tag{3.2b}$$

where **P** and **M** are the electric and the magnetic polarisations. We can set $\mathbf{M} = 0$ since the material we used is nonmagnetic. The origin of electric polarisation **P** lies at the microscopic level. When an electromagnetic field is present in matter, the electric field perturbs the motion of electrons and produces a polarisation **P** per unit volume. Assuming an instantaneous response of the material, the components P_α of the polarisation field **P** can be related to the components E_β of the electric field **E** via a power series:[1,2]

$$\begin{aligned} P_\alpha(\mathbf{r},t) = \varepsilon_0 \chi^{(1)}_{\alpha\beta}(\mathbf{r},t) E_\beta(\mathbf{r},t) + \varepsilon_0 \chi^{(2)}_{\alpha\beta\gamma}(\mathbf{r},t) E_\beta(\mathbf{r},t) E_\gamma(\mathbf{r},t) \\ + \varepsilon_0 \chi^{(3)}_{\alpha\beta\gamma\delta}(\mathbf{r},t) E_\beta(\mathbf{r},t) E_\gamma(\mathbf{r},t) E_\delta(\mathbf{r},t) + \cdots , \end{aligned} \tag{3.3}$$

where the quantities $\chi^{(n)}$, known as susceptibilities, arise from the material's atomic structure. As in any power series expansion, the susceptibility $\chi^{(n)}$ eventually decreases with successive terms, so that we need only to consider the highest order terms. The first term depends linearly on the electric field and defines the refractive index of the material, i.e. $n_{\alpha\beta} = \sqrt{1 + \chi^{(1)}_{\alpha\beta}}$. The rest of the terms can then be identified as the nonlinear polarisation field. Hence the polarisation field can be split into:

$$\mathbf{P} = \mathbf{P}^{\mathrm{L}} + \mathbf{P}^{\mathrm{NL}}, \tag{3.4}$$

where $\mathbf{P}^{\mathrm{L}}$ is the linearly dependent polarisation field, and $\mathbf{P}^{\mathrm{NL}}$ contains the nonlinear polarisation field. We next look more closely into the nonlinear polarisation field $\mathbf{P}^{\mathrm{NL}}$ and the nonlinear susceptibility $\chi^{(n)}$.

3.2 Second-Order Nonlinear Interactions

Since the susceptibilities $\chi^{(n)}$ are intrinsic properties of a material, their tensorial forms reflect the structural symmetry of the material. In all materials with inversion symmetry, such as liquids, gases, amorphous solids, and many crystals, i.e. the so-called centrosymmetric materials, the $\chi^{(2n)}$ tensor components must vanish. This vanishing $\chi^{(2n)}$ tensor results from the odd inversion symmetry of the electric field vector $\mathbf{E}$ and the electric polarisation vector $\mathbf{P}$. However, there exists an important class of materials known as ferroelectrics, of which Lithium Niobate is a member. These materials possess a spontaneous electric dipole moment $\mathbf{P}_s$ in zero external field,[1] which originates from the shift of an ion from a symmetrical site.[3] This symmetry-breaking results in nonzero $\chi^{(2)}$ tensor components,[4] which are responsible for the nonlinear interactions we are interested in.

Several second-order nonlinear interactions which result from $\chi^{(2)}$ are qualitatively described in this section. For linearly polarised light, which we restrict ourselves to, the scalar form of the nonlinear polarisation [Eq. (3.3)] for second-order nonlinear interactions is given by:

$$P(\mathbf{r},t) = \varepsilon_0 \chi^{(2)} E^2(\mathbf{r},t). \tag{3.5}$$

Let us consider an electric field that consists of two distinct frequency components, ω_1 and ω_2, which is represented in scalar form by:

$$E(\mathbf{r},t) = E_1 \exp\left[i(\mathbf{k}_1 \cdot \mathbf{r} - \omega_1 t)\right] + E_2 \exp\left[i(\mathbf{k}_2 \cdot \mathbf{r} - \omega_2 t)\right] + \text{c.c.}, \tag{3.6}$$

where $|\mathbf{k}_j| = \frac{\omega_j}{c}\varepsilon(\omega_j) = \frac{\omega_j}{c} n^2(\omega_j)$. With the above electric field, the second-order nonlinear polarisation [Eq. (3.5)] can be rewritten as follows:

$$\begin{aligned} P(\mathbf{r},t) = \varepsilon_0 \chi^{(2)} \Big\{ & E_1^2 \exp\left[2i(\mathbf{k}_1 \cdot \mathbf{r} - \omega_1 t)\right] + E_2^2 \exp\left[2i(\mathbf{k}_2 \cdot \mathbf{r} - \omega_2 t)\right] \\ & + 2E_1 E_2 \exp\left[i(\mathbf{k}_1 + \mathbf{k}_2) \cdot \mathbf{r} - i(\omega_1 + \omega_2)t\right] \\ & + 2E_1 E_2^* \exp\left[i(\mathbf{k}_1 - \mathbf{k}_2) \cdot \mathbf{r} - i(\omega_1 - \omega_2)t\right] + \text{c.c.} \Big\} + 2\varepsilon_0 \chi^{(2)} \Big[|E_1|^2 + |E_2|^2 \Big]. \end{aligned} \tag{3.7}$$

One readily identifies the different frequency components of the nonlinear polarisation

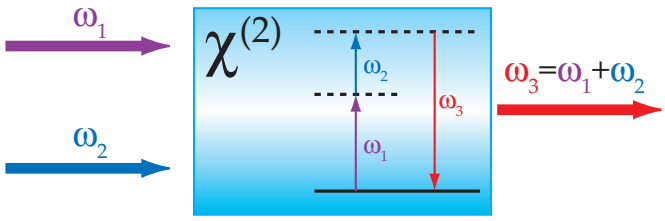

(a) Sum-frequency generation

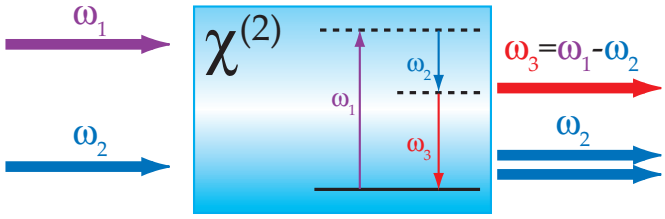

(b) Difference-frequency generation

Figure 3.1: Illustration of geometries and energy-level descriptions for two different second-order nonlinear interactions.

as being due to the following interactions:

$$E_1^2 \exp(-i2\omega_1 t), E_2^2 \exp(-i2\omega_2 t) \quad \text{second-harmonic generation,} \tag{3.8a}$$

$$E_1 E_2 \exp[-i(\omega_1 + \omega_2)t] \quad \text{sum-frequency generation,} \tag{3.8b}$$

$$E_1 E_2^* \exp[-i(\omega_1 - \omega_2)t] \quad \text{difference-frequency generation,} \tag{3.8c}$$

$$|E_1|^2 + |E_2|^2 \quad \text{optical rectification.} \tag{3.8d}$$

We are only interested in the first three interactions, collectively known as parametric interactions. These interactions produce electromagnetic radiations at a new frequency, whilst the last one, optical rectification, does not. Instead, it creates a static electric field inside the nonlinear material.[4] Although the three parametric interactions occur simultaneously (see Section 3.5), generally only one is preferred by the phase-matching condition in the nonlinear material to efficiently produce an output signal. Hence, we can consider them separately.

Let us first consider sum-frequency generation (SFG), whose geometry is illustrated in Fig. 3.1(a). The input electromagnetic field has two distinct frequencies ω_1 and ω_2 which interact with each other through the nonlinear material to produce an output wave at a frequency $\omega_3 = \omega_1 + \omega_2$. This interaction can be visualised in terms of photon virtual energy levels, as depicted in Fig. 3.1(a). In this process, photons with energy $\hbar\omega_1$ and $\hbar\omega_2$ are destroyed in the material to generate another one. The energy

conservation dictates that the produced photon has an energy $\hbar\omega_3 = \hbar\omega_1 + \hbar\omega_2$. In addition, the total momentum in the interaction must be conserved, i.e. $\mathbf{k}_3 = \mathbf{k}_1 + \mathbf{k_2}$. This requirement for conservation of momentum is also known as the phase-matching condition. For a collinear interaction, the conservation of momentum translates into $\omega_3 n(\omega_3) = \omega_1 n(\omega_1) + \omega_2 n(\omega_2)$. However, this condition is generally prevented from happening due to chromatic dispersion of the device, resulting in a phase-mismatch $\Delta k = k_3 - k_1 - k_2$. The phase-mismatch causes an alternation of power flow between the three waves, reducing the conversion efficiency. Ways to achieve phase-matching condition is given in Section 3.5. When the input waves are at a degenerate frequencies $\omega_1 = \omega_2$, this interaction simply reduces to SHG. Second-harmonic generation is analysed in more detail in the next sections. Both interactions are commonly used to generate electromagnetic waves at higher frequencies that are inaccessible by standard quantum transitions of atoms and/or molecules, such as frequencies in the ultraviolet.

The geometry of difference-frequency generation (DFG) is depicted in Fig. 3.1(b). The two input electromagnetic waves have distinct frequencies ω_1 and ω_2 which interact to produce an output wave at a frequency $\omega_3 = \omega_1 - \omega_2$. Both energy and momentum must be conserved in this interaction, i.e. $\hbar\omega_3 = \hbar\omega_1 - \hbar\omega_2$ and $\mathbf{k}_3 = \mathbf{k}_1 - \mathbf{k_2}$. Superficially, DFG looks similar to SFG. However, upon close inspection of the energy level diagrams in Fig. 3.1(b), not both input photons are destroyed. Only the photon at a higher frequency (ω_1) is destroyed, whilst a second photon at the lower frequency (ω_2) is created in the interaction. Therefore, the input wave at a lower frequency is amplified. For this reason, this process is also known as optical parametric amplification (OPA).[5]

In the energy level diagram for DFG depicted in Fig. 3.1(b), the emission of a photon with energy $\hbar\omega_3$ after the excitation by a $\hbar\omega_1$ photon is stimulated by the presence of a $\hbar\omega_2$ photon. However, spontaneous two photon emission ($\hbar\omega_2$ and $\hbar\omega_3$) that follows from the destruction of the $\hbar\omega_1$ photon can occur without the presence of the $\hbar\omega_2$ photon. This process is known as optical parametric fluorescence.[6] If the nonlinear material is put inside a resonator such that the device is being used multiple times, the electromagnetic waves at ω_2 and/or ω_3 can build up to an extremely high value. This device is known as an optical parametric oscillator (OPO).[7]

3.3 Continuous-Wave Second-Harmonic Generation

Having discussed second-order nonlinear interactions qualitatively in the previous section, we now provide a more formal mathematical treatment. The treatment is done through the formulation of coupled-mode equations for SHG, since it is the simplest among second-order nonlinear interactions, and is easily generalise to SFG. The formulation of coupled-mode equations starts with the electromagnetic waves, an important consequence of Maxwell's equations. Straightforward algebra from Maxwell's equations [Eq. (3.1)] and the constitutive relations [Eq. (3.2)] yields the following wave equation with an additional driving term originating from the nonlinear polarisation field:

$$\nabla \times \nabla \times \mathbf{E} + \frac{n^2}{c^2}\frac{\partial^2 \mathbf{E}}{\partial t^2} = -\mu_0 \frac{\partial^2 \mathbf{P}^{\mathrm{NL}}}{\partial t^2}. \tag{3.9}$$

Note that a similar wave equation can be derived for the magnetic field vector $\mathbf{H}$. The nonlinear driving term in the right-hand-side (RHS) of the above equation can be treated as a small perturbation to the linear differential equation on the left-hand-side (LHS), which has the effect of coupling light at different frequencies. This nonlinear coupling leads to an energy transfer between the different frequencies along the propagation direction. We write the solution to the above nonlinear wave equation as a sum of their various frequency components:

$$\mathbf{E}(\mathbf{r}, t) = \sum_j \mathbf{F}_j(x, y) A_j(z) \exp\left[i(\mathbf{k}_j \cdot \mathbf{r} - \omega_j t)\right] + \text{c.c.}, \tag{3.10}$$

where $\mathbf{F}_j(x, y)$ is the transverse field profile*, and $A_j(z)$ is the slowly varying amplitude of the electromagnetic wave at frequency ω_j. The angular frequency ω_j and the propagation wavevector $\mathbf{k}_j$ determine the phase velocity of the wave $v_p = \frac{\omega_j}{|\mathbf{k}_j|}$. The above solution can be normalised in the following way:

$$\frac{1}{2}\int_{x,y} \mathrm{Re}\left[(\mathbf{E} \times \mathbf{H}^*) \cdot \hat{z}\right] dxdy = \sum_j |A_j(z)|^2 = \sum_j \mathcal{P}_j(z), \tag{3.11}$$

where $\mathcal{P}_j(z)$ is the total power of the electric field at a frequency ω_j.

We need to find equations for the $A_j(z)$, which describes the evolution of each frequency component ω_j due to the nonlinear effects. Let us consider an electromagnetic wave at the fundamental-frequency (FF) ω_{FF} which interacts with itself and the $\chi^{(2)}$

*We have assumed that the transverse mode-profile does not change significantly during propagation along the interaction length, so that $\mathbf{F}$ is independent of z, i.e. $\mathbf{F} \neq \mathbf{F}(z)$.

material producing the following nonlinear polarisation wave at its second-harmonic frequency ($\omega_{\mathrm{SH}} = 2\omega_{\mathrm{FF}}$):

$$P_{\alpha}^{\mathrm{NL}}(\mathbf{r}, t; \omega_{\mathrm{SH}}) = \varepsilon_0 \chi_{\alpha\beta\gamma}^{(2)} E_{\beta}(\mathbf{r}, t; \omega_{\mathrm{FF}}) E_{\gamma}(\mathbf{r}, t; \omega_{\mathrm{FF}}). \tag{3.12}$$

For the sake of simplicity, we consider a FF wave with parallel or perpendicular polarisations to the optic axis of the crystal, such that only a single component of $\chi_{\alpha\beta\gamma}^{(2)}$, typically $\chi_{333}^{(2)}$, is being utilised. Substitution of Eq. (3.12) and Eq. (3.10) into Eq. (3.9), and utilisation of the slowly-varying amplitude approximation, yield the following coupled-mode equations that govern the evolution of the FF and SH amplitudes in the $\chi^{(2)}$ medium:[8]

$$\frac{dA_{\mathrm{FF}}(z)}{dz} = 2i\omega_{\mathrm{FF}}\kappa A_{\mathrm{FF}}^{*}(z) A_{\mathrm{SH}}(z) \exp\left(i\Delta k z\right), \tag{3.13a}$$

$$\frac{dA_{\mathrm{SH}}(z)}{dz} = i\omega_{\mathrm{SH}}\kappa A_{\mathrm{FF}}^{2}(z) \exp\left(-i\Delta k z\right), \tag{3.13b}$$

where $\Delta k = k(\omega_{\mathrm{SH}}) - 2k(\omega_{\mathrm{FF}})$ is the wavevector mismatch. The nonlinear coupling coefficients κ is given by

$$\kappa = d\sqrt{\frac{2\mu_0}{n_{\mathrm{FF}}^2 n_{\mathrm{SH}} c}}\sqrt{\frac{1}{S_{\mathrm{ovl}}}} \tag{3.14}$$

where $n_j = n(\omega_j)$ is the refractive index of the material, $d = \frac{1}{2}\chi_{\alpha\beta\gamma}^{(2)}$, and

$$S_{\mathrm{ovl}} = \frac{\int |\mathbf{F}_{\mathrm{SH}}|^2 \, dxdy \, \left(\int |\mathbf{F}_{\mathrm{FF}}|^2 \, dxdy\right)^2}{\left(\int |\mathbf{F}_{\mathrm{FF}}|^2 \, |\mathbf{F}_{\mathrm{SH}}| \, dxdy\right)^2} \tag{3.15}$$

is called the effective overlap area between the transverse field profiles of the FF and the SH waves.

Although Eq. (3.13) can be solved analytically,[9] their solution is far from simple. A simple solution would be beneficial as it would provide physical understanding of the process. If the FF wave has sufficiently low input power, such that the change in its power level is less than 20% throughout the interaction length, it can then be considered undepleted, i.e. $A_{\mathrm{FF}}(z) \approx A_{\mathrm{FF}}$. Hence, the generated SH power in a material of length L can be obtained by direct integration of Eq. (3.13b):

$$\mathcal{P}_{\mathrm{SH}}(L) = \left|\int_0^L \frac{dA_{\mathrm{SH}}(z)}{dz} dz\right|^2 = \left(\omega_{\mathrm{SH}}\kappa_{\mathrm{SH}}\right)^2 P_{\mathrm{FF}}^2 L^2 \, \mathrm{sinc}^2\left[\Delta k \frac{L}{2}\right], \tag{3.16}$$

where $\mathcal{P}_{\mathrm{FF}}^2 = |A_{\mathrm{FF}}(0)|^2$. Characterisation of a $\chi^{(2)}$ material usually involves the generation of the tuning curve, which is the measured SH power as a function of the phase-mismatch, as plotted in Fig. 3.2. For the ideal case, the phase-mismatch variation can

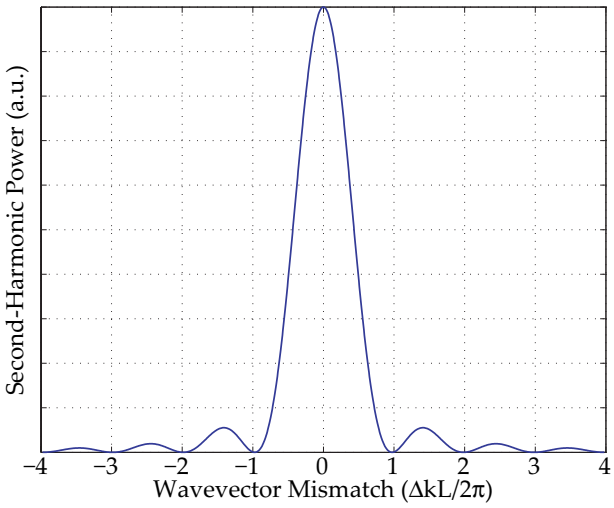

Figure 3.2: Second-Harmonic Generation tuning curve.

be achieved by tuning the temperature of the material or the input FF wavelength. Note that the maximum generated SH power occurs when phase-matching ($\Delta k = 0$) is achieved, as expected. Methods to achieve this will be discussed in details in Section 3.5. As is apparent from Eq. (3.16), for $\Delta k = 0$, the resulting power scales quadratically with the interaction length. We define a nonlinear conversion efficiency as follows:

$$\eta_{\mathrm{NL}} = \frac{\mathcal{P}_{\mathrm{SH}}(L)}{\mathcal{P}_{\mathrm{FF}}^2} = \eta_{\mathrm{nor}} L^2 \,\mathrm{sinc}^2\left[\Delta k \frac{L}{2}\right], \tag{3.17}$$

where the normalised conversion efficiency η_{nor}, a measure of the intrinsic quality of the $\chi^{(2)}$ material which is independent of the input FF power and the interaction length, is given by:

$$\eta_{\mathrm{nor}} = \left[\omega_{\mathrm{SH}} \kappa_{\mathrm{SH}}\right]^2 . \tag{3.18}$$

Its units are usually given as $\%[\mathrm{W\,cm^2}]^{-1}$.

The full-width at half-maximum (FWHM) bandwidth of the SHG tuning curve [Eq. (3.16)] is given by:

$$\Delta[\Delta k] = \frac{5.57}{L}, \tag{3.19}$$

as $\mathrm{sinc}^2(1.39) \approx 0.5$. Note that it scales inversely with the interaction length. Similarly, the wavelength bandwidth is given by:

$$\Delta\lambda = \frac{5.57}{L} \left|\frac{\partial \Delta k}{\partial \lambda}\right|^{-1}_{\lambda=\lambda_0} . \tag{3.20}$$

It can be easily seen that the generated SH power [Eq. (3.16)] is inversely proportional to the beam spot size [Eq. (3.14)]. Therefore, a high conversion efficiency can be

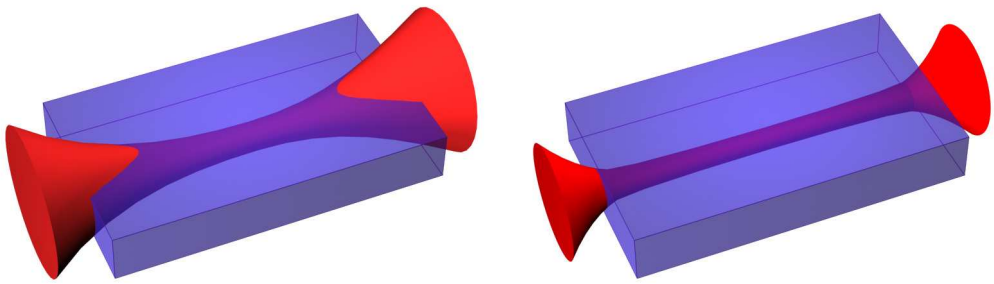

(a) (b)

Figure 3.3: Illustration of the laser beam propagation with Gaussian intensity profile in a) bulk material and b) guided-wave configuration.

theoretically achieved by using a laser beam with a spot size as small as possible. In reality, however, the spot size of the beam cannot be chosen arbitrarily due to the wave nature of light. As the beam spot size is focused to a spot as small as possible near the centre of the nonlinear material, diffraction results in a much larger beam spot size at the end of the material, and thus the whole length of the material is not optimally used for the nonlinear interaction [see Fig. 3.3(a)]. Boyd and Kleinman[8] showed that the optimum focusing condition is tighter than the confocal focusing, i.e. a focusing condition where the spot size at the end of the material is $\sqrt{2}$ times that at the centre. For this focusing, the beam spot size is given by $S_{\text{bulk}} \approx \frac{\lambda L}{2n}$, causing the maximum SH power to only scale linearly with the interaction length.

3.4 Guided-Wave Configurations

The Gaussian beam diffraction problem can be overcome by guided-wave configurations. In guided-wave configurations, a small beam size can be maintained for a long interaction length, since the electromagnetic radiation is confined in a waveguide, as illustrated in Fig. 3.3(b). The efficiency improvement gained by resorting to guided-wave configurations can be estimated as follows:

$$\frac{\eta_{\text{waveguide}}}{\eta_{\text{bulk}}} = \frac{S_{\text{bulk}}}{S_{\text{waveguide}}} = \frac{\lambda L}{2nS_{\text{waveguide}}}. \tag{3.21}$$

Using a typical $LiNbO_3$ waveguide mode size of $\sim 40\,\mu\text{m}^2$ at wavelengths in the $1.55\,\mu$m-band, an estimated improvement ratio of $10^2 L$ is obtained, where L is in cm. A 1 cm-long

interaction length should therefore provide an efficiency improvement by two orders of magnitude over bulk materials.

Waveguides are obtained by creating a localised perturbation of higher refractive index than the surroundings. Such structures do not allow electromagnetic radiation to propagate freely. Instead, the electromagnetic radiation propagates as discrete modes inside the waveguide. The solution to the wave equation for electric field $\mathbf{E}(\mathbf{r},t)$ in such a structure is given by

$$\mathbf{E}(\mathbf{r},t) = \sum_q \sum_j \mathbf{F}_j^{(q)}(x,y) A_j^{(q)}(z) \exp\left[i(\omega_j t - \beta_j^{(q)} z)\right] + \text{c.c}, \tag{3.22}$$

where q denotes the mode indices, and $\beta_j^{(q)} = \frac{\omega_j}{c}\mathcal{N}^q$ is the propagation wavevector of mode q with frequency ω_j inside the waveguide, with $\mathcal{N}$ being the effective refractive index of the propagating mode.

The coupled-mode equations describing the evolution of the FF and the SH waves inside the waveguide are formally identical to Eq. (3.13), and are given by:

$$\frac{dA_{\text{FF}}(z)}{dz} = 2i\omega_{\text{FF}}\kappa A_{\text{FF}}^*(z) A_{\text{SH}}(z) \exp\left(i\Delta\beta z\right), \tag{3.23a}$$

$$\frac{dA_{\text{SH}}(z)}{dz} = i\omega_{\text{SH}}\kappa A_{\text{FF}}^2(z)\ \exp\left(-i\Delta\beta z\right). \tag{3.23b}$$

In deriving the above equations, we consider only the interactions between fundamental modes, since these give the highest conversion efficiency, and thus have omitted the mode indices. There are two main differences in the above equations compared to Eq. (3.13): The bulk material wavevector mismatch Δk is replaced by the waveguide wave vector mismatch $\Delta\beta = \beta(\omega_{\text{SH}}) - 2\beta(\omega_{\text{FF}})$, and the nonlinear coupling coefficient, similar to Eq. (3.14), is given by:

$$\kappa = d\sqrt{\frac{2\mu_0}{\mathcal{N}_{\text{FF}}^2 \mathcal{N}_{\text{SH}} c}}\sqrt{\frac{1}{S_{\text{ovl}}}}, \tag{3.24}$$

where $\mathcal{N}$ is the effective index of the fundamental modes of the waveguide, and the effective overlap area S_{ovl} is given by Eq. (3.15). Note also that the effective overlap area in waveguide can be optimised to improve the conversion efficiency by proper design of the waveguide structure.

3.5 Achieving Phase-Matching

As described before, the interaction between the FF wave and the material produces a polarisation wave at its SH [see Eq. (3.12)]. The polarisation wave travels with the same

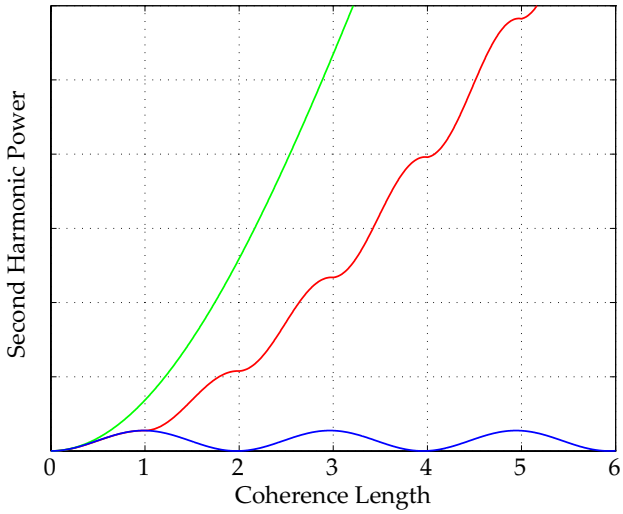

Figure 3.4: Power of the SH wave as a function of the propagation length in the units of coherence length for non-phase-matching (blue), phase-matching (green) and quasi-phase-matching (red) conditions.

phase velocity as the FF wave, determined by $\mathcal{N}_{\mathrm{FF}}$, which is the effective refractive index of the waveguide at ω_{FF}. The polarisation wave then radiates the SH wave which travels at phase velocities determined by $\mathcal{N}_{\mathrm{SH}}$, the effective refractive index of the waveguide at ω_{SH}. When the phase velocities of both the FF and SH wave are equal, then the power flows unidirectionally from the FF wave to the SH wave. Therefore, the amplitude of the SH wave grows monotonically along the interaction length as illustrated by the green curve in Fig. 3.4. As previously mentioned, this condition is called phase-matching, and corresponds to $\Delta\beta = \frac{4\omega_{\mathrm{FF}}}{c}(\mathcal{N}_{\mathrm{SH}} - \mathcal{N}_{\mathrm{FF}}) = 0$ or $\mathcal{N}_{\mathrm{FF}} = \mathcal{N}_{\mathrm{SH}}$.

In general, however, $\mathcal{N}_{\mathrm{SH}} \neq \mathcal{N}_{\mathrm{FF}}$ due to chromatic dispersion in most materials and waveguides, including Lithium Niobate (see Fig. 3.5, for example). Hence, the FF and the SH waves travel at different phase-velocities, so that there is a continuous phase slip between both waves. This phase slip leads to the alternation of power flow between the FF and the SH waves, as illustrated by the blue curve in Fig. 3.4. The alternation of the power flows yields a growth and decay cycle of the SH wave along the interaction length. The length over which the FF and the SH waves accumulate a π phase difference is called the coherence length:

$$l_c = \frac{\pi}{\Delta\beta} = \frac{\lambda}{4\left[\mathcal{N}(\omega_{\mathrm{SH}}) - \mathcal{N}(\omega_{\mathrm{FF}})\right]}, \tag{3.25}$$

which is a half-period of the growth and decay cycle of the SH wave.

A simple and common way to achieve phase-matching is by utilising the mater-

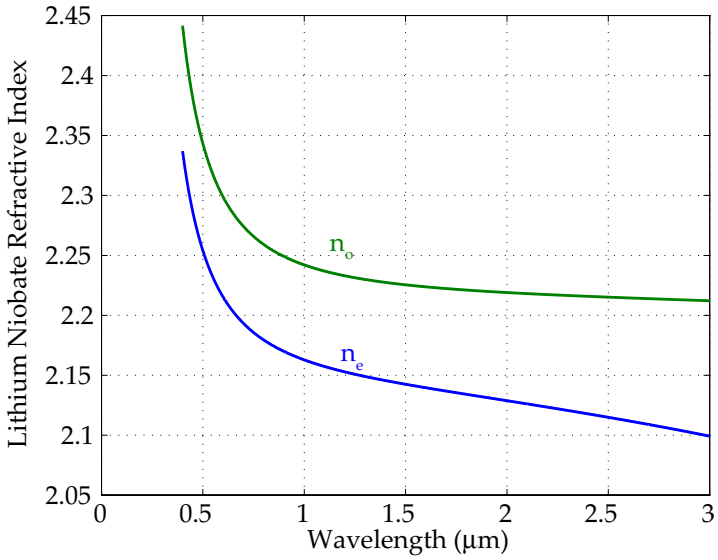

Figure 3.5: The ordinary (green) and extraordinary (blue) refractive index of Lithium Niobate at a temperature $T = 100\,^0$C as calculated from the Sellmeier equations in Refs. 10 and 11, respectively.

ial birefringence.[12,13] Different refractive indices experienced by interacting waves of different polarisations in birefringent material can result in phase-matching, $\Delta\beta = 0$. However, this method restricts the choice of the $\chi^{(2)}$ tensor component that can be used. In addition, birefringence phase-matching usually involves some angle of propagation θ relative to the optic axis, resulting in spatial and Poynting-vector walk-offs. These walk-offs limit the effective interaction length, reducing the conversion efficiency. The so-called ordinary and extraordinary refractive indices of Lithium Niobate are shown in Fig. 3.5. For birefringent phase-matching in Lithium Niobate, the FF wave is polarised perpendicular to the z-axis of the crystal $[n_{\rm FF} = n_o(\omega_{\rm FF})]$, whereas the SH wave is polarised parallel to the z-axis of the crystal $[n_{\rm SH} = n_e(\omega_{\rm SH}, \theta)]$. Unfortunately, due to chromatic dispersion, the phase-matching condition $n_o(\omega_{\rm FF}) = n_e(\omega_{\rm SH}, \theta)$ is only possible at certain wavelengths. In this case, the effective nonlinear coefficient is given by $d_B = \frac{1}{2}\chi^{(2)}_{311}$.

An alternative scheme, called **quasi-phase-matching** (QPM), to compensate the continuous phase slip was proposed by Armstrong *et al.*[9] The scheme involves a repeated inversion of the relative phase between the FF and the SH waves after an odd number of coherence lengths, in order to maintain the growth of the SH wave along the interaction length. The repeated inversion can be achieved by changing the sign of the nonlinear

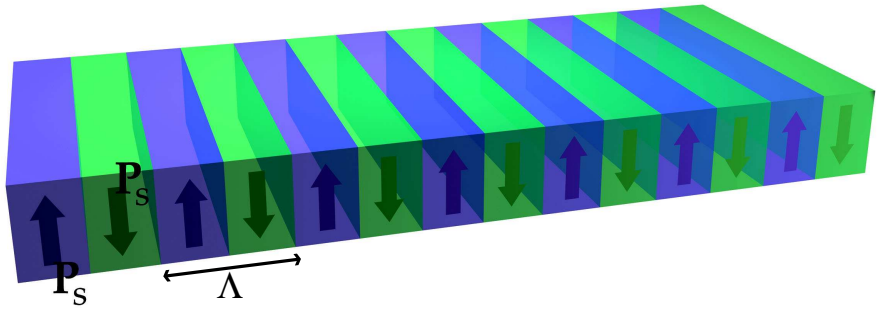

Figure 3.6: Illustration of periodic inversion of the spontaneous polarisation $\mathbf{P}_s$ in ferroelectrics.

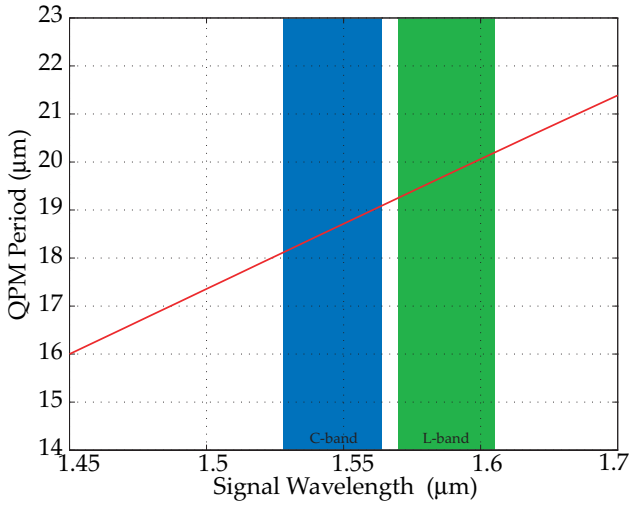

Figure 3.7: The required QPM period for SHG as a function of the phase-matching wavelength, as calculated from the Sellmeier equation for the extraordinary refractive index[11] at temperature $T = 100\,^0$C. C and L telecommunications bands are highlighted in blue and green, respectively.

coefficient. In ferroelectrics, this can be done by reversing the spontaneous polarisation $\mathbf{P}_s$ periodically along the interaction length as illustrated in Fig. 3.6. This, for example, can be achieved by applying a spatially periodic external electric field onto a ferroelectric material, i.e. electric-field poling. The most rapid conversion, of course, is achieved by reversing $\mathbf{P}_s$ every coherence length l_c. The evolution of the SH wave along the interaction length is shown by the red curve in Fig. 3.4.

In a Fourier space picture, it can be easily recognised that the compensation is achieved by a periodic structure whose reciprocal lattice vector is equivalent to the phase-mismatch between the FF and the SH waves. Periodic inversion of the nonlinear

coefficient along the interaction length can be represented by the following Fourier series:

$$d(z) = d \sum_{q=-\infty}^{\infty} \frac{2}{q\pi} \mathrm{e}^{iK_q z}, \tag{3.26}$$

where $K_q = \frac{2\pi q}{\Lambda}$ is a reciprocal lattice vector of the periodic structure with periodicity Λ. In the QPM case, the wavevector mismatch $\Delta\beta$ in Eq. (3.23) must then be replaced with

$$\Delta\beta_{\mathrm{QPM}} = \Delta\beta - K_q. \tag{3.27}$$

It follows then that only the Fourier component of the nonlinear coefficient [Eq. (3.26)] that is phase-matched ($\Delta\beta_{\mathrm{QPM}} = 0$) contributes significantly to the nonlinear interaction, so that the nonlinear coefficient in Eq. (3.24) has to be replaced with

$$d \to d_{\mathrm{QPM}} = \frac{2d}{q\pi}. \tag{3.28}$$

As expected, maximum nonlinear interaction efficiency is achieved from the first order Fourier component ($q = 1$). The tuning curve for SHG with QPM is identical to that without QPM as shown in Fig. 3.2.

The QPM scheme allows one to access $\chi^{(2)}_{333}$, the highest $\chi^{(2)}$ tensor component of Lithium Niobate, when both the FF and SH waves are polarised parallel to the z-axis of the crystal. Although the QPM scheme only allows 64% $\left(\frac{2}{\pi}\right)$ of $\chi^{(2)}_{333}$, it still provides a significant improvement of about 16 times over the birefringent phase-matching, considering $d_{\mathrm{B}} = \frac{1}{2}\chi^{(2)}_{311} = 2.1\,\mathrm{pm/V}$ and $d_{\mathrm{QPM}} = \frac{1}{\pi}\chi^{(2)}_{333} = 8.6\,\mathrm{pm/V}$. More importantly, in contrast to birefringent phase-matching, QPM can be achieved at any frequencies by appropriate choice of the gratings period. For example, Fig. 3.7 shows the required QPM period for the second-harmonic conversion from the C and L telecommunications bands, periods which are easily achieved using standard electric-field poling techniques.

We have so far assumed that we have a perfectly periodic QPM structure and a homogeneous waveguide. However, in practice, such conditions cannot be easily met. Imperfections in fabrications yield randomly varying QPM structures and inhomogeneous waveguides. In addition, spatially varying temperature during experiments also affects the homogeneity of the waveguides. These result in a position-dependent phase-mismatch along the length of the devices.[14–16] In such conditions, the solution given by Eq. (3.16) no longer holds, instead, the tuning curve is distorted. This distortion can be viewed as a redistribution of the area under the tuning curve as a function of $\frac{1}{2}\Delta\beta L$, resulting from the spatially dependent phase-matching condition along the interaction

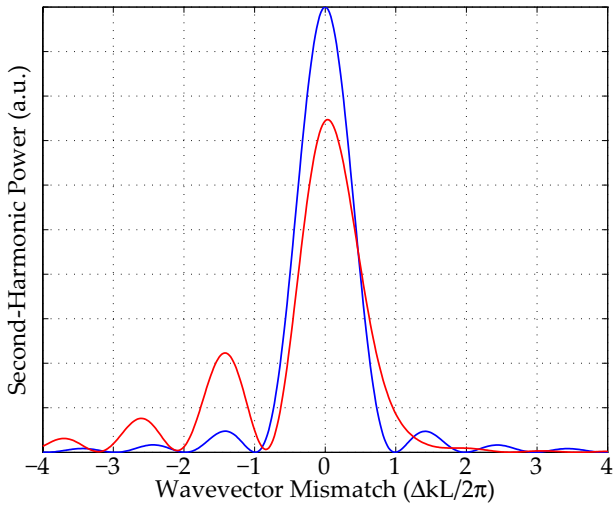

Figure 3.8: Nonideal SHG tuning curve (red lines) normalised to the peak conversion efficiency of an ideal SHG tuning curve (blue lines).

length. In other words, the imperfections in QPM waveguide devices result in a reduction of the conversion efficiency and a broadening of the SHG tuning curve. This fact implies that the total device length is not effectively used in the nonlinear interaction. Therefore, the FWHM bandwidth [Eq. (3.19)] is often used as a measure of the effective interaction length.[14] Figure 3.8 shows a comparison between a nonideal QPM waveguide device and an ideal one with identical interaction lengths. Here the broadening of the nonideal QPM waveguide device can be easily seen. Unfortunately, little can be done to suppress the effect of the imperfections on the QPM structure. However, in waveguides, their dimensions can be optimised in such a way to yield a greater tolerance on the spatially varying phase-matching conditions arising from their fabrication imperfections and experimental conditions (spatially varying temperature).[17,18]

3.6 Summary

General qualitative descriptions of second-order nonlinear interactions are presented in this chapter. Among second-order nonlinear interactions, SHG is the simplest, and its theoretical framework was developed in this chapter. The analysis revealed that the efficiency of the nonlinear interaction reaches maximum when the phase-matching condition is achieved. Quasi-phase-matching technique is an elegant scheme to achieve this condition by introducing an artificial periodic structure. The phase-matching wavelength can be chosen by engineering the structure period. The efficiency can be further

enhanced by using guided-wave configuration in order to avoid the Gaussian beam diffraction, providing tight optical confinements and long interaction lengths.

References

[1] J. D. Jackson, *Electrodynamics* (John Wiley & Sons, Inc., New York, 1962).

[2] N. Bloembergen, *Nonlinear Optics* (W.A. Benjamin, New York, 1965).

[3] D. Mills, *Nonlinear Optics: Basic Concepts* (Springer-Verlag, New York, 1998).

[4] R. W. Boyd, *Nonlinear Optics* (Academic Press Ltd., London, 1992).

[5] R. Baumgartner and R. L. Byer, "Optical Parametric Amplification," IEEE Journal of Quantum Electronics **15**(6), 432–444 (1979).

[6] S. E. Harris, M. K. Osman, and R. L. Byer, "Observation of Tunable Optical Parametric Fluorescence," Physical Review Letters **18**, 732–734 (1967).

[7] M. H. Dunn and M. Ebrahimzadeh, "Parametric Generation of Tunable Light from Continuous-Wave to Femtosecond Pulses," Science **286**, 1513–1517 (1999).

[8] G. D. Boyd and D. A. Kleinman, "Parametric Interaction of Focused Gaussian Light Beams," Journal of Applied Physics **39**(8), 3597–3639 (1968).

[9] J. A. Armstrong, N. Bloembergen, J. Ducuing, and P. S. Pershan, "Interactions Between Light Waves in a Nonlinear Dielectric," Physical Review **127**(6), 1918 (1962).

[10] M. Lawrence, "A Temperature-Dependent Dispersion Equation for Congruently Grown Lithium Niobate," Optical and Quantum Electronics **16**, 373 (1984).

[11] D. Jundt, "Temperature-Dependent Sellmeier Equation for The Index of Refraction, n_e, in Congruent Lithium Niobate," Optics Letters **22**(20), 1553 (1997).

[12] J. A. Giordmaine, "Mixing of Light Beams in Crystals," Physical Review Letters **8**(1), 19–20 (1962).

[13] P. D. Maker, R. W. Terhune, M. Nisenoff, and C. M. Savage, "Effects of Dispersion and Focusing on the Production of Optical Harmonics," Physical Review Letters **8**(1), 21–22 (1962).

[14] M. M. Fejer, G. A. Magel, D. H. Jundt, and R. L. Byer, "Quasi-Phase-Matched Second Harmonic Generation: Tuning and Tolerances," IEEE Journal of Quantum Electronics **28**(11), 2631 (1992).

[15] S. Helmfrid and G. Arvidsson, "Influence of Randomly Varying Domain Lengths and Nonuniform Effective Index on Second-Harmonic Generation in Quasi-Phase-Matching Waveguides," Journal of the Optical Society of America B **8**(4), 797–804 (1991).

[16] S. Helmfrid, G. Arvidsson, and J. Webjörn, "Influence of Various Imperfections on the Conversion Efficiency of Second-Harmonic Generation in Quasi-Phase-Matching Lithium Niobate Waveguides," Journal of the Optical Society of America B **10**(2), 222–229 (1992).

[17] E. J. Lim, S. Matsumoto, and M. M. Fejer, "Noncritical Phase Matching for Guided-Wave Frequency Conversion," Applied Physics Letters **57**(22), 2294–2296 (1990).

[18] M. L. Bortz, S. J. Field, M. M. Fejer, D. W. Nam, R. G. Waarts, and D. F. Welch, "Noncritical Quasi-Phase-Matched Second Harmonic Generation in an Annealed Proton-Exchanged $LiNbO_3$ Waveguide," IEEE Transactions on Quantum Electronics **30**(12), 2953–2960 (1994).

Chapter 4

Quasi-Phase-Matched Lithium Niobate Waveguide Devices

The devices used throughout my research work consists of buried waveguides on periodically-poled Lithium Niobate (PPLN). Their description, fabrication, and properties are described in this chapter. Section 4.1 describes the structure and presents a short description of its fabrication. The device fabrication was done by Dr. Katia Gallo with help from Dr. Corin Gawith in Prof. Peter Smith's group. A more detailed overview of the fabrication technique for the creation of buried waveguide is given in Section 4.2. Since this fabrication technique was not established at the ORC, some work was spent on its characterisation, which is presented in Section 4.3.

A large portion of this research work was spent on setting up characterisation tools and using them on the fabricated device. These enabled us to gain knowledge of the device properties in order to optimise the device performance in the future. The characterisation was done by myself and Dr. Katia Gallo. The linear properties of the device are associated with the waveguide structure. These properties comprise transverse field profiles and propagation losses, and are presented in section 4.4. In section 4.5 that follows, second-order nonlinear properties of the device are being assessed through nonlinear interactions, such as SHG (see Chapter 3) and sum-frequency generation (SFG).

4.1 Device Overview

As mentioned above, the device used throughout this research work consists of uniform QPM structures and buried waveguides. Figure 4.1 shows a three-dimensional model of our device, while a microscopic photograph of its top surface is shown in Fig. 4.2. The fabrication of QPM structures began by defining the gratings pattern on the $-z$-face of

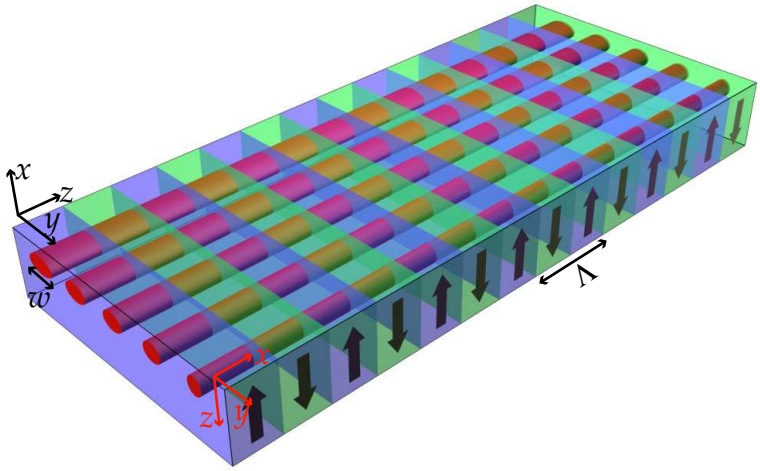

Figure 4.1: Three-dimensional model of the device. The QPM structure of period Λ and the waveguides of nominal width w are shown. The crystal axes are shown in red, whilst the electromagnetic wave axes are in black.

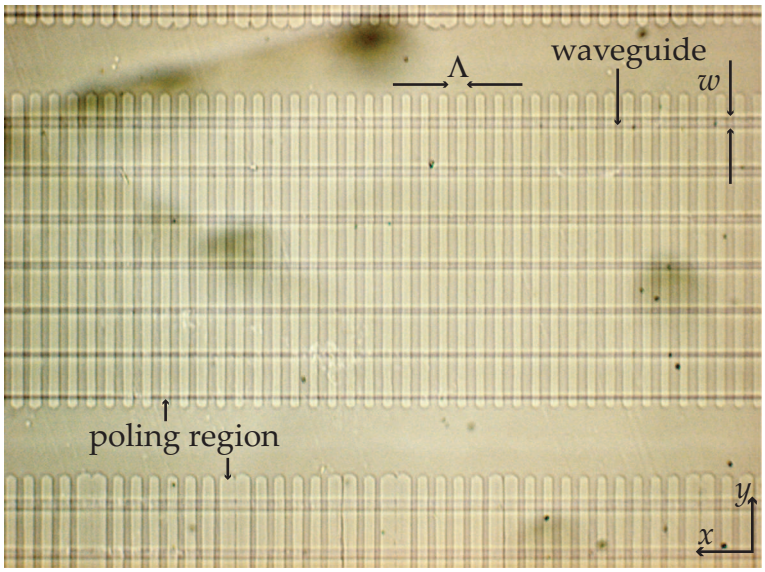

Figure 4.2: Top microscopic photograph of the device. The QPM structure and the waveguides are clearly visible. The crystal axes direction is also shown.

the crystal using a standard photolithographic technique, followed by the application of an external electric field at room temperature using a conductive gel as the electrode,[1] resulting in periodic inversions along the x-axis of the crystal with periods ranging from 14.5 to 16.5 μm with a 0.5 μm step. The poling was performed by Dr. Katia Gallo with help from Dr. Corin Gawith in Prof. Peter Smith's group. Afterward, buried channel waveguides perpendicular to the QPM structures on the $-z$-face of the crystal were fabricated by Dr. Katia Gallo using a selective proton exchange process, followed by annealing and reverse proton exchange processes following the work of Parameswaran, *et al.*,[2] as described in Section 4.2. The precise fabrication parameters are given below, whilst a detailed description of the process is given in the next section. The periodically-poled $LiNbO_3$ (PPLN) was first immersed in a Benzoic acid melt for 31 hours at 160 ^{0}C, resulting in a proton-rich layer of $\sim$ 1.2 μm thick. The sample was subsequently annealed in air for 8 hours at 328 ^{0}C, followed by a reverse exchange in an eutectic melt of $LiNO_3$:KNO_3:$NaNO_3$ with a mole ratio of 37.5:44.5:18.0 for 10 hours at 328^0 C, resulting in the realisation of buried waveguides. These buried waveguides only support electromagnetic wave polarised parallel to the crystal optic axis, i.e. the so-called transverse magnetic (TM) polarisation. Each of the fabricated waveguides have nominal widths, defined by the mask widths used during the selective proton exchange, ranging from 4 to 10 μm with a 1 μm step. One set of these 7 waveguides with the same QPM period are clearly shown in Fig. 4.2. These combination of QPM structures and waveguides were repeated three times on the sample, such that there were $7 \times 5 \times 3$ waveguides in total. This redundancy was made due to the uncertainties in the fabrication process in order to ensure that at least one device is suitable for our experiments. Finally, the end-faces of the device (x-faces of the crystal) were polished, resulting in a device with a total length of 2.6 cm.

4.2 Waveguide Fabrication Overview

As described in the previous section, the fabrication technique to produce buried waveguides on $LiNbO_3$ adopted by our group in the ORC consists of three steps: proton exchange, annealing and reverse exchange, as summarised in Fig. 4.3. This technique has advantages over others, such as titanium indiffusion,[3] heavy-ion exchange (silver[4] and thallium,[5] for example), direct writing,[6] and proton exchange. The advantages can be listed as follows: (1) It is consistently reproducible, and the optical properties of

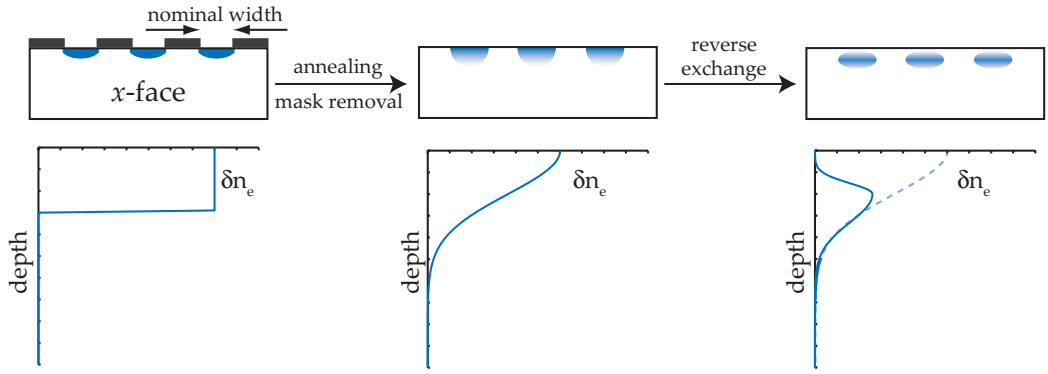

Figure 4.3: Summary of the waveguide fabrication process, involving proton exchange, annealing, and reverse exchange. Corresponding refractive index profile evolutions are also shown.

the resulting waveguides can be tailored by varying the fabrication parameters, (2) it is done at a relatively low temperature, and (3) it gives relatively high refractive index changes (≈ 0.02) with low propagation losses ($< 1\,\mathrm{dB/cm}$). The fabrication steps will be briefly reviewed here.

4.2.1 Proton Exchange

Waveguide fabrication on $LiNbO_3$ using proton-exchange (see Fig. 4.3, left-most picture) was firstly demonstrated by Jackel *et.al.*[7] The process involves the immersion of the $LiNbO_3$ substrate into an acid bath which acts as the proton source at $150^0 - 300^0$C. Immersion of the substrate into weak acids yields in incomplete exchange of the $LiNbO_3$, resulting in a proton rich ($H_xLi_{1-x}NbO_3$) layer on the surface. The proton rich layer results in an increase of extraordinary refractive index and a decrease of ordinary refractive index.[7,8] Waveguides can be made in both x-cut and z-cut crystals, while the y-faces are strongly etched by the acid and thus cannot guide any light. Benzoic acid (C_6H_5COOH, $K_\alpha = 6.46 \times 10^{-5}$) is a well established proton source and has been widely used. The acid is solid at room temperature, stable throughout its liquid phase, and its acidity can be easily controlled by the addition of lithium benzoate. The low melting point of 122^0C also enables an exchange to be performed at a relatively low temperature.

Proton-exchanged (PE) waveguides are known to be unstable at room temperature, i.e. the refractive index profile changes as a function of time at room temperature.[9] The metastable nature at room temperature is associated to the presence of a high-proton

concentration phase (the so-called β-phase) of $H_xLi_{1-x}NbO_3$.[10] This crystallographic phase exhibits relatively high propagation losses, and an almost complete erasure of the nonlinear coefficient, thus forming a dead layer on the surface.[11,12] Hence, such waveguides are unsuitable for nonlinear interactions, and thus further treatment must be done.

4.2.2 Annealing

Post-exchange annealing of the proton exchanged samples (see Fig. 4.3, middle picture) is necessary to produce stable and efficient waveguides. The annealing is usually done by heating the sample at $250^0 - 450^0$C,[13] in an oxygen-rich environment to prevent the evaporation of Li_2O and/or H_2O from the surface, as it was found that evaporation of certain species from the surface during annealing[13,14] can have a detrimental effect on the kinetics and properties of APE waveguides. Annealing leads to the diffusion of the protons into the substrate from the proton-rich layer, shifting from the β-phase to the κ-phase and finally to the stress-free phase (the so-called α-phase).[10] This diffusion of protons yields waveguides with a graded-profile and a reduction of the peak refractive index Δn_e (see Fig. 4.3).[15] The process is accompanied by a recovery of the nonlinearity within the initial exchange layer,[16,17] enabling higher conversion efficiency for nonlinear interactions within the waveguide. The optical properties of the waveguide can be manipulated by varying the temperature and the time of annealing.[18,19]

4.2.3 Reverse Exchange

The final step in the process is the reverse exchange. Reverse proton exchange of PE or APE waveguides (see Fig. 4.3, right-most picture) leads to the realisation of buried waveguides. In addition to the creation of a buried waveguide, an ordinary index waveguide is created at the surface by using the PE region as an index barrier. Buried waveguides in PE:$LiNbO_3$ by reverse-exchange were firstly demonstrated by Ganshin *et al.*[20] In order to reintroduce lithium at the surface, the PE or APE sample is immersed in a lithium rich melt. For this purpose, lithium nitrate is chosen for the melt due to its stability for long-duration usage, but reverse-exchange in $LiNO_3$ alone damages the surface of the crystal. It was discovered that mixtures of nitrates containing $LiNO_3$ do not damage the surface of $LiNbO_3$. A mixture of KNO_3 and $NaNO_3$ has been used as an inert carrier for $LiNO_3$ since both substances do not result in measurable changes in

the waveguide.

Reverse-exchange is carried out by immersing the PE:$LiNbO_3$ sample in an eutectic melt of nitrate mixtures $LiNO_3$:KNO_3:$NaNO_3$ with a mole percent ratio of 37.5:44.5:18.0 (the melting point of this eutectic mixture is 120^0 C) at temperatures varying from 250^0 to 330^0 C.[21] After the reverse exchange, a buried waveguide with a graded index profile near the surface is created but with a reduced refractive index compared to the PE waveguide. Note that at the same time, a layer of pure $LiNbO_3$ is restored on the surface, and thus restoring the nonlinearity. Reverse-exchange can be applied to both PE and annealed waveguides. The latter is preferred since the additional annealing step allows better tailoring of the refractive index profile.

4.3 Characterisation of Proton Exchange and Annealing

Characterisation of the device used throughout this research work, presented in Section 4.4 and 4.5, revealed that its quality is still lower than that of the best state-of-the-art devices.[2] Therefore, improving the quality of the device would yield more sensitive results than the ones described in Chapter 6 and 7. Complete knowledge of the fabrication processes would allow one to tailor the waveguide properties at will, in order to produce highly efficient devices.[22] In my research work, much work was spent on characterising the diffusion process in the proton exchange and the subsequent annealing processes. Unfortunately, the characterisation of reverse proton exchange process were not completed, mainly due to the lack of time. The characterisation aimed to obtain the refractive index profile evolution of the waveguide during each process, as it is associated with the evolution of proton concentration in the substrate by either a linear or a nonlinear relationship. It was found[17,23,24] that there is essentially a linear relationship between these quantities, i.e.

$$\Delta n(x) \propto C(x), \tag{4.1}$$

where $\Delta n(x)$ is the refractive index profile of the waveguide, and $C(x)$ is the position dependent proton concentration. Since the refractive index profile evolution is based on the diffusion of the protons into the substrate, the characterisations was simpler if done on slab waveguides. Generalisation into channel waveguides can be readily done by assuming an isotropic diffusion.

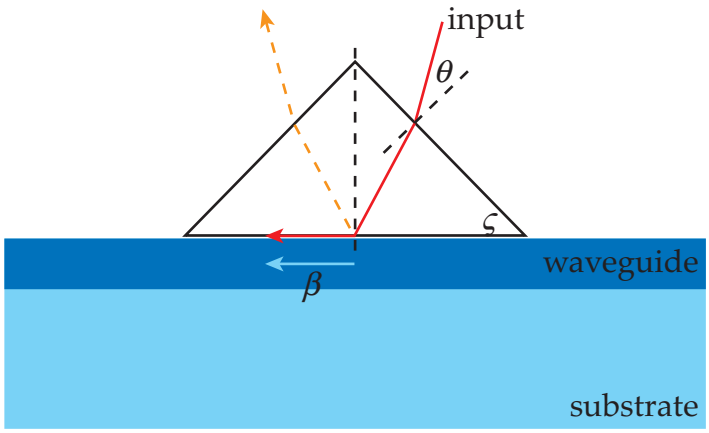

Figure 4.4: Illustration of prism coupling principle.

4.3.1 Prism Coupling

The main characterisation technique of the fabrication processes was the prism coupling technique,[25] done using a commercial instrument "Metricon". Figure 4.4 gives an illustration of the basic principle of prism coupling technique. A slab waveguide is put in contact with a prism whose refractive index is higher than the waveguide. When light is shone into the prism, it undergoes total internal reflection at the prism base, unless the waves in the prism and in the waveguide are coupled through their evanescent fields. This occurs when the propagation wavevector of the reflected light and the waveguide are equal. Changing the incident angle of the light allows a specific propagating mode to be preferentially excited in the waveguide. Therefore, placing a detector at the other side of the prism allows one to measure the angle θ at which this coupling occurs. The effective refractive index of propagating mode q of the waveguide is given by:

$$\mathcal{N}^{(q)} = n_p \sin\left[\varsigma + \arcsin\left(\frac{\sin\theta}{n_p}\right)\right], \tag{4.2}$$

where φ is the base-angle of the prism, θ is the incident angle of the beam with respect to the normal of the prism, and n_p is the refractive index of the prism. If the refractive index analytical profile is known, the indices can be used to calculate the parameters of the profile, as shown in Fig. 4.5. Otherwise, an inverse-Wentzel-Kramers-Brillouin (IWKB) method can be used to reconstruct the profile, as discussed later.

A rutile (TiO_2) prism with a base angle of 60^0 was used in the experiment. A Helium-Neon laser with a wavelength of 632.8 nm was used as the source. The extraordinary and ordinary refractive indices for rutile at this wavelength were $n_e = 2.865$ and

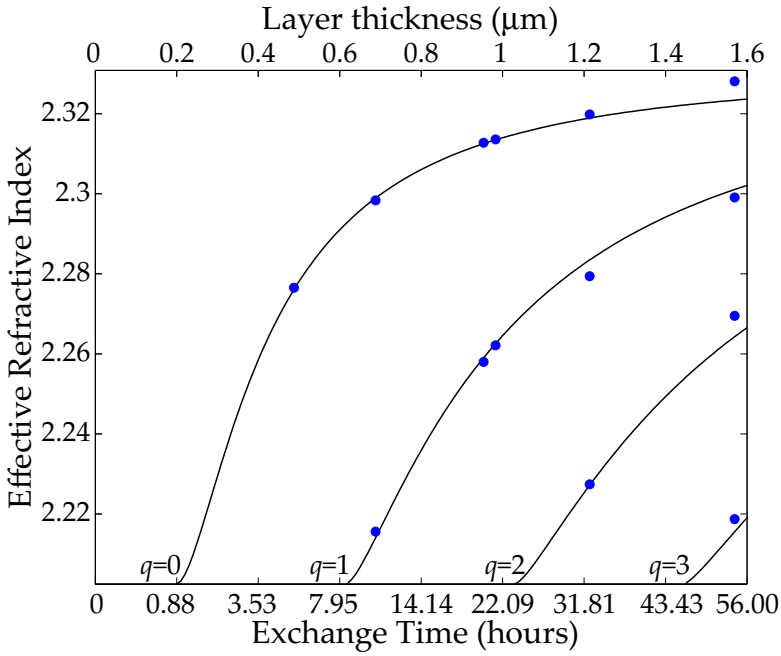

Figure 4.5: Measured effective refractive indices of proton-exchanged waveguides (blue dots) and theoretically fitted dispersion curves (solid lines) of a slab $LiNbO_3$ waveguide with a simple step index profile with a refractive index increase of $\Delta n_e = 0.128$. The exchange time is shown by the bottom abscissa, whilst the estimated proton exchanged layer thickness by the top abscissa.

$n_o = 2.584$, respectively. The prism and the waveguide were configured in such a way that the optic axis of the prism is perpendicular to the optic axis of the waveguide, so that the ordinary (extraordinary) refractive index of the prism was used for measuring the transverse magnetic (transverse electric) effective refractive indices.

4.3.2 Characterisation of Proton Exchange Process

The aim of the proton-exchange process characterisation was to determine the proton diffusion coefficient into the $LiNbO_3$ substrate. The resulting proton-rich layer has a step-like refractive index, whose thickness can be assumed to vary with time according to the standard diffusion law:[7]

$$d_e = 2\sqrt{D_e(T)t}, \tag{4.3}$$

where $D_e(T)$ is the diffusion coefficient, T is the absolute temperature of the diffusion, and t is the exchange time. Note that we expect the proton-exchanged depth d_e to depend on $\sqrt{(}t)$.

For the characterisations, several slab waveguides were prepared by exchanging

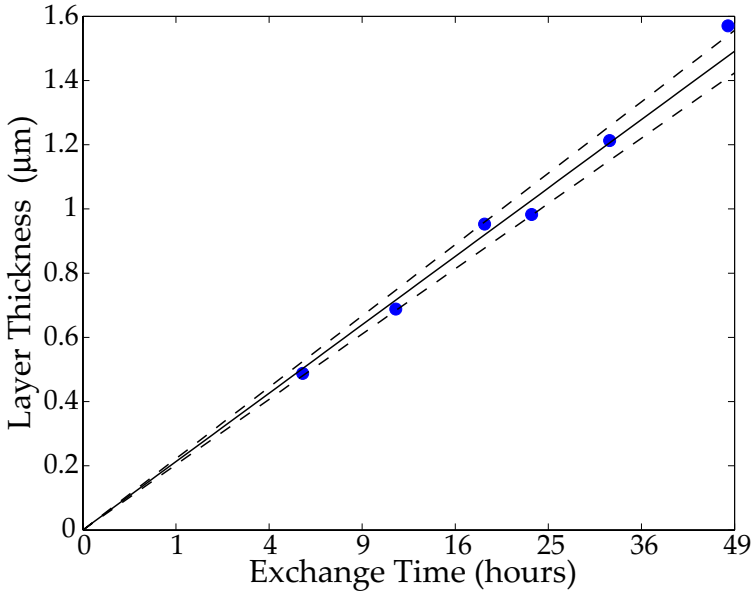

Figure 4.6: Estimated proton-exchanged waveguide thickness as a function of the exchange time (blue dots) in a squared-root scale, with its linear fit (solid line) and the uncertainty of the fit (dashed lines).

$LiNbO_3$ substrates at $160\,^0$C, for times ranging from 5 to 49 hours. Characterisations via the prism coupling technique (Subsection 4.3.1) revealed that the waveguides only support a polarisation that is parallel to the optic axis of the crystal, i.e. transverse magnetic polarisation. Figure 4.5 shows the measured effective refractive indices of the waveguides, as a function of the exchange time.

We made a theoretical model of the waveguide using a step refractive index profile, and found that a refractive index increase $\Delta n_e = 0.128$ gave the best fit to the measured effective refractive indices. Calculated effective refractive indices for the first four propagating modes ($q = 0, 1, 2, 3$) of a waveguide with a step index profile of $\Delta n_e = 0.128$ as a function of depth are also shown in Fig. 4.5. The excellent agreement confirms the reported results in literatures.[7,8,14] This allows us to estimate the thickness of the waveguide, which has a roughly linear relationship with the squared-root of the exchange time [Eq. (4.3)], as shown in Fig. 4.6. Assuming that the concentration of the proton source did not vary during the exchange, the diffusion coefficient $D_e(T_e) = (0.0113 \pm 0.0010)\,\mu\text{m}^2/\text{hour}$ can be deduced from the linear fit gradient.

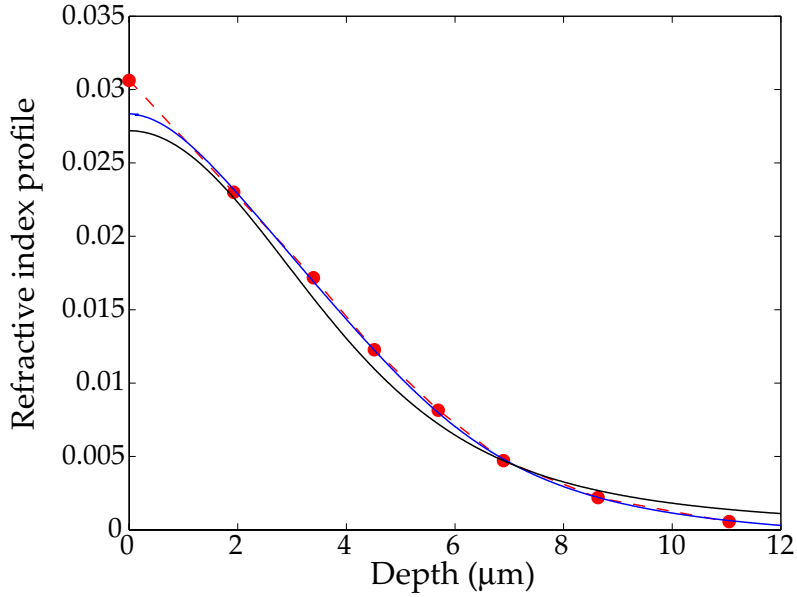

Figure 4.7: Reconstructed refractive index using IWKB method with piecewise-linear (red dots) and continuous (blue curves) functions. Calculated refractive index profile from the nonlinear diffusion equation (black curves), as described in the text, is also shown.

4.3.3 Kinetics of Annealing Process

The characterisation of the annealing process aims to understand the kinetics of the proton diffusion, which defines the refractive index profile. Tailoring this refractive index profile should enable one to produce efficient waveguides. Two PE waveguides of thickness 0.69 and 0.95 μm were annealed at 330 ^{0}C with an O_2 flow of 200 cm^3/min for times ranging from 1 to 200 hours. In order to avoid thermal shocks, the temperature was increased at a rate of 10 ^{0}C/min before the annealing, and decreased slowly to room temperature afterward.

After each annealing step, the refractive index profiles were reconstructed using the IWKB method from the effective refractive indices obtained via prism coupling (Subsection 4.3.1) in order to gather the information of the refractive index at the surface $[\Delta n_a(0)]$ and the $1/e$ depth (d_a). The reconstruction used either piecewise-linear[26,27] or continuous[28] functions. I wrote a computer program to perform this reconstruction, and the reconstructed profiles for a sample with an initial proton-rich layer thickness of 0.95 μm after being a 57 hours annealing are shown in Fig. 4.7. As can be seen in the picture, the piecewise-linear and continuous functions differ only slightly near the surface of the waveguide. Hence, we took the average of both for the value of surface

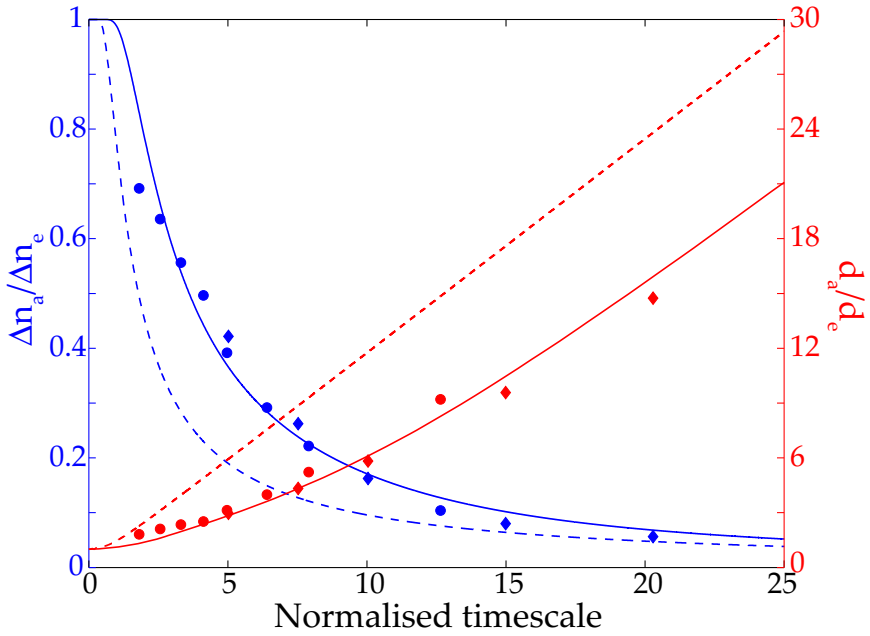

Figure 4.8: Normalised refractive index increase $\Delta n_e/\Delta n_a$ (blue colours, left ordinates) and normalised depth d_a/d_e (red colours, right ordinates) as a function of the squared-root of normalised time $\sqrt{(t'_a)}$. Markers are data from the reconstructed profile using IWKB, where the circles are associated with $d_e = 0.69\,\mu$m, whilst diamonds are associated with $d_e = 0.95\,\mu$m. Linear (dashed lines) and nonlinear (solid lines) diffusion results are also shown.

refractive index $[\Delta n_a(0)]$.

Analysis of the diffusion kinetics during annealing was done using the idea of a similarity transformation.[17,29] The surface index $[\Delta n_a(0)]$ and the $1/e$ depth (d_a) of the annealed waveguides were normalised to the PE waveguides values (Δn_e and d_e, respectively), whilst the annealing time t_a was normalised to $t'_a = t_a/d_e^2$. Figure 4.8 shows the normalised surface index and normalised depth obtained from our annealed waveguides with different initial PE layer thicknesses. The fact that the normalised depth (d_a/d_e) and normalised surface refractive index $(\Delta n_a(0)/\Delta n_e)$ for waveguides with different initial proton rich layer thicknesses (d_e) in Figure 4.8 follow the same trend against normalised time t'_a implies that the evolution of the refractive index profile only depends on normalised time t'_a for a given annealing temperature T_a. Although this analysis does not make any assumptions on the physical processes that take place during the fabrication, the fact that the data points follow the same trend shows that the evolution of the refractive index profile can be modelled by a differential equation obeying the similarity transformation described above, such as the diffusion equation.

The general diffusion equation used to modelled the evolution of proton concentration is given by:

$$\frac{\partial C'(\mathbf{r}'_a, t'_a)}{\partial t'_a} = \nabla \cdot \left[D(C') \nabla C'(\mathbf{r}'_a, t'_a) \right], \tag{4.4}$$

where $C'(\mathbf{r}'_a, t'_a)$ is the normalised proton concentration, $\mathbf{r}'_a$ is the normalised coordinate, t'_a is the normalised timescale, and $D(C')$ is the nonlinear diffusion coefficient. When $D(C')$ is constant, the above equation reduces to a standard linear diffusion equation. The above diffusion equation was solved using a *linearised three-level implicit finite difference scheme*.[30]

The normalised depth data in Fig. 4.8 suggest that the diffusion kinetics is asymptotically linear when the timescale is sufficiently large. A linear diffusion coefficient $D_0 = 0.344\,\mu\text{m}^2/\text{hour}$ can therefore be determined from the slope of the curve as the annealing time becomes large. Solving Eq. (4.4) using this linear diffusion coefficient results in the dashed line in Fig. 4.8. However, it can easily be seen that the linear diffusion results do not match the experimental data. Instead, we use the following expression for the nonlinear diffusion coefficient:[17]

$$D(C') = D_0[a + (1-a)\exp(-bC')], \tag{4.5}$$

where a and b are free parameters, whilst D_0 is the linear diffusion coefficient. We found that the parameters $a = 0.23$ and $b = 20$ yielded a good fit to the data, as shown in Fig. 4.8. A calculated refractive index profile is plotted in Fig. 4.7 for comparison with the IWKB reconstructions, showing a good agreement. Unfortunately, optimisation of the refractive index profile for buried channel waveguides cannot be done without knowledge of the reverse exchange process, which was not completed due to the lack of time.

4.4 Linear Properties of the Device

The linear properties of the device are a result of the buried waveguide structure, and of particular interest are their transverse field profiles and propagation losses. Preferentially exciting the fundamental mode of a waveguide that support several modes is well-known to be difficult. Therefore, to be of practical use, it is essential that the waveguides support one and only one propagating mode at the desired fundamental frequency. Furthermore, the ease of integration with other optical components, such as standard single-mode fibre (SMF) in telecommunications systems, is determined by

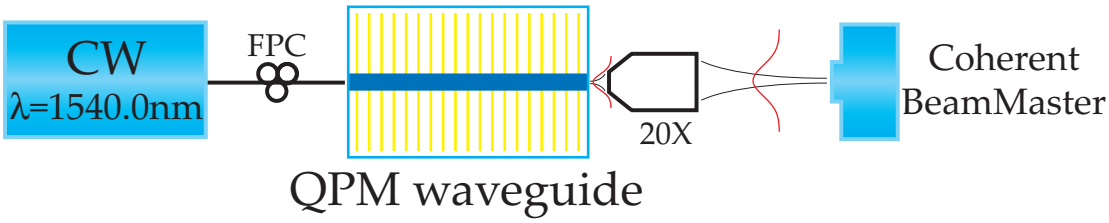

Figure 4.9: Schematic illustration of experimental setup for measuring transverse field profile of a waveguide.

their transverse field profile matching. In addition, in order to achieve high nonlinear performance, tight optical confinements and low propagation losses ($< 1\,\mathrm{dB/cm}$) in the device are required. The lowest propagation loss coefficient reported to date for a buried channel waveguide fabricated using the same method as ours is $0.3\,\mathrm{dB/cm}$.[2] Therefore, characterisation of these properties is necessary, especially since we have limited knowledge of the fabrication processes to predict them. Moreover, this knowledge will help the improvement of the device in the future.

4.4.1 Waveguide Transverse Field Profiles

The waveguide transverse field profile $|\mathbf{F}(x,y)|^2$ [see Eq. (3.22)] can be easily measured by imaging the near-field of the waveguide onto a commercial instrument ("Coherent BeamMaster") that employs a scanning knife-edge technique.[31,32] Figure 4.9 shows a schematic illustration of the experimental setup used to measure the transverse mode profile of the waveguides in our device. A CW laser at 1540 nm was coupled into the waveguide via a standard single-mode fibre. Since our waveguide only supports TM polarised modes, a fibre polarisation controller (FPC) was necessary to maximise the amount of power coupled into the waveguide. The near-field of the waveguide was then imaged onto the "Coherent BeamMaster" using a 20× microscope objective. A further calibration step was necessary to accurately determine the size of the transverse field profile. This was achieved by replacing the waveguide in the setup with another object of known size, such as another waveguide, a fibre, or transmission gratings. As a representative sample, Figure 4.10(a) shows a measured transverse field profile contour plot of a waveguide of nominal width $6\,\mu\mathrm{m}$ measured at a wavelength of 1540.0 nm. For a comparison, the transverse field profile image recorded by an infrared camera is shown in Fig. 4.10(b).

Figure 4.11 shows the $1/e^2$ width of the horizontal and the vertical slices of the

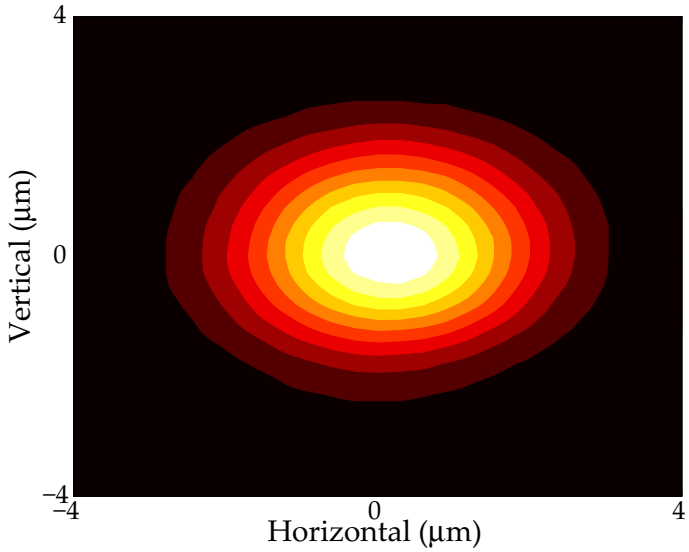

(a)

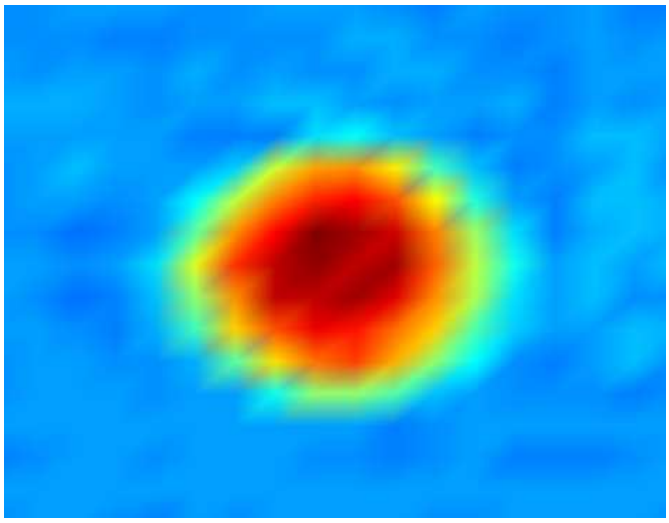

(b)

Figure 4.10: Measured transverse field profile of a waveguide with a nominal width 6 μm at a wavelength of 1540.0 nm. a) Linear contour plot of the measurement from the "Coherent BeamMaster." The contour plot was normalised to unity with an equidistant spacing of 0.1. b) Image from an infrared camera with arbitrary scales.

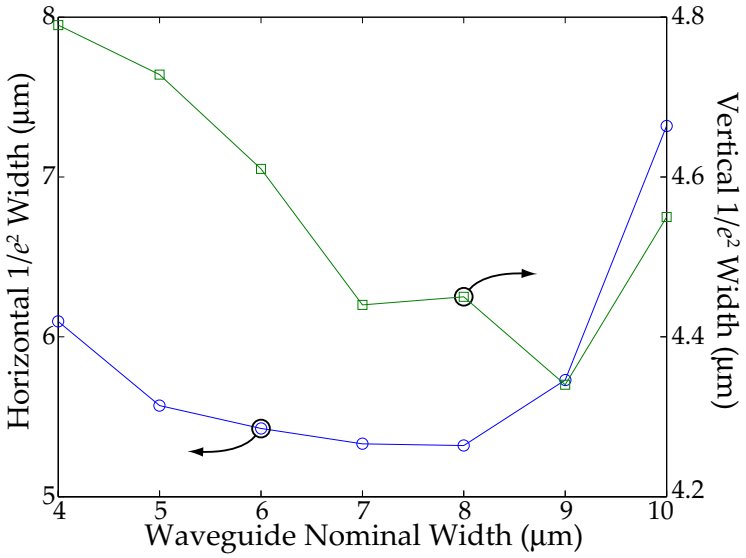

Figure 4.11: Horizontal (blue) and vertical (green) transverse field profile $1/e^2$ width as a function of the waveguide nominal width measured at a wavelength of 1540.0 nm.

measured transverse field profile as a function of the waveguide nominal widths. It can be observed that the vertical slice widths do not vary as much as the horizontal slice widths. This can be understood since the vertical dimensions are mainly determined by the diffusion process during their fabrication, but the horizontal ones depend strongly on the waveguide nominal widths. If the waveguide dimension is too small, it will not be able to support a propagating mode. This condition is called the cut-off point. When the waveguide dimension increases, it will be able to support a propagating mode with loose optical confinement, resulting in a relatively large transverse mode profile size. As the waveguide dimension continues to increase, the optical confinement improves, and thus the transverse field profile size decreases. This continues until it reaches a minimum and then increases monotonically, as the waveguide dimension dominates the transverse field profile size. In addition, at some point the waveguide will also be able to support more propagating modes (multi-mode). We can see a clear minimum in Fig. 4.11 for the waveguide nominal width of 8 μm. We also note that the waveguides becomes multi-mode at nominal width larger than 7 μm.

Knowing the transverse field profile dimension, we can calculate its coupling efficiency to a standard SMF, due to the overlap between the two different transverse field profiles. The coupling efficiency (in dB) is given by:

$$\eta_c = -10 \log S_{ovl}, \tag{4.6}$$

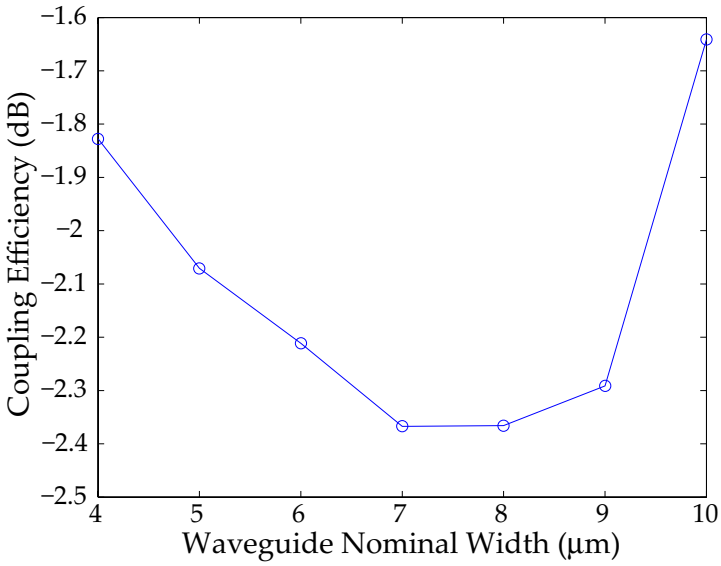

Figure 4.12: Calculated coupling efficiency [Eq. (4.6)] between the waveguide and a standard single-mode fibre as a function of the waveguide nominal width.

where the area overlap is defined as:

$$S_{\text{ovl}} = \frac{\int |\mathbf{F}_{\text{SMF}}|^2 \, dxdy \int |\mathbf{F}_{\text{WG}}|^2 \, dxdy}{\left(\int |\mathbf{F}_{\text{SMF}}| \, |\mathbf{F}_{\text{WG}}| \, dxdy\right)^2}, \tag{4.7}$$

with $\mathbf{F}_{\text{SMF}}$ and $\mathbf{F}_{\text{WG}}$ being the transverse field profiles for the standard SMF and waveguide, respectively. Figure 4.12 shows the calculated coupling efficiency η_c as a function of the waveguide nominal widths. Since the $1/e^2$ transverse field diameter of a standard SMF that we used was $10.5\,\mu$m, waveguides with large transverse mode profile areas have the best coupling efficiencies, explaining the shape of the curve in Fig. 4.12. This work shows that waveguides with a nominal width of $6\,\mu$m is our preferred choice, since they support only a single propagating mode with the tightest optical confinement.

4.4.2 Propagation Losses

We characterised the propagation loss of the waveguide using the Fabry-Perot (FP) resonator method, following the work of Regener and Sohler.[33] This method is non-destructive, and does not require the fabrication of additional structures, such as ring resonators, on the substrate. A FP resonator consists of a pair of parallel reflective surfaces, separated by a length L. A waveguide (see Fig. 4.1) naturally forms a FP resonator, with the polished end-faces as the pair of reflective surfaces, having a reflectivity $R = \left(\frac{\mathcal{N}-1}{\mathcal{N}+1}\right)^2$, where $\mathcal{N}$ is the effective refractive index of a propagating mode. Since

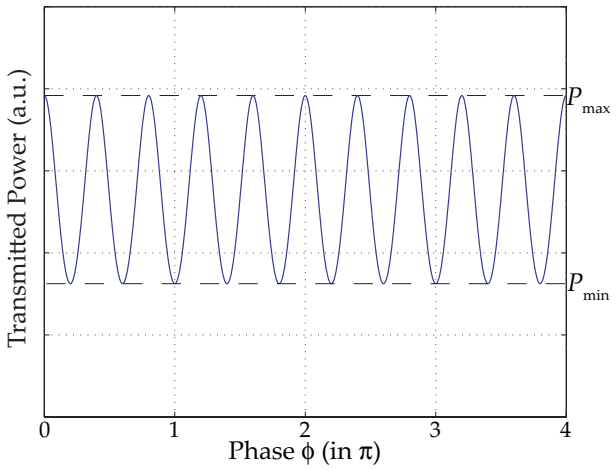

Figure 4.13: Theoretical Fabry-Perot fringes as a function of the phase $\phi = 2\beta L$.

different propagating modes have different propagation losses and effective refractive indices, the analysis of waveguides that support a single propagating mode is the simplest, and thus is much preferred. When the internal phase $\phi = 2\beta L$ of a FP resonator is varied, resonances of the transmitted power, such as those shown in Fig. 4.13 can be observed. The FP fringes are analytically given by:[33]

$$\mathcal{P}_t(\phi) = \frac{T^2 \exp(-\alpha L)}{[1 - R\exp(-\alpha L)]^2 + 4R\exp(-\alpha L)\sin^2\left(\frac{\phi}{2}\right)} \mathcal{P}_0 \eta_c, \tag{4.8}$$

where $T = 1 - R$ is the transmissivity of the end-faces, $\mathcal{P}_0$ is the input power to the waveguide, η_c is the coupling efficiency [Eq. (4.6)], and α is the propagation loss coefficient of the waveguide. By measuring the contrast of the resonance curve, which is defined as:

$$K = \frac{\mathcal{P}_{max} - \mathcal{P}_{min}}{\mathcal{P}_{max} + \mathcal{P}_{min}}, \tag{4.9}$$

the propagation loss coefficient in the resonator, or more specifically, the waveguide, in dB/length unit, can be deduced by straightforward algebra from Eq. (4.8):

$$\alpha = \frac{4.34}{L} \ln\left[\frac{RK}{1 - \sqrt{1 - K^2}}\right]. \tag{4.10}$$

Importantly, it can be seen from the above formula that the propagation loss coefficient is independent of the coupling efficiency η_c, provided η_c does not depend on ϕ.

Variation of the FP resonator internal phase $\phi = 2\beta L$ in the waveguide was commonly achieved by heating the sample, causing changes in the optical path $\mathcal{N}L$ in the waveguide.[33,34] We attempted to adopt this method and met with difficulties, mainly

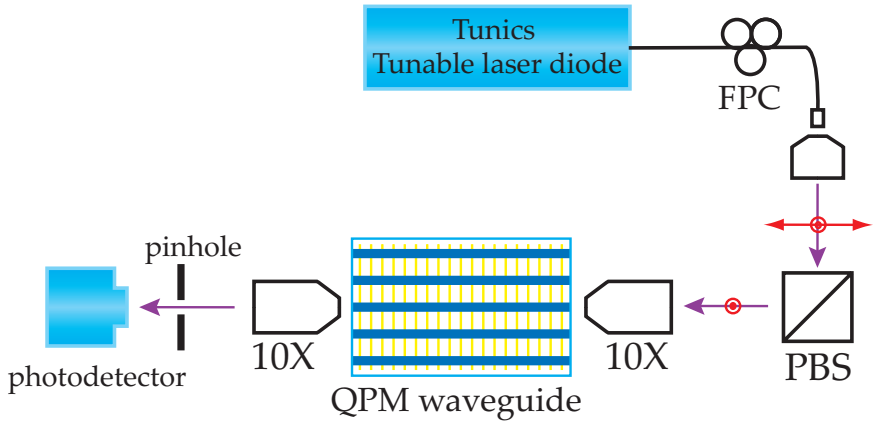

Figure 4.14: Schematic illustration of the experimental setup used in the characterisation of the waveguide propagation loss via a FP resonator method.

because the thermal expansion affects the coupling efficiency, which needs to be constant during the measurement. Hence this approach is not very reliable, and we chose to vary the wavelength of the source instead. Figure 4.14 shows a schematic illustration of the experimental setup used for the propagation loss measurement via a FP resonator method. A tunable external cavity source, "NetTest Tunics-Plus," was used as the source in this experiment. It had a stable longitudinal mode with a linewidth of 2 fm, corresponding to a coherence length of 1.5 km, much longer than the waveguide length. The light from the source was out-coupled in free-space via a microscope objective, and injected into the waveguide via a 10× microscope objective. The appropriate polarisation was selected by a polarising beam-splitter (PBS), and thus a fibre polarisation controller (FPC) was necessary prior to out-coupling. The light at the device output was focused onto a photodetector by a 10× microscope objective. Spatial filtering by a pinhole was employed to suppress background noise. In addition, we employed a different experimental setup employing fibre butt-coupling at the waveguide input/output, and found similar results to this setup.

Figure 4.15 shows measured FP resonances of a waveguide of nominal width 6 μm. The period of the resonances is 0.023 nm, in agreement with the theoretically predicted one. The contrast was evaluated to be $K = 0.123$, leading to a propagation loss coefficient $\alpha = 1.3\,\mathrm{dB/cm}$. We assumed that the effective refractive index of the waveguide was $\mathcal{N} \approx n_e + \Delta n_e/2 = 2.149$ at $\sim 1550\,\mathrm{nm}$, resulting in a reflectivity $R = 13.32\,\%$. The actual reflectivity may be less than this value, because of imperfections of the end-face polishing quality and/or inclinations of the end-faces from the normal. Therefore, the

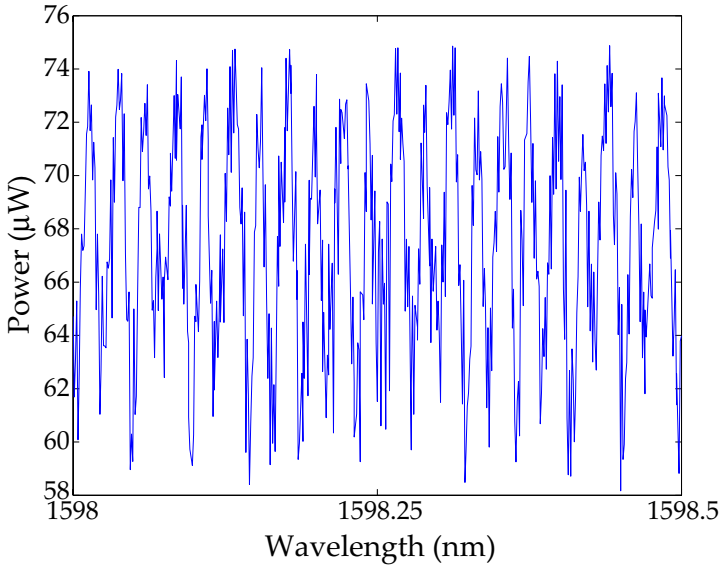

Figure 4.15: Measured FP resonances of a waveguide of nominal width 6 μm.

measured value above is the upper limit of the actual propagation loss. We note that the end-faces inclinations of our waveguide were less than 0.1^0, such that the reduction of the propagation loss coefficient should be less than 0.05 dB/cm. We performed numerous propagation loss measurements on this waveguide, and found that the propagation loss coefficient estimate varied between ~ 0.8 and ~ 1.8 dB/cm.

We also performed additional characterisation of the propagation loss coefficient by measuring the fibre-waveguide-fibre throughput. Losses in such system are due to the reflection at the waveguide-air and fibre-air interfaces, the waveguide-fibre mode-mismatch, and the propagation loss. Since the first two factors can be calculated theoretically from the Fresnel formula and Eq. (4.6), respectively, we can readily estimate the last. Proper and meticulous alignment of the fibre to the waveguide using a nanopositioning system should readily yield a coupling efficiency that is closed to the theoretical calculation. Compiling numerous data from the FP resonator method described above and from this method, we finally estimated that the actual propagation loss coefficient to be $\alpha \approx 1$ dB/cm.

4.5 Nonlinear Properties of the Device

Having characterised the linear properties of the device, we then characterised the nonlinear ones. Nonlinear properties of the device are associated with the properties of

second-order nonlinear interactions. The two main pieces of information, that we are interested in, are the working regime in terms of wavelength and the performance of the device. The working regime is determined by the phase-matching wavelengths for the SHG and SFG interactions, whilst the performance is measured by the normalised conversion efficiency η_{nor} [Eq. (3.18)].

4.5.1 Second-Harmonic Generation

Second-harmonic generation (SHG) is the simplest second-order nonlinear interaction, and thus the most convenient way to perform a nonlinear characterisation. As previously reviewed in Chapter 3, SHG involves the upconversion of an input FF wave at ω_{FF} to its SH frequency at $\omega_{\text{SH}} = 2\omega_{\text{FF}}$. By tuning the frequency of the FF wave, the phase-mismatch between the FF and the SH waves is varied. This results in the generation of a SHG tuning curve (see Fig. 3.8), which shows the quality of the device (see section 3.5). The normalised conversion efficiency can be obtained from the peak of the curve, the effective interaction length can be deduced from the bandwidth at full-width-half-maximum (FWHM), the dispersion of the waveguide is given by the phase-matching wavelength, whilst the uniformity of the device is reflected in the shape of the curve.

Figure 4.16 shows a schematic illustration of the experimental setup used in this nonlinear characterisation via SHG. The source for generating the tunable FF wave for our SHG experiment was an all-fibre amplified tunable diode laser. A CW tunable diode laser "HP 8168C" operating at a constant power of 1.5 mW was externally modulated by an electro-optics modulator (EOM), and then amplified by an erbium-doped fibre amplifier (EDFA). The source produced a train of 200 ns pulses with a repetition rate of 100 kHz, and an average (peak) power of ~ 68 mW (~ 2 W). The source was tunable from 1528 to 1565 nm in steps of 0.02 nm. This tunability is within the C-band, the region of interest of this research work. Since the pulses are extremely long, i.e. much longer than the waveguide, we can consider them as CW during the experiment, enabling the use of analysis presented in Chapter 3.

Next, the FF pulse train was out-coupled into free-space using a microscope objective, and the appropriate input polarisation was selected by a polarising beam-splitter (PBS). A fibre polarisation controller (FPC) was necessary prior to the out-coupling to maximise the appropriate polarisation component. Afterward, the FF pulse train

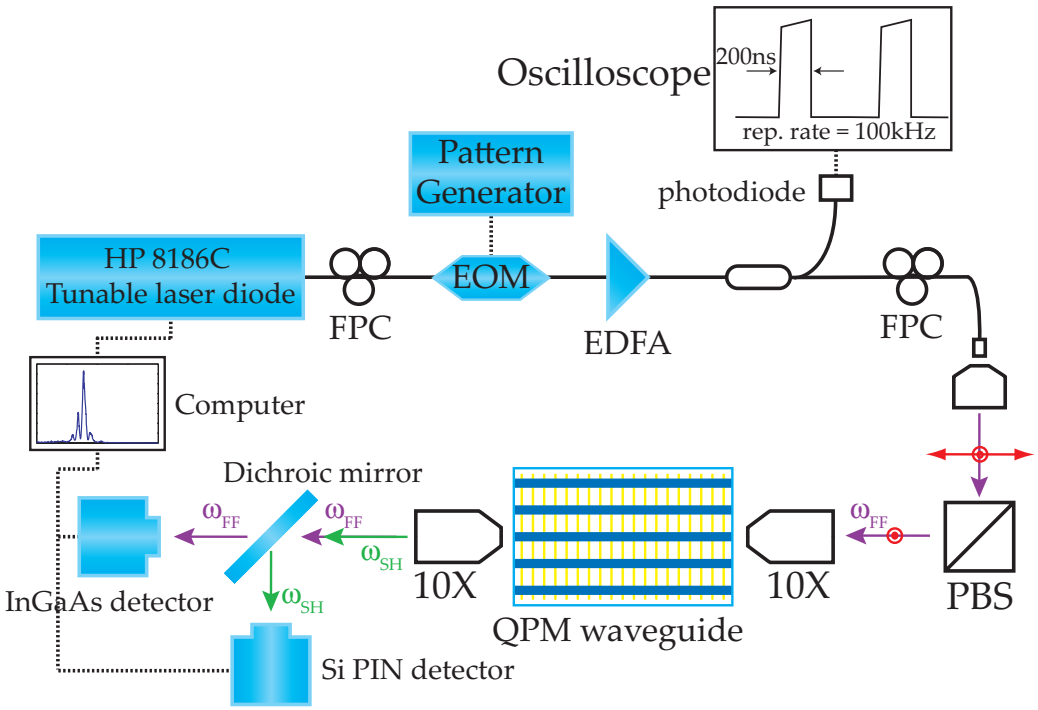

Figure 4.16: Schematic illustration of the experimental setup for the nonlinear characterisation via SHG.

was injected into the waveguide using a 10× microscope objective. The FF and the SH waves at the waveguide output were collected by another 10× microscope objective, before being separated by a dichroic mirror and measured by InGaAs and Si PIN detectors, respectively. The tunable source and the detectors were computer controlled to perform the wavelength scan and the data acquisition.

It is well-known that $LiNbO_3$ is sensitive to photorefractive effects at room temperature, where charge migration (by photovoltaic effect) followed by electro-optic effect induce refractive index changes.[35] Photorefractive effects shift the phase-matching wavelength, degrade the conversion efficiency by altering the phase-matching condition, and cause instabilities due to variation of effective index value. The effects can be severe at visible wavelengths and are enhanced in waveguide devices due to the high optical intensity. Photorefractive effects can be significantly reduced by heating the devices. In our experiment, the sample was heated by placing it in a copper block connected to a thin resistor operated at a constant electrical current. According to our measurements, the time required for the temperature to shift by $0.5\,^0$C was much longer than the time required to complete the wavelength scan. Hence, we may consider the temperature

was constant in each characterisation.

From all of the QPM structures and waveguides in our device, we are interested in the ones that had a QPM period of $\Lambda = 15\,\mu$m and a waveguide nominal width of $w = 6\,\mu$m. We found that such devices supported single propagating mode and had a phase-matching wavelength in the region of interest. There were three such waveguides on the sample, but one was accidentally damaged and thus could not be used. Second-harmonic generation tuning curves for the remaining two, measured at a temperature of $\sim 94\,^0$C, are shown in Fig. 4.17. The phase-matching wavelength of both PPLN waveguides, as observed from Fig. 3.2, was 1537.7 nm. Note that these tuning curves should be identical. The bandwidth [Eq. (3.20)] of Figs. 4.17(a) and 4.17(b) were 0.56 and 0.75 nm, respectively. The theoretical bandwidth of a 2.6 cm long bulk PPLN, as calculated using the Sellmeier equation,[36] was $\Delta\lambda = 0.42$ nm, from which we can deduce the effective interaction lengths for Figs. 4.17(a) and 4.17(b) to be 1.9 and 1.5 cm, respectively. The discrepancy between calculated and measured bandwidths implies that the whole length of the device is not efficiently used in the interaction due to the nonuniformities in the device, which can be further verified from the distorted shape of the SHG tuning curves. Although the latter device whose SHG tuning curve is depicted in Fig. 4.17(a) had a shorter effective interaction length than the one depicted in Fig. 4.17(b), the fact that Fig. 4.17(b) is more distorted than Fig. 4.17(a) makes us to prefer working with the latter.

In addition, we can infer from this characterisation, that the device had a higher dispersion than bulk PPLN, because of the waveguide dispersion. For bulk PPLN, the theoretical gratings period for phase-matching the same wavelength at the same condition (1537.7 nm at $\sim 94^0$ C) is 18.4 μm, which is longer than the gratings period used in the experiment. This fact implies that the wave vector mismatch $\Delta\beta = \beta_2 - 2\beta_1$ of our device is greater than the bulk PPLN, and thus a larger reciprocal lattice vector K, or equivalently, a shorter QPM period, is needed.

4.5.2 Normalised Efficiency Measurement

The figure-of-merit of the device is determined by the normalised conversion efficiency $\eta_{\rm nor}$ [Eq. (3.18)], which can be measured when the phase-matching condition occurs ($\Delta\beta_{\rm QPM} = 0$). In a device of negligible losses, the normalised conversion efficiency can be determined from the peak of the nonlinear conversion efficiency [Eq. (3.17)].

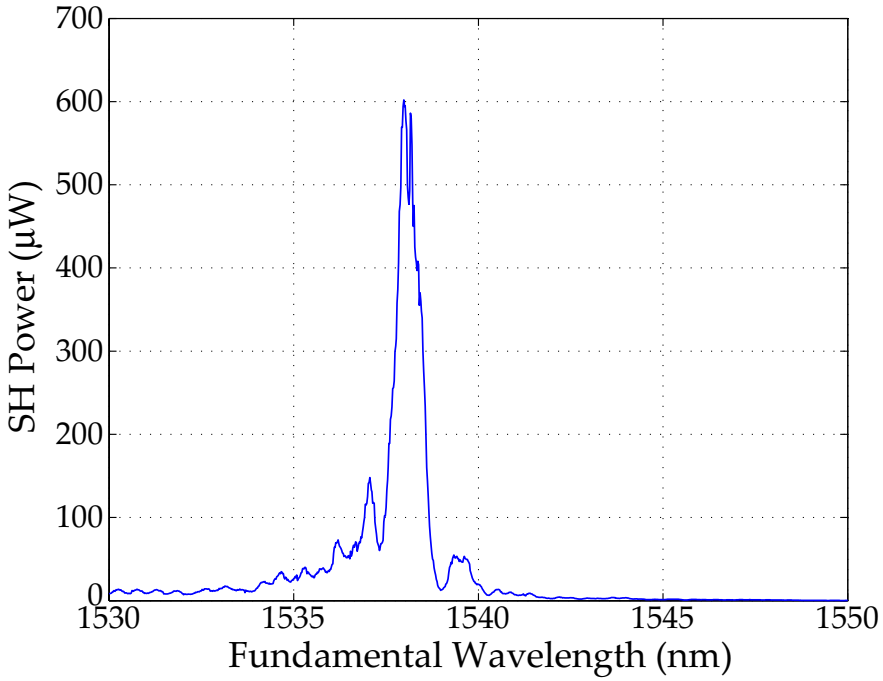

(a)

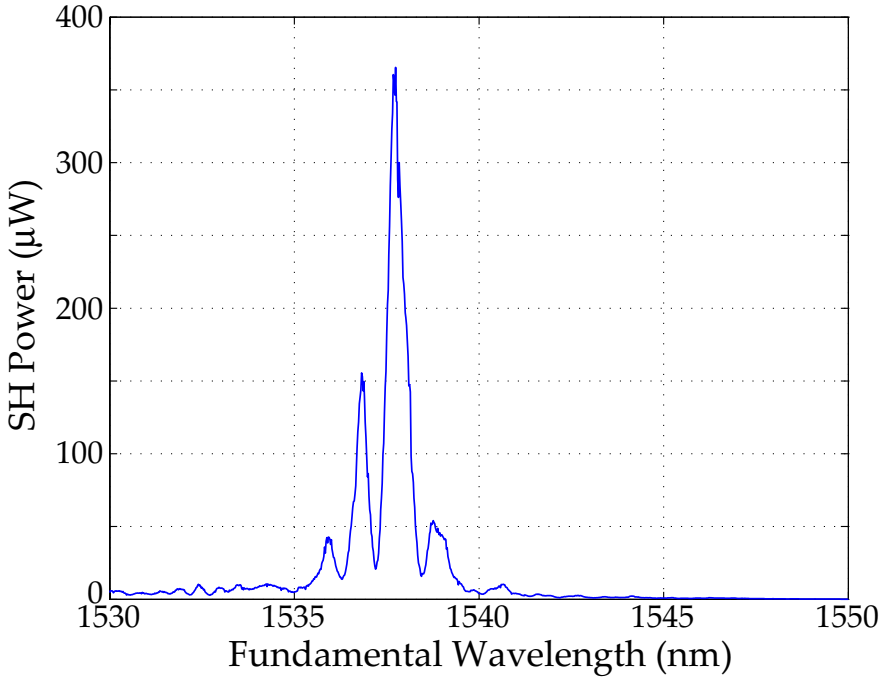

(b)

Figure 4.17: Measured SHG tuning curves of two waveguides in our device at a temperature of $\sim 94\,^0$C. The two waveguides had a QPM period of $\Lambda = 15\,\mu$m and a waveguide of nominal width of $w = 6\,\mu$m.

However, in real devices, losses cannot be neglected, and thus the nonlinear conversion efficiency becomes more complicated:[2]

$$\eta_{\text{lossy}} = \eta_{\text{nor}} \frac{\exp\left(-4\alpha_{\text{FF}}L\right) + \exp\left(-4\alpha_{\text{SH}}L\right) - 2\cos(\Delta\beta L)\exp\left(-4[\alpha_{\text{SH}} + 2\alpha_{\text{FF}}]L\right)}{\left(\alpha_{\text{SH}} - \alpha_{\text{FF}}\right)^2 + \Delta\beta^2}, \tag{4.11}$$

where α_{FF} and α_{SH} are the propagation losses of the waveguides at ω_{FF} and ω_{SH}, respectively. Since it is often easier to measure the FF and the SH powers at the device output, we define a measured conversion efficiency as

$$\eta_{\text{meas}} = \frac{P_{\text{SH}}(L)}{P_{\text{FF}}^2(L)}, \tag{4.12}$$

which can be expanded into

$$\eta_{\text{meas}} = \eta_{\text{nor}} \frac{\exp\left(-4\alpha_{\text{FF}}L\right) + \exp\left(-4\alpha_{\text{SH}}L\right) - 2\cos(\Delta\beta L)\exp\left(-4[\alpha_{\text{SH}} + 2\alpha_{\text{FF}}]L\right)}{\exp\left(-4\alpha_{\text{FF}}L\right)\left[\left(\alpha_{\text{SH}} - \alpha_{\text{FF}}\right)^2 + \Delta\beta^2\right]}. \tag{4.13}$$

In the special case of $\alpha_{\text{SH}} = 2\alpha_{\text{FF}}$, which is often true in many real devices, including waveguides on Lithium Niobates,[2] the above expression reduces nicely to

$$\eta_{\text{meas}} = \eta_{\text{nor}} L^2 \,\text{sinc}^2\left[\Delta\beta\frac{L}{2}\right]. \tag{4.14}$$

The above expression is the same as the nonlinear conversion efficiency in the lossless case η_{NL} [Eq. (3.17)].

The simplest way to measure of η_{nor} is when the phase-matching condition occurs ($\Delta\beta = 0$), such that the measured nonlinear conversion efficiency becomes:

$$\eta_{\text{meas}} = \frac{P_{\text{SH}}(L)}{P_{\text{FF}}^2(L)} = \eta_{\text{nor}} L^2. \tag{4.15}$$

By measuring the SH power as a function of the FF power, at the phase-matching wavelength, the above measured nonlinear conversion efficiency value η_{meas} can be obtained, from which η_{nor} can be easily deduced.

The experimental setup for the SHG characterisation (Fig. 4.16) was used to measure the normalised conversion efficiency. The tunable laser diode was operated at the phase-matching wavelength of 1537.7 nm at a sample temperature of $\sim 94\,^0$C. An optical band-pass filter with a 0.5 nm spectral FWHM was placed after the EDFA to suppress the amplified spontaneous emission (ASE). Figure 4.18 shows the SH power as a function of the FF power, which was varied by changing the EDFA gain, after correcting for the transmittance of the microscope objective and the waveguide-air interface. A quadratic

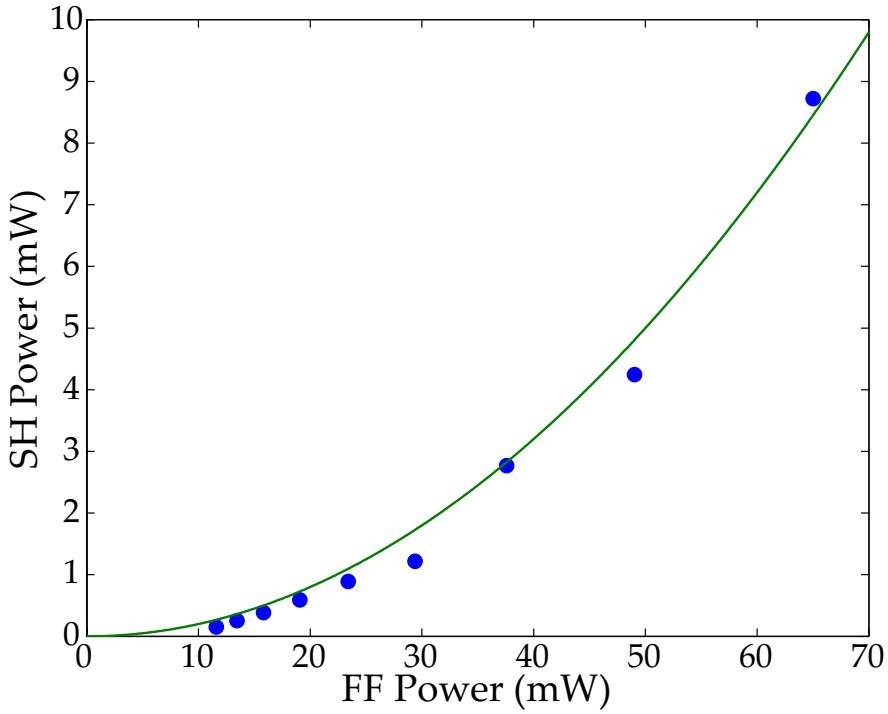

Figure 4.18: SH power $[P_{\mathrm{SH}}(L)]$ as a function of the output FF power $[P_{\mathrm{FF}}(L)]$ (blue filled circles), with its quadratic fit (green line)

fit to the experimental data results in a normalised conversion efficiency of $\eta_{\mathrm{nor}} = (30 \pm 2)\,\%[\mathrm{W\,cm^2}]^{-1}$, if the whole length of the device $L = 2.6\,\mathrm{cm}$ was used in the calculation, or $\eta_{\mathrm{nor}} = (91 \pm 2)\,\%[\mathrm{W\,cm^2}]^{-1}$, if the effective interaction length of the device $L_{\mathrm{eff}} = 1.5\,\mathrm{cm}$ was used. Since the measured normalised conversion efficiency of our device is still less than the highest reported so far,[2] $\eta_{\mathrm{nor}} = 150\,\%[\mathrm{W\,cm^2}]^{-1}$, improvements can be expected for future devices.

4.5.3 Sum-Frequency Generation

For many applications, such as the characterisation of ultrashort optical pulses using the frequency-resolved optical gating (FROG) technique (see Chapter 6), more general three-wave mixing processes are often employed rather than SHG. We therefore also performed nonlinear characterisations via a non-degenerate three-wave mixing process, specifically, via a sum-frequency generation (SFG). Sum-frequency generation involves the mixing of two electromagnetic waves, a pump at ω_{P} and a signal at ω_{S} in a $\chi^{(2)}$ device to produce a sum-frequency wave at $\omega_{\mathrm{SF}} = \omega_{\mathrm{P}} + \omega_{\mathrm{S}}$. Of course, SFG is a more general case to SHG, whose input waves are at the degenerate frequency $\omega_{\mathrm{FF}} = \omega_{\mathrm{P}} =$

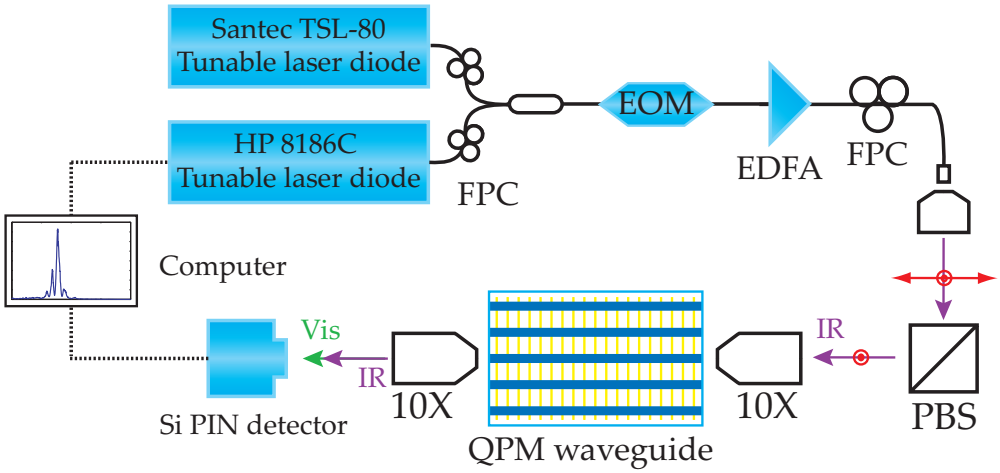

Figure 4.19: Schematic illustration of the experimental setup for the nonlinear characterisation via SFG.

ω_S. Nonlinear characterisation via SFG can be achieved by generating a tuning curve similar to that of SHG, by varying the input signal frequency. The nonlinear conversion efficiency, similar to that of SHG [Eq. (3.17)], is given by:

$$\eta_{NL} = \frac{\mathcal{P}_{SF}(L)}{\mathcal{P}_S(0)\mathcal{P}_P(0)} = 4\eta_{nor}L^2\,\mathrm{sinc}^2\left[\Delta\beta\frac{L}{2}\right], \tag{4.16}$$

where the SFG wavevector mismatch is defined as:

$$\Delta\beta = \beta(\omega_{SF}) - \beta(\omega_P) - \beta(\omega_S) - K. \tag{4.17}$$

Figure 4.19 shows a schematic of the experimental setup used in this nonlinear characterisation via SFG. Two CW tunable laser diode, "HP 8168C" and "Santec TSL-80", which acted as signal and pump, respectively, were combined together via a 50:50 coupler, before being carved by an EOM and amplified by an EDFA. The experimental setup afterward followed the one used in previous characterisation via SHG (Fig. 4.16). The light at the device output was finally collected by a Si PIN detector. Characterisation via SFG was performed by selecting a specific pump wavelength, and then scanning the signal wavelength to find the phase-matching condition. An example of a characterisation performed at a temperature of $\sim 105\,^0$C with a fixed pump wavelength of 1531.6 nm, is shown in Fig. 4.20. As the signal wavelength was scanned from 1535 nm, a peak which corresponds to the SHG phase-matching wavelength at 1539 nm was encountered, before the second peak which corresponds to the SFG phase-matching wavelength pair at 1546.5 nm was found. The SFG peak had a FWHM of 1.5 nm, twice of the SHG

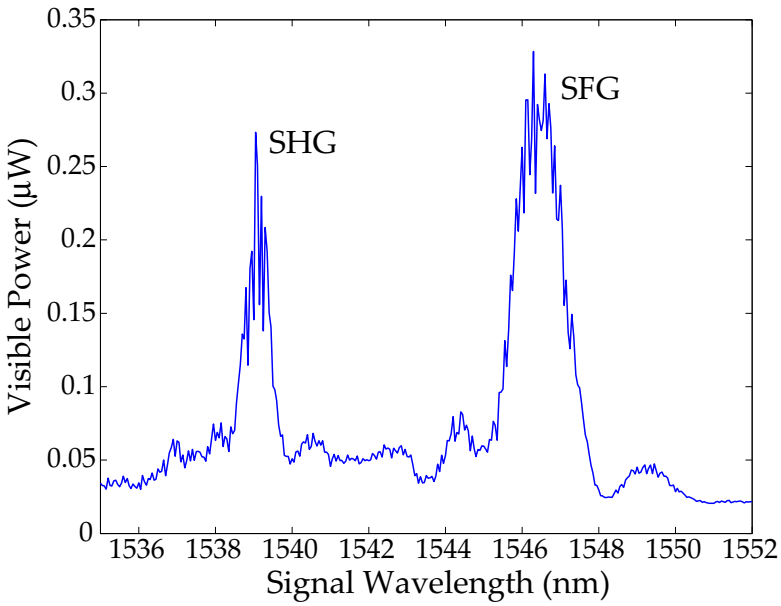

Figure 4.20: Measured power at the visible regime at the device output.

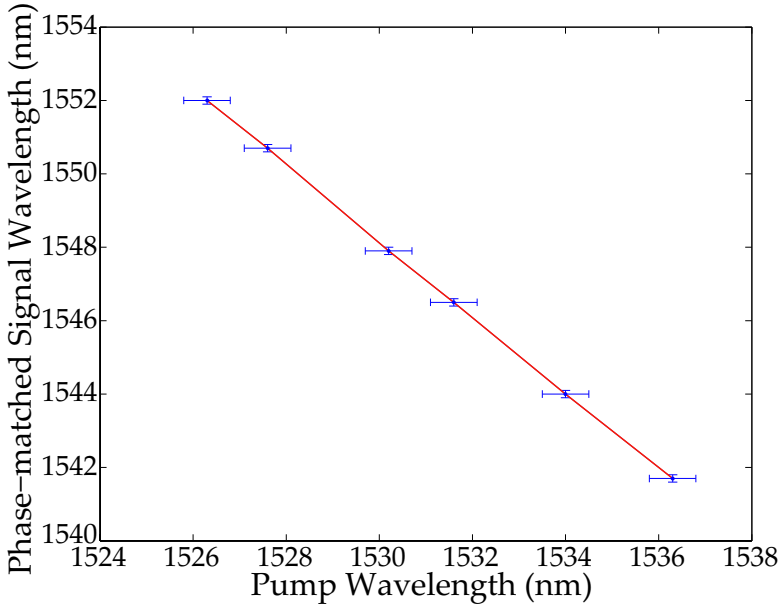

Figure 4.21: Phase-matched signal wavelength for SFG interaction as a function of the pump wavelength.

peak FWHM (0.75 nm), as expected.* Figure 4.21 shows a plot of the phase-matched signal wavelength for the SFG interaction as a function of the pump wavelength.

4.6 Summary

A brief overview on the fabrication of the device was presented early in this chapter. Characterisations on the first two steps of the waveguide fabrication were presented as well. The description of the device was given, and we are interested in a device, which was used throughout this research work, with a QPM structure of period $\Lambda = 15\,\mu$m and a buried waveguide of nominal width $w = 6\,\mu$m. The coupling efficiency with a standard SMF was calculated to be ~ 2.2 dB, with an estimated propagation loss coefficient of $\alpha \approx 1$ dB/cm. The phase-matching wavelength was 1537.7 nm at a temperature of $94\,^0$C, with a tuning curve bandwidth of 0.75 nm. The measured normalised conversion efficiency was $\eta_{\text{nor}} = 30\,\%[\text{W cm}^2]^{-1}$, with $L = 26$ mm.

References

[1] L. Ming, "Fabrication and Applications of Zinc Indiffused Waveguides in Periodically Poled Lithium Niobate," Ph.D. thesis, Optoelectronics Research Centre, University of Southampton (2005).

[2] K. R. Parameswaran, R. K. Route, J. R. Kurz, R. V. Roussev, M. M. Fejer, and M. Fujimura, "Highly Efficient Second-Harmonic Generation in Buried Waveguides Formed by Annealed and Reverse Proton Exchange in Periodically Poled Lithium Niobate," Optics Letters **27**(3), 179–181 (2002).

[3] M. Fukuma, J. Noda, and H. Iwasaki, "Optical Properties in Titanium-Diffused $LiNbO_3$ Strip Waveguides," Journal of Applied Physics **49**(7), 3693 (1978).

[4] M. L. Shah, "Optical Waveguides in $LiNbO_3$ by Ion Exchange Technique," Applied Physics Letters **26**(11), 652 (1975).

[5] J. Jackel, "High-Δn Optical Waveguides in $LiNbO_3$: Thallium-Lithium Ion Exchange," Applied Physics Letters **37**(8), 739 (1980).

[6] K. Itoh, O. Matoba, and Y. Ichioka, "Fabrication Experiment of Photorefractive Three-Dimensional Waveguides in Lithium Niobate," Optics Letters **19**(9), 652 (1994).

*Although the SFG tuning exhibits the same sinc-squared as that of SHG, their bandwidths are different, which will become clear by the following arguments. A small variation in the SFG input signal frequency $\delta\omega_{\text{S}}$ yields a variation in its sum-frequency by $\delta\omega_{\text{S}} = \delta\omega_{\text{SF}}$, whilst a small variation of the SHG input frequency yields $\delta\omega_{\text{FF}} = 2\delta\omega_{\text{SH}}$. Since ω_{FF} is the degeneracy of SFG interaction, and ω_{S} is often only slightly different with ω_{FF}, it follows that $\delta\omega_{\text{FF}} \approx \delta\omega_{\text{S}}$, such that $\delta\omega_{\text{SF}} \approx 2\delta\omega_{\text{SH}}$. Hence, the SFG tuning curve bandwidth is always approximately twice of the SHG tuning curve bandwidth.

[7] J. L. Jackel, C. E. Rice, and J. J. Veselka, "Proton Exchange for High-Index Waveguides in $LiNbO_3$," Applied Physics Letters **41**(7), 607–608 (1982).

[8] D. F. Clark, A. C. Q. Nutt, K. K. Wong, P. J. R. Laybourn, and R. M. D. L. Rue, "Characterization of Proton-Exchange Slab Optical Waveguides in z-Cut $LiNbO_3$," Journal of Applied Physics **54**(11), 6218–6220 (1983).

[9] A. Yi-Yan, "Index Instabilities in Proton-Exchanged $LiNbO_3$," Applied Physics Letters **42**(8), 633–635 (1983).

[10] Y. N. Korkishko, V. A. Fedorov, M. P. D. Micheli, P. Baldi, K. E. Hadi, and A. Leycuras, "Relationships Between Structural and Optical Properties of Proton-Exchanged Waveguides on z-Cut Lithium Niobate," Applied Optics **35**(36), 7056–7060 (1996).

[11] T. Suhara, H. Tazaki, and H. Nishihara, "Measurement of Reduction in SHG Coefficient of $LiNbO_3$ by Proton Exchanging," Electronics Letters **25**(20), 1326–1328 (1989).

[12] M. L. Bortz and M. M. Fejer, "Measurement of the Second-Order Nonlinear Susceptibility of Proton-Exchanged $LiNbO_3$," Optics Letters **17**(10), 704–706 (1992).

[13] V. A. Ganshin and Y. N. Korkishko, "H:$LiNbO_3$ Waveguides: Effects of Annealing," Optics Communications **86**, 523–530 (1991).

[14] A. Loni, G. Hay, R. M. de la Rue, and J. M. Winfield, "Proton-Exchanged $LiNbO_3$ Waveguides: The Effects of Post-Exchange Annealing and Buffered Melts as Determined by Infrared Spectroscopy, Optical Waveguide Measurements, and Hydrogen Isotopic Exchange Reactions." Journal of Lightwave Technology **7**(6), 911–919 (1989).

[15] P. G. Suchoski, T. K. Findakly, and F. J. Leonberger, "Stable Low-Loss Proton-Exchanged $LiNbO_3$ Waveguide Devices with No Electro-Optic Degradation," Optics Letters **13**(11), 1050–1052 (1988).

[16] X. Cao, R. Srivastava, R. V. Ramaswamy, and J. Natour, "Recovery of Second-Order Optical Nonlinearity in Annealed Proton-Exchanged $LiNbO_3$," IEEE Photonics Technology Letters **3**(1), 25–27 (1991).

[17] M. L. Bortz, L. A. Eyres, and M. M. Fejer, "Depth Profiling of the d_{33} Nonlinear Coefficient in Annealed Proton Exchanged $LiNbO_3$," Applied Physics Letters **62**(17), 2012–2014 (1993).

[18] M. D. Micheli, J. Botineau, S. Neveu, P. Sibillot, D. B. Ostrowsky, and M. Papuchon, "Independent Control of Index and Profiles in Proton-Exchanged Lithium Niobate Guides," Optics Letters **8**(2), 114–115 (1983).

[19] M. L. Bortz and M. M. Fejer, "Annealed Proton-Exchanged $LiNbO_3$ Waveguides," Optics Letters **16**(23), 1844–1846 (1991).

[20] V. A. Ganshin, Y. N. Korkishko, and V. Z. Petrova, "Reverse Ion-Exchange in H:$LiNbO_3$ Optical Waveguides," Zhurnal Tekhniczekoi Fiziki **58**(6), 1168–1170 (1988).

[21] Y. Korkishko, V. Fedorov, T. Morozova, F. Caccavale, F. Gonella, and F. Segato, "Reverse Proton Exchange for Buried Waveguides in $LiNbO_3$," Journal of Optical Society of America A **15**(7), 1838 (1998).

[22] N. Ramanujam, "Optimizing KTP and $LiTaO_3$ Channel Waveguides for Quasi-Phase-Matched Second Harmonic Generation with High Conversion Efficiency," IEEE Journal of Quantum Electronics **33**(2), 152–163 (1997).

[23] Y. N. Korkishko and V. A. Fedorov, "Relationship Between Refractive Indices and Hydrogen Concentration in Proton Exchanged $LiNbO_3$ Waveguides," Journal of Applied Physics **82**(3), 1010–1017 (1997).

[24] M. M. Howerton, W. K. Burns, P. R. Skeath, and A. S. Greenblatt, "Dependence of Refractive Index on Hydrogen Concentration in Proton Exchanged $LiNbO_3$," IEEE Journal of Quantum Electronics **27**(3), 593–601 (1991).

[25] P. K. Tien, S. Riva-Sanseverino, and R. J. Martin, "Optical Waveguide Modes in Single-Crystalline $LiNbO_3$-$LiTaO_3$ Solid-Solution Films," Applied Physics Letters **24**(10), 503–506 (1974).

[26] J. M. White and P. F. Heidrich, "Optical Waveguide Refractive Index Profiles Determined from Measurement of Mode Indices: A Simple Analysis," Applied Optics **15**(1), 151–155 (1976).

[27] Y. M. Dikaev, Y. L. Kopylov, and I. M. Kotelyanskii, "A Simple Method of Determining the Profiles of Diffused Waveguides," Soviet Journal of Quantum Electronics (Kvantovaya Electronika) **11**, 225–226 (1981).

[28] K. S. Chiang, "Construction of Refractive-Index Profiles of Planar Dielectric Waveguides from the Distribution of Effective Indexes," Journal of Lightwave Technology **LT-3**(2), 385–391 (1985).

[29] N. Goto and G. L. Yip, "Characterization of Proton-Exchange and Annealed $LiNbO_3$ Waveguides with Pyrophosphoric Acid," Applied Optics **28**(1), 60–65 (1989).

[30] M. Lees, "A Linear Three-Level Difference Scheme for Quasilinear Parabolic Equations," Mathematics of Computation **20**, 516–522 (1966).

[31] J. A. Arnaud, W. M. Hubbard, G. D. Mandeville, B. de la Claviere, E. A. Franke, and J. M. Franke, "Technique for Fast Measurement of Gaussian Laser Beam Parameters," Applied Optics **10**(12), 2775–2776 (1971).

[32] J. M. Khosrofian and B. A. Garetz, "Measurement of a Gaussian Laser Beam Diameter Through the Direct Inversion of Knife-Edge Data," Applied Optics **22**(21), 3406–3410 (1983).

[33] R. Regener and W. Sohler, "Loss in Low-Finesse Ti:$LiNbO_3$ Optical Waveguide Resonators," Applied Physics B **36**, 143–147 (1985).

[34] R. G. Walker, "Simple and Accurate Loss Measurement Technique for Semiconductor Optical Waveguides," Electronics Letters **21**(13), 581–583 (1985).

[35] R. S. Weis and T. K. Gaylord, "Lithium Niobate: Summary of Physical Properties and Crystal Structure," Applied Physics A **37**, 191–203 (1985).

[36] D. H. Jundt, "Temperature-Dependent Sellmeier Equation for The Index of Refraction, n_e, in Congruent Lithium Niobate," Optics Letters **22**(20), 1553–1555 (1997).

Chapter 5

Ultrashort Pulse Parametric Interactions

In contrast to nonlinear interaction with monochromatic continuous-waves, parametric interactions of ultrashort pulses are more complicated due to their broad spectrum. Chromatic dispersion causes the envelopes of the ultrashort pulses at different wavelengths to propagate at different group velocities. This group-velocity-mismatch (GVM) leads to the temporal walk-off effect which manifests prominently in SHG owing to the large gradient of the refractive index toward the lower wavelengths regime. Therefore, one needs to establish a characteristic length, called the walk-off length, after which the SH pulse is substantially broadened compared to the input FF pulse. In the frequency-domain, the temporal walk-off effect translates into a finite conversion bandwidth for the SHG interaction. When the spectral bandwidth of the FF pulse is less than the conversion bandwidth of the SHG interaction, the SH pulse temporal width equals to the temporal width of the FF pulse squared. However, if the input FF pulse has a large spectral bandwidth, the SHG bandwidth is insufficient to convert its spectrum, resulting in a broader SH pulse. Whilst the temporal walk-off effect on ultrashort pulse SHG had been recognised since the early days of nonlinear optics[1,2] and there had been extensive research on the subject,[3–8] its effect on other parametric interactions has not been thoroughly investigated.

In this chapter, we present theoretical analyses and numerical simulations of ultrashort-pulse parametric interactions which serve as the fundamentals to understand the basics and experimental results of the frequency-resolved optical gating (FROG) techniques discussed in the next chapters. This chapter is organised as follows; it will begin with the general description of pulse propagation in $LiNbO_3$ in section 5.1.

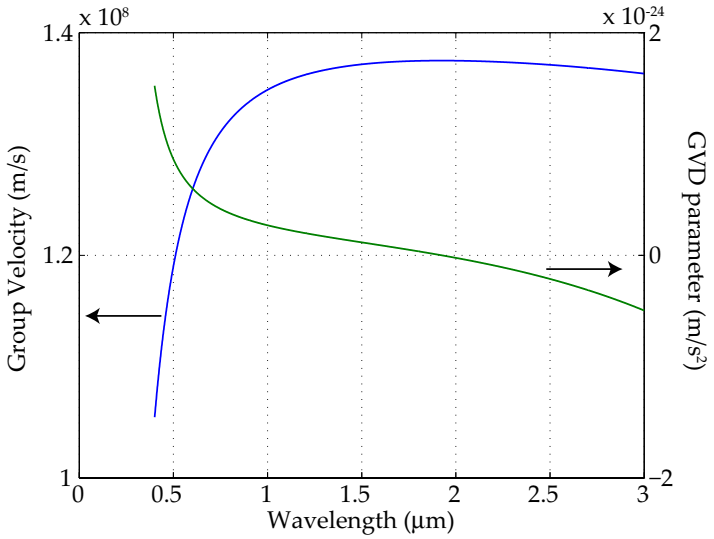

Figure 5.1: The group velocity v_g (blue) and the GVD parameter β (green) for electric-field polarised parallel to the z-axis of the bulk Lithium Niobate crystal as calculated for the extraordinary refractive index from the Sellmeier equation[10] at a temperature $T = 100\,^0$C.

In section 5.2, the theoretical analysis on the ultrashort pulse SHG in the frequency-domain, based on the work of Ref. 8, shall be reviewed briefly. This theoretical analysis will be complemented by numerical simulations in the time-domain, based on the full coupled-mode equations, in order to gain deeper physical understanding. This analysis of ultrashort pulse SHG can be trivially extended to sum-frequency and difference-frequency generations (SFG and DFG) which will be presented in Sections 5.3 and 5.4, respectively. We shall then further extend these results to analyse the ultrashort pulse cascaded $\chi^{(2)} : \chi^{(2)}$ SHG:DFG interaction[9] in section 5.5 in order to understand a novel FROG configuration proposed and demonstrated in Chapter 7.

5.1 Ultrashort Pulse Propagation in $LiNbO_3$ Waveguides

The propagation of an ultrashort optical pulse with a central frequency ω_0 in a single-mode waveguide can be described by the following electric-field [cf. Eq. (3.22)]:

$$\mathbf{E}(\mathbf{r}, t) = \mathbf{F}(x, y)A(z, t)\exp\left[i(\beta z - \omega_0 t)\right] + \text{c.c}, \tag{5.1}$$

where $A(z, t) \in \mathbb{C}$ is a slowly-varying amplitude both in time and space [see Eq. (2.2)]. We shall now introduce a frequency-domain envelope $\hat{A}(z, \Omega_j)$, instead of the standard $\hat{A}(z, \omega)$, to simplify the subsequent analysis. Hence, the Fourier transform of Eq. (5.1)

in the frequency detuning coordinate, $\Omega_j = \omega - \omega_j$, is given by:

$$\mathcal{F}\left[\mathbf{E}(\mathbf{r},t)\right] = \hat{\mathbf{E}}(\mathbf{r},\Omega_j) = \frac{1}{2\pi}\int_{-\infty}^{\infty}\mathbf{E}(\mathbf{r},t)\exp\left(i\Omega_j t\right)dt, \tag{5.2}$$

can be written as follows

$$\hat{\mathbf{E}}(\mathbf{r},\Omega_j) = \mathbf{F}(x,y)\hat{A}(z,\Omega_0)\exp\left[i\beta(\omega_0+\Omega_0)z\right)] + \text{c.c.} \tag{5.3}$$

Importantly, the chromatic dispersion of the waveguide device causes the spectral components of the pulse to travel with different phase velocities $v_p = \frac{\omega}{\beta(\omega)}$. Hence, the propagation of an ultrashort pulse is governed by its range of wavevectors $\beta(\omega_0+\Omega_0)$, which can be expanded in Taylor series as follows:

$$\beta(\omega_0+\Omega_0) = \beta(\omega_0) + \Omega_0\left.\frac{d\beta(\omega)}{d\omega}\right|_{\omega=\omega_0} + \frac{1}{2}\Omega_0^2\left.\frac{d^2\beta(\omega)}{d\omega^2}\right|_{\omega=\omega_0} + \frac{1}{6}\Omega_0^3\left.\frac{d^3\beta(\omega)}{d\omega^3}\right|_{\omega=\omega_0} + \ldots. \tag{5.4}$$

The first term simply describes the effective refractive index experienced by the electromagnetic wave. The second term describes the speed u_0 at which the envelope of an ultrashort pulse propagates, called the group velocity:

$$u_0 = \left[\frac{d\beta(\omega)}{d\omega}\right]^{-1}_{\omega=\omega_0} = c\left[\mathcal{N}(\omega) + \omega_0\frac{d\mathcal{N}(\omega)}{d\omega}\right]^{-1}_{\omega=\omega_0}. \tag{5.5}$$

Consequently, the third term determines how the group velocity changes as a function of the frequency, referred to as the group velocity dispersion (GVD) parameter:

$$b_0 = \left.\frac{d^2\beta(\omega)}{d\omega^2}\right|_{\omega=\omega_0} = \frac{1}{c}\left[2\frac{d\mathcal{N}(\omega)}{d\omega} + \omega\frac{d^2\mathcal{N}(\omega)}{d\omega^2}\right]_{\omega=\omega_0}. \tag{5.6}$$

This GVD parameter, which measures the dispersion rate of the pulse spectral components, is responsible for the broadening of a transform-limited ultrashort pulse.[11] The higher-order terms are usually neglected, except near the zero-dispersion wavelength, at which the GVD parameter vanishes, i.e. $b_0 = 0$. Figure 5.1 shows the group velocity u and the GVD parameter β as a function of wavelength, as calculated from the Sellmeier equation for the extraordinary refractive index of Lithium Niobate.[10] As can be seen, at around $1.5\,\mu$m $b \neq 0$, and thus we do not need to consider higher order dispersion than GVD. The length over which the GVD parameter becomes important is called the dispersion length, and is defined as follows:

$$L_d = \frac{\tau^2}{|b|}. \tag{5.7}$$

Figure 5.2: Illustration of the GVM and GVD effects on two pulses of different frequencies, ω_1 and ω_2, in bulk $LiNbO_3$. Given $\omega_1 < \omega_2$, it follows from Fig. 5.1 that $u_1 > u_2$. Whilst GVM is responsible for separating the two pulses after propagating in the material, GVD is responsible for the pulse broadening.

When two pulses of different central frequencies co-propagate with each other in a waveguide device, the waveguide's chromatic dispersion causes them to move with different group velocities. This group-velocity-mismatch (GVM) yields the temporal walk-off effect. The length over which the pulses walk through each other is called the walk-off length. The walk-off length is defined as

$$L_w = \frac{\tau}{|\delta\nu|}, \tag{5.8}$$

where τ is the width of the widest pulse, while $\delta\nu = \frac{1}{u_1} - \frac{1}{u_2}$ is the GVM parameter between the two pulses. As previously mentioned, after one walk-off length, the generated SH pulse in SHG interaction experiences substantial broadening compared to the input FF pulse. In general, the dispersion length is much longer than the walk-off length, i.e. $L_d \gg L_w$, and thus the GVD parameter is often neglected in short devices. Figure 5.2 shows an illustration of these GVM and GVD effects.

The fabrication of waveguide structures in $LiNbO_3$ introduces a small localised perturbation to the refractive index profile, changing the chromatic dispersion of the material, and thus resulting in the shift of the required QPM period to phase-match a certain wavelength of about 2-3 μm. This dispersion change, nevertheless, causes only a slight change in the GVM and GVD parameter. For instance, the GVM for SHG from 1.55 μm is 0.31 ps/mm in bulk $LiNbO_3$ and increases to 0.36 ps/mm in an annealed proton exchanged waveguide.[12] Furthermore, the exact waveguide dispersion will vary depending on the fabrication condition. Therefore, the dispersion of bulk Lithium Niobate is a good approximation to the waveguide dispersion for the parameters in the numerical simulations.

5.2 Second-Harmonic Generation

In this section, we shall present the theoretical analysis of ultrashort pulse SHG in the frequency-domain based on the work of Ref. 8. Numerical simulations in the time-domain will also be provided to give a deeper physical understanding of the interaction.

5.2.1 Frequency-Domain Treatment

The nonlinear polarisation for SHG [Eq. (3.12)] in the frequency-domain is given by a convolution:

$$P_{\alpha}^{\mathrm{NL}}(\mathbf{r},\Omega_{\mathrm{SH}}) = \varepsilon_0 \int_{-\infty}^{\infty} \chi_{\alpha\beta\gamma}^{(2)} E_{\beta}(\mathbf{r},\Omega_{\mathrm{FF}}) E_{\gamma}(\mathbf{r},\Omega_{\mathrm{SH}}-\Omega_{\mathrm{FF}}) d\Omega_{\mathrm{FF}}. \tag{5.9}$$

Substituting the above equation and Eq. (5.3) into the Fourier transform of Eq. (3.9), utilising the slowly-varying amplitude approximation, and assuming an undepleted FF pulse yield the following solution for the SH wave envelope after propagation through an interaction length L:

$$\hat{A}(L,\Omega_{\mathrm{SH}}) = -i\sqrt{\eta_{\mathrm{nor}}^{(\mathrm{SHG})}} \int_0^L dz \int_{-\infty}^{\infty} \hat{A}(\Omega_{\mathrm{FF}}) \hat{A}(\Omega_{\mathrm{SH}}-\Omega_{\mathrm{FF}}) \times \exp\left[-i\Delta\beta_{\mathrm{SHG}}(\Omega_{\mathrm{FF}},\Omega_{\mathrm{SH}})z\right] d\Omega_{\mathrm{FF}}, \tag{5.10}$$

where $\eta_{\mathrm{nor}}^{(\mathrm{SHG})}$ is the normalised efficiency as defined by Eq. (3.18), and the SHG wavevector mismatch is given by

$$\Delta\beta_{\mathrm{SHG}}(\Omega_{\mathrm{FF}},\Omega_{\mathrm{SH}}) = \beta(\omega_{\mathrm{SH}}+\Omega_{\mathrm{SH}}) - \beta(\omega_{\mathrm{FF}}+\Omega_{\mathrm{FF}}) - \beta(\omega_{\mathrm{FF}}+\Omega_{\mathrm{SH}}-\Omega_{\mathrm{FF}}) - K_{\mathrm{QPM}}. \tag{5.11}$$

Assuming that the frequency detunings are negligible compared to the central frequencies, i.e. $\Omega_{\mathrm{FF}},\Omega_{\mathrm{SH}} \ll \omega_{\mathrm{FF}},\omega_{\mathrm{SH}}$, Eq. (5.11) can then be expanded in Taylor series as:

$$\Delta\beta_{\mathrm{SHG}}(\Omega_{\mathrm{FF}},\Omega_{\mathrm{SH}}) = \Delta\beta_{\mathrm{SHG}}^{(0)} + \delta\nu_{\mathrm{SHG}}\Omega_{\mathrm{SH}} + \delta b\Omega_{\mathrm{SH}}^2 + b_{\mathrm{FF}}(\Omega_{\mathrm{FF}}\Omega_{\mathrm{SH}} - \Omega_{\mathrm{FF}}^2) + \mathcal{O}\left(\Omega_{\mathrm{FF}}^3,\Omega_{\mathrm{SH}}^3\right), \tag{5.12}$$

where $\Delta\beta_{\mathrm{SHG}}^{(0)} = \beta(\omega_{\mathrm{SH}}) - 2\beta(\omega_{\mathrm{FF}}) - K_{\mathrm{QPM}}$ is the QPM central frequencies wavevector mismatch for SHG (see section 3.5), whereas $\delta\nu_{\mathrm{SHG}} = \frac{1}{u_{\mathrm{SH}}} - \frac{1}{u_{\mathrm{FF}}}$ is the GVM parameter and $\delta b = b_{\mathrm{SH}} - b_{\mathrm{FF}}$ is the GVD mismatch between the FF and the SH pulses. Since the GVD and higher order dispersions are negligible compared to the GVM (as discussed in previous section) Eq. (5.12) is left with the Ω_{SH}-dependent term only. Hence, the

exponential term in Eq. (5.10) can be factored out of the convolution integral to yield the following relation:

$$\hat{A}_{\mathrm{SH}}(L,\Omega_{\mathrm{SH}}) = D_{\mathrm{SHG}}(\Omega_{\mathrm{SH}})\left[\hat{A}_{\mathrm{P}}(\Omega_{\mathrm{SH}}) * \hat{A}_{\mathrm{P}}(\Omega_{\mathrm{SH}})\right], \tag{5.13}$$

where $*$ denotes convolution, and $D_{\mathrm{SHG}}(\Omega_{\mathrm{SH}})$ is the SHG transfer function given by:

$$\begin{aligned} D_{\mathrm{SHG}}(\Omega_{\mathrm{SH}}) &= -i\sqrt{\eta_{\mathrm{nor}}^{(\mathrm{SHG})}}\int_0^L \exp\left[-i\left(\Delta\beta_{\mathrm{SHG}}^{(0)} + \delta\nu_{\mathrm{SHG}}\Omega_{\mathrm{SH}}\right)z\right]dz, \\ &= -i\sqrt{\eta_{\mathrm{nor}}^{(\mathrm{SHG})}}L\,\mathrm{sinc}\left[\left(\Delta\beta_{\mathrm{SHG}}^{(0)} + \delta\nu_{\mathrm{SHG}}\Omega_{\mathrm{SH}}\right)\frac{L}{2}\right] \\ &\qquad \times \exp\left[-i\left(\Delta\beta_{\mathrm{SHG}}^{(0)} + \delta\nu_{\mathrm{SHG}}\Omega_{\mathrm{SH}}\right)\frac{L}{2}\right]. \end{aligned} \tag{5.14}$$

The transfer function $D_{\mathrm{SHG}}(\Omega_{\mathrm{SH}})$, which relates the spectrum of the output SH pulse to the autoconvolution of the FF spectrum, only depends on the waveguide dispersion and is independent of the input FF pulse parameters. Therefore, the quantity $|D_{\mathrm{SHG}}(\Omega_{\mathrm{SH}})|^2$ can be considered as a spectral filter function, which has the the same functional form as the CW SHG tuning curve [see Eq. (3.16), and Fig. 3.2]. Physically speaking, the presence of this particular transfer function is expected, since we know that in the CW case the device has a finite bandwidth, and thus the same would be expected in the pulse interactions. It is noteworthy that the bandwidth (FWHM) of the transfer function, given by $\delta\Omega = \frac{5.56}{\delta\nu L}$, is exactly the same as that of the wavelength tuning in the CW case [Eq. (3.19)]. Hence, the temporal envelope of the output SH wave described by Eq. (5.13) is a square-like pulse whose width scales linearly with the interaction length, and acquires a time-shift of $\delta\nu_{\mathrm{SHG}}\frac{L}{2}$ with respect to the FF pulse, if its spectral width is larger than the bandwidth of the transfer function.

5.2.2 Numerical Simulations

In order to gain deeper understanding of the physics of ultrashort pulse SHG, we supplement the frequency-domain treatment presented in the previous section, with numerical simulations based on the following coupled-mode equations in the time-domain:

$$\begin{aligned} \frac{\partial A_{\mathrm{FF}}}{\partial z} + \frac{1}{u_{\mathrm{FF}}}\frac{\partial A_{\mathrm{FF}}}{\partial t} + i\frac{b_{\mathrm{FF}}}{2}\frac{\partial^2 A_{\mathrm{FF}}}{\partial t^2} &= 2i\omega_{\mathrm{FF}}\kappa_{\mathrm{FF}}A_{\mathrm{FF}}^{*}A_{\mathrm{SH}}\exp\left[i\Delta\beta_{\mathrm{SHG}}^{(0)}z\right], \\ \frac{\partial A_{\mathrm{SH}}}{\partial z} + \frac{1}{u_{\mathrm{SH}}}\frac{\partial A_{\mathrm{SH}}}{\partial t} + i\frac{b_{\mathrm{SH}}}{2}\frac{\partial^2 A_{\mathrm{SH}}}{\partial t^2} &= i\omega_{\mathrm{FF}}\kappa_{\mathrm{SH}}A_{\mathrm{SH}}^{2}\exp\left[-i\Delta\beta_{\mathrm{SHG}}^{(0)}z\right]. \end{aligned} \tag{5.15}$$

Since SHG is a special case of three-wave mixing, the above coupled-mode equations can be readily obtained from the coupled-mode equations for the more general three-wave mixing case derived in Appendix A. These coupled-mode equations go beyond the

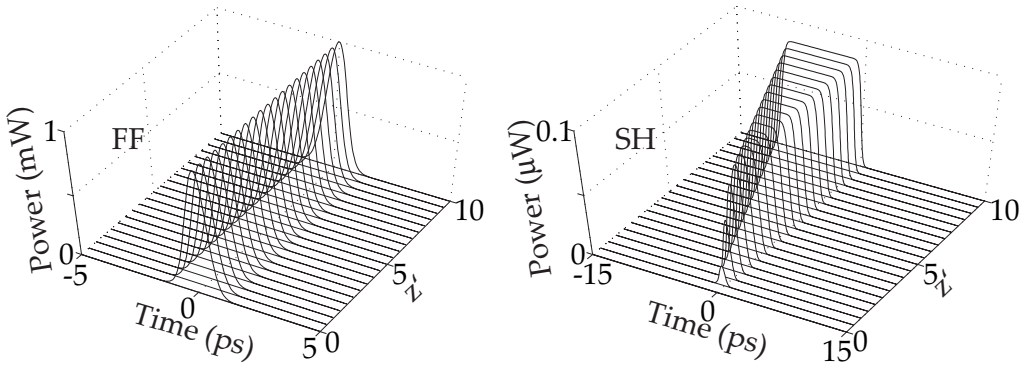

(a)

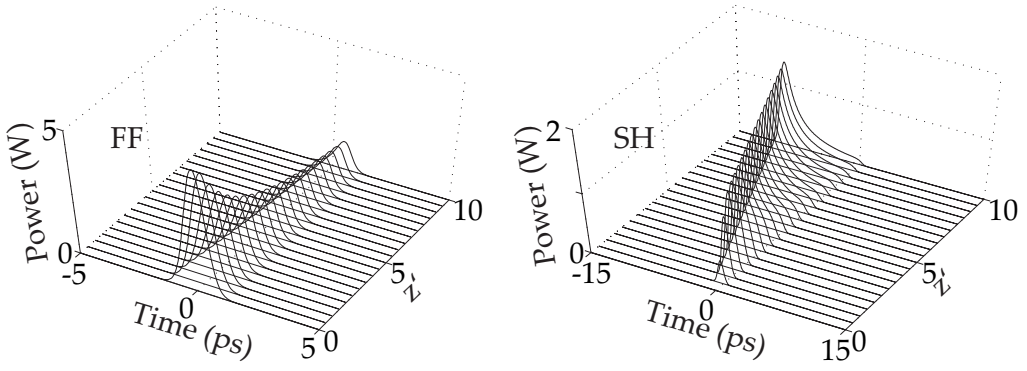

(b)

Figure 5.3: Results of numerical simulations for ultrashort pulse SHG. The figure shows the propagation of the FF and SH pulses. The input FF pulse is a transform-limited Gaussian of width 1 ps with peak power of a) 1 mW, and b) 5 W. The device had a normalised efficiency of $\eta_{\text{nor}} \approx 75\%[\text{W cm}^2]^{-1}$. The wavelength of the FF pulse is $\lambda_{\text{FF}} = 1.540\,\mu$m. The QPM period was chosen such that the phase-matching condition is met.

approximations used in the frequency domain treatment, including both pump depletion and GVD. The coupled-mode equations were solved using the symmetric split-step Fourier method[11] with a Runge-Kutta integrator in the FF pulse frame of reference. We considered an SHG interaction starting with a single input FF pulse at $\lambda_{\mathrm{FF}} = 1.540\,\mu\mathrm{m}$. The required QPM period to phase-match this wavelength in bulk material is $\Lambda = 18.44\,\mu\mathrm{m}$ at $T = 100\,^0\mathrm{C}$. The waveguide linear dispersion properties in the simulations are approximated by the bulk Lithium Niobate parameters, whereas the normalised conversion efficiency [Eq. (3.18)] is chosen to be $\eta_{\mathrm{nor}} \approx 75\%[\mathrm{W\,cm^2}]^{-1}$, a typical value for annealed proton-exchange waveguides.[12,13]

Figure 5.3(a) shows the propagation of FF and SH pulses as obtained by solving Eq. (5.15) using a 1 ps wide transform-limited (TL) Gaussian FF pulse with a peak power of 1 mW. The FF pulse power level is sufficiently low to be considered undepleted for direct comparison with the frequency-domain treatment. The propagation lengths against which the pulses are plotted have been normalised to the walk-off length, i.e. $z' = \frac{z}{L_w}$. The walk-off length is defined as $L_w = \frac{\tau_{\mathrm{FF}}}{|\delta\nu_{\mathrm{SHG}}|}$, where τ_{FF} is the temporal FWHM of the FF pulse. The device length used in the simulation was $10L_w$, which corresponds to a bandwidth of $\delta\Omega = \frac{5.56}{10\tau_{\mathrm{FF}}} = 0.556\,\mathrm{THz}$. The numerical simulation results are in excellent agreement with the frequency-domain treatment. The temporal walk-off effect causes the SH pulse component generated in a certain position z in the device to be time-shifted by $\delta\nu_{\mathrm{SHG}}z$ with respect to the FF pulse. This results in a total time-shift of $\delta\nu_{\mathrm{SHG}}\frac{z}{2}$ after propagating through a length z with respect to the FF pulse and in the broadening of the SH pulse. Therefore, when the interaction length exceeds the one-walk-off length limit, the SH pulsewidth increases linearly with L with a rate determined by the GVM parameter $\delta\nu_{\mathrm{SHG}}$.

Figure 5.3(b) again shows the propagation of the FF and the SH pulses, but for an FF pulse peak power of 5 W. As observed in the plots, such a high peak power leads to the depletion of the FF pulse. This depletion causes the SH pulse components to be generated with different efficiencies at different positions in the device. Hence, the interplay between the temporal walk-off effect and the depletion of the FF pulse results in the distortion of the SH pulse as apparent in the plot.

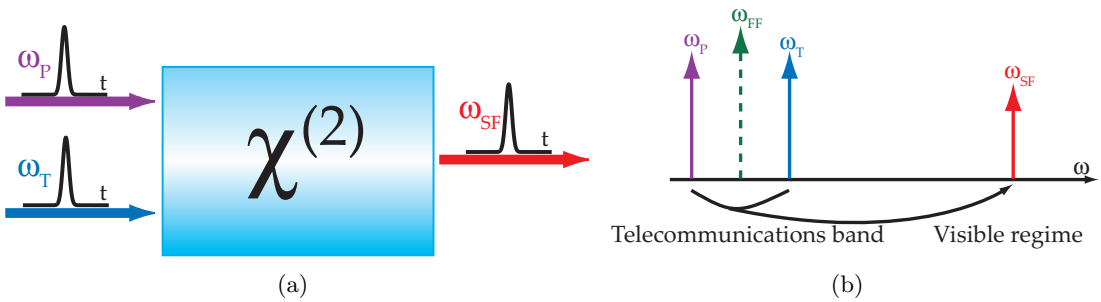

(a) (b)

Figure 5.4: Illustrations of the ultrashort pulse SFG in the QPM waveguide device. A test pulse with a central frequency ω_{T} and a pump pulse with central-frequency ω_{P}, which are slightly different from the degenerate frequency ω_{FF} in the telecommunications-band, interact in the $\chi^{(2)}$ device generating an output pulse at the sum-frequency $\omega_{\mathrm{SF}} = \omega_{\mathrm{T}} + \omega_{\mathrm{P}}$.

5.3 Sum-Frequency Generation

Moving from SHG, we now discuss sum-frequency generation (SFG), which has two input pulses at distinct frequencies, and is more general case of three-wave mixing than SHG. We consider SFG input pulses which are only slightly different from the degenerate frequency ω_{FF}, namely test and pump pulses with central frequencies at ω_{T} and ω_{P}, respectively. These input pulses interact with each other in the $\chi^{(2)}$ device to generate an output sum-frequency (SF) pulse with a central-frequency $\omega_{\mathrm{SF}} = \omega_{\mathrm{T}} + \omega_{\mathrm{P}}$ in the visible regime, as illustrated in Fig. 5.4. Although the analysis of ultrashort pulse SHG in the previous section can be trivially extended to SFG, the results have not been presented in previous publications, to the best of our knowledge.

5.3.1 Frequency-Domain Treatment

The generalisation of the previous frequency-domain treatment for SHG to SFG is straightforward. Assuming undepleted pump and test pulses, the solution for the SF pulse envelope after propagation through an interaction length L is given by:

$$\hat{A}(z,\Omega_{\mathrm{SF}}) = -i2\sqrt{\eta_{\mathrm{nor}}^{(\mathrm{SFG})}}\int_0^L dz \int_{-\infty}^{\infty} \hat{A}_{\mathrm{P}}(\Omega_{\mathrm{P}})\hat{A}_{\mathrm{S}}(\Omega_{\mathrm{SF}}-\Omega_{\mathrm{P}}) \exp\left[-i\Delta\beta_{\mathrm{SFG}}(\Omega_{\mathrm{P}},\Omega_{\mathrm{SF}})z\right]d\Omega_{\mathrm{P}}, \quad (5.16)$$

where $\eta_{\mathrm{nor}}^{(\mathrm{SFG})} = [\omega_{\mathrm{SF}}\kappa]^2$ is the normalised conversion efficiency, and κ is the nonlinear coupling coefficient for three-wave mixing given by Eq. (A.29). Hence, $\eta_{\mathrm{nor}}^{(\mathrm{SFG})}$ can be rewritten as:

$$\eta_{\mathrm{nor}}^{(\mathrm{SFG})} = [\omega_{\mathrm{SF}}\kappa]^2 = \omega_{\mathrm{SF}}^2 d^2 \frac{2\mu_0}{\mathcal{N}_{\mathrm{P}}\mathcal{N}_{\mathrm{T}}\mathcal{N}_{\mathrm{SF}}c}\frac{1}{S_{\mathrm{ovl}}}. \quad (5.17)$$

Since $\omega_{\mathrm{SF}} \approx \omega_{\mathrm{SH}}$, and the SHG [Eq. (3.24)] and the three-wave mixing [Eq. (A.29)] nonlinear coupling coefficients are similar, it follows that $\eta_{\mathrm{nor}}^{(\mathrm{SFG})} \approx \eta_{\mathrm{nor}}^{(\mathrm{SHG})}$. The wavevector mismatch for SFG is given by

$$\Delta\beta_{\mathrm{SFG}}(\Omega_{\mathrm{P}}, \Omega_{\mathrm{SF}}) = \beta(\omega_{\mathrm{SF}} + \Omega_{\mathrm{SF}}) - \beta(\omega_{\mathrm{P}} + \Omega_{\mathrm{P}}) - \beta(\omega_{\mathrm{T}} + \Omega_{\mathrm{SF}} - \Omega_{\mathrm{P}}) - K_{\mathrm{QPM}}, \quad (5.18)$$

which after expansion in Taylor series can be recast as follows:

$$\Delta\beta_{\mathrm{SFG}}(\Omega_{\mathrm{P}}, \Omega_{\mathrm{SF}}) = \Delta\beta_{\mathrm{SFG}}^{(0)} + \delta\nu_{\mathrm{SF,T}}\Omega_{\mathrm{SF}} + \delta\nu_{\mathrm{T,P}}\Omega_{\mathrm{P}} + \mathcal{O}(\Omega_{\mathrm{P}}^2, \Omega_{\mathrm{SF}}^2), \quad (5.19)$$

where $\Delta\beta_{\mathrm{SFG}}^{(0)} = \beta(\omega_{\mathrm{SF}}) - \beta(\omega_{\mathrm{T}}) - \beta(\omega_{\mathrm{P}}) - K_{\mathrm{QPM}}$ is the QPM central frequencies wavevector mismatch for SFG, $\delta\nu_{\mathrm{SF,T}} = \frac{1}{u_{\mathrm{SF}}} - \frac{1}{u_{\mathrm{T}}}$ is the GVM between the SF and the test pulses, and $\delta\nu_{\mathrm{T,P}} = \frac{1}{u_{\mathrm{T}}} - \frac{1}{u_{\mathrm{P}}}$ is the GVM between the test and the pump pulse. Since the test and pump pulses are only slightly different in frequency, their GVM is negligible compared to that between the SF and the test pulses, i.e. $\delta\nu_{\mathrm{T,P}} \approx 0$, and thus Eq. (5.18) is left with Ω_{SF}-dependent terms only. Hence, the exponential term in Eq. (5.16) can be factored out of the convolution, resulting in the following relation:

$$\hat{A}_{\mathrm{SF}}(L, \Omega) = D_{\mathrm{SFG}}(\Omega)\left[\hat{A}_{\mathrm{P}}(\Omega) * \hat{A}_{\mathrm{T}}(\Omega)\right]. \quad (5.20)$$

At this point, the similarity between ultrashort pulse SHG and SFG is apparent [cf. Eq. (5.13)]. The SFG transfer function $D_{\mathrm{SFG}}(\Omega)$ takes the same form as the SHG one [Eq. (5.14)], but with the GVM parameter being $\delta\nu_{\mathrm{SF,T}}$ and the central frequencies wavevector mismatch being $\Delta\beta_{\mathrm{SFG}}^{(0)}$. Since $\delta\nu_{\mathrm{SF,T}} \approx \delta\nu_{\mathrm{SHG}}$, the bandwidth of this interaction is also approximately the same as that of SHG*. It can be directly deduced that the ultrashort pulse SFG is affected by temporal walk-off in the same way as the ultrashort pulse SHG.

5.3.2 Numerical Simulations

The frequency-domain treatment is supplemented with numerical simulations in time-domain based on the following coupled-mode equations (see appendix A):

$$\begin{aligned}
\frac{\partial A_{\mathrm{P}}}{\partial z} + \frac{1}{u_{\mathrm{P}}}\frac{\partial A_{\mathrm{P}}}{\partial t} + i\frac{b_{\mathrm{P}}}{2}\frac{\partial^2 A_{\mathrm{P}}}{\partial t^2} &= 2i\omega_{\mathrm{P}}\kappa_{\mathrm{SFG}}A_{\mathrm{T}}^* A_{\mathrm{SF}} \exp\left[i\Delta\beta_{\mathrm{SFG}}^{(0)}z\right], \\
\frac{\partial A_{\mathrm{T}}}{\partial z} + \frac{1}{u_{\mathrm{T}}}\frac{\partial A_{\mathrm{T}}}{\partial t} + i\frac{b_{\mathrm{T}}}{2}\frac{\partial^2 A_{\mathrm{T}}}{\partial t^2} &= 2i\omega_{\mathrm{T}}\kappa_{\mathrm{SFG}}A_{\mathrm{P}}^* A_{\mathrm{SF}} \exp\left[i\Delta\beta_{\mathrm{SFG}}^{(0)}z\right], \\
\frac{\partial A_{\mathrm{SF}}}{\partial z} + \frac{1}{u_{\mathrm{SF}}}\frac{\partial A_{\mathrm{SF}}}{\partial t} + i\frac{b_{\mathrm{SF}}}{2}\frac{\partial^2 A_{\mathrm{SF}}}{\partial t^2} &= 2i\omega_{\mathrm{SF}}\kappa_{\mathrm{SFG}}A_{\mathrm{P}}A_{\mathrm{T}} \exp\left[-i\Delta\beta_{\mathrm{SFG}}^{(0)}z\right],
\end{aligned} \quad (5.21)$$

*It is worth noting here that the bandwidth mentioned here is the acceptance bandwidth for the FF or the T pulses at their respective frequencies. This bandwidth is not the same as the tuning bandwidth described in Section 4.5.3, which is measured at the SH or SF frequencies.

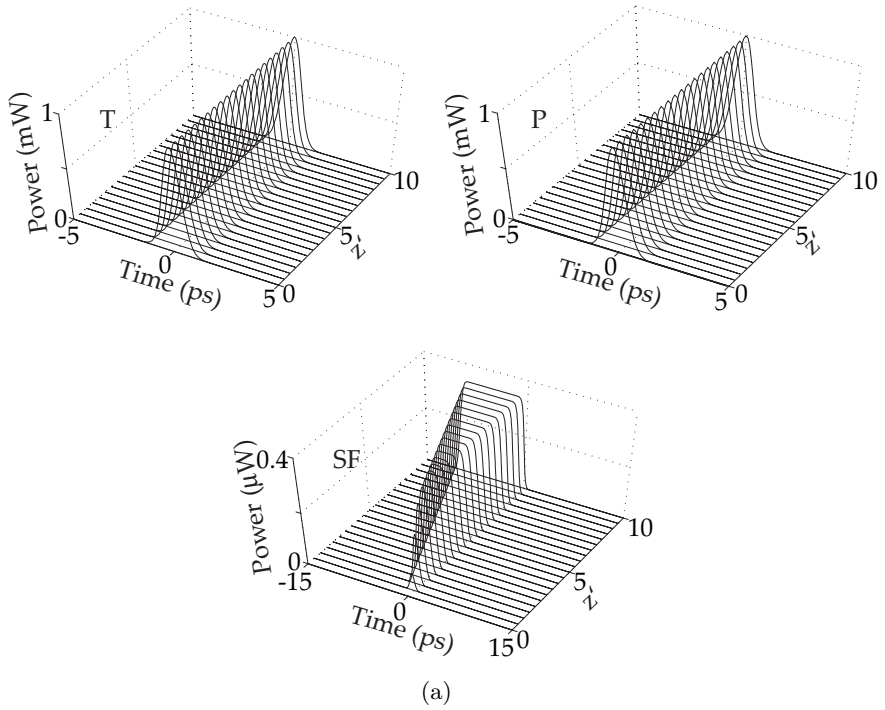

(a)

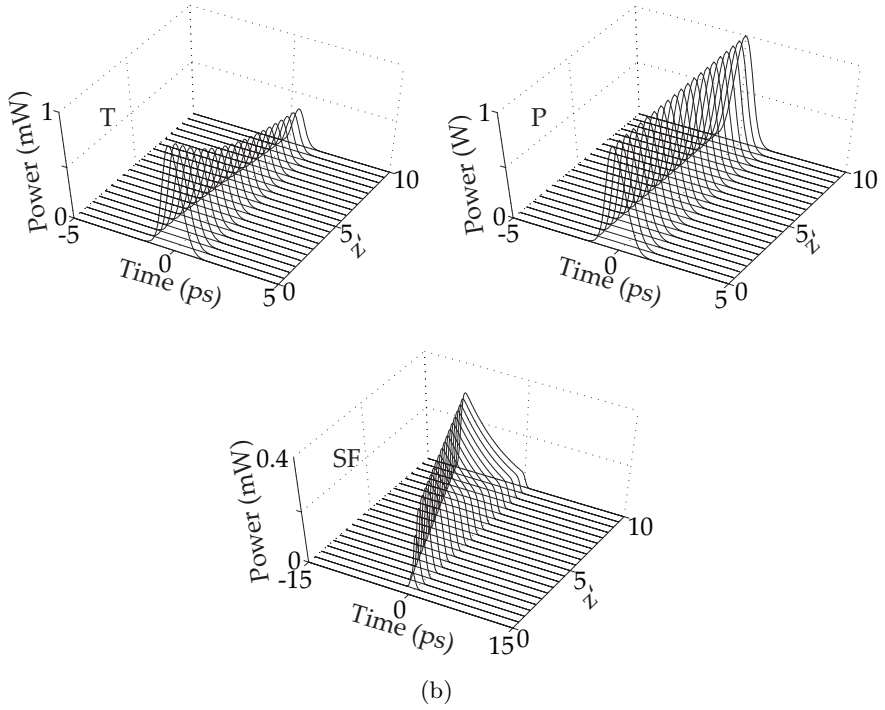

(b)

Figure 5.5: Results of numerical simulations for ultrashort pulse SFG. The figure shows the propagation of the test (T), pump (P) and sum-frequency (SF) pulses. The input T and P pulses are transform-limited Gaussians of widths 1 ps. The T pulse has a peak power of 1 mW, whereas the P pulse has a peak power of a) 1 mW, or b) 1 W. The device had a normalised efficiency of $\eta_{\text{nor}} \approx 75\%[\text{W cm}^2]^{-1}$. The wavelength of the input T and P pulses are $\lambda_{\text{T}} = 1.536\,\mu$m and $\lambda_{\text{P}} = 1.544\,\mu$m, respectively. The QPM period was chosen such that the phase-matching condition is met.

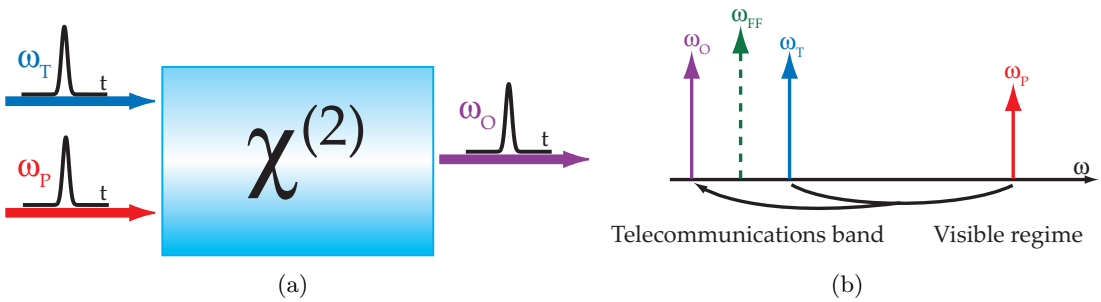

Figure 5.6: Illustrations of the ultrashort pulse DFG in the QPM waveguide device. A test pulse with a central frequency ω_{T} in the telecommunications-band interacts with a pump pulse with central-frequency ω_{P} in the visible region generating an output pulse at the difference-frequency $\omega_{\mathrm{O}} = \omega_{\mathrm{P}} - \omega_{\mathrm{T}}$ back in the telecommunications-band.

where $\kappa_{\mathrm{SFG}} \approx \kappa_{\mathrm{SHG}}$ is given by Eq. (A.29). Solving the above equations by the symmetric split-step Fourier method in the T pulse frame of reference results in Fig. 5.5, which shows the propagation of the three pulses involved (P, T and SF). The propagation lengths have been normalised against the walk-off length, defined as $L_w = \frac{\tau_{\mathrm{P}}}{|\delta\nu_{\mathrm{SF,T}}|}$, where τ_{P} is the temporal FWHM of the pump pulse. The wavelengths of the input pulses, which meet the phase-matching condition for the QPM period $\Lambda = 18.44\,\mu$m used in Fig. 5.3, are $\lambda_{\mathrm{T}} = 1.536\,\mu$m and $\lambda_{\mathrm{P}} = 1.544\,\mu$m. The input pump and test pulses are TL Gaussians of widths 1 ps. The T pulse peak power is 1 mW, whereas the P pulse peak powers are 1 mW and 1 W which correspond to Figs. 5.5(a) and 5.5(b), respectively. It is easy to see the striking resemblance between Figs. 5.5(a) and 5.3(a), and between Figs. 5.5(b) and 5.3(b). As the frequency-domain treatment shows, the physical interpretation of this process is the same as that of ultrashort pulse SHG.

5.4 Difference-Frequency Generation

In a simple difference-frequency generation (DFG) experiment, a test pulse with a central frequency ω_{T} in the telecommunications-band and a pump signal with central-frequency ω_{P} in the visible region interact with each other in the $\chi^{(2)}$ device generating an output difference-frequency pulse at $\omega_{\mathrm{O}} = \omega_{\mathrm{P}} - \omega_{\mathrm{T}}$ back in the telecommunications-band, as illustrated in Fig. 5.6. Again, the analysis of ultrashort pulse DFG can be trivially from the SHG and the SFG analyses, but the results have not been presented in previous publications, to the best of our knowledge.

5.4.1 Frequency-Domain Treatment

Following a similar derivation to the previous sections, and assuming undepleted pump and unamplified test pulses, the envelope of the difference-frequency pulse after propagation through an interaction length L is given by:

$$\hat{A}_{\mathrm{O}}(L,\Omega_{\mathrm{O}}) = -i\sqrt{\eta_{\mathrm{nor}}^{(\mathrm{DFG})}}\int_0^L dz \int_{-\infty}^{\infty} \hat{A}_{\mathrm{P}}(\Omega_{\mathrm{P}})\hat{A}_{\mathrm{T}}^{*}(\Omega_{\mathrm{P}}-\Omega_{\mathrm{O}}) \times \exp\left[-i\,\Delta\beta_{\mathrm{DFG}}(\Omega_{\mathrm{O}},\Omega_{\mathrm{P}})z\right]d\Omega_{\mathrm{P}}, \quad (5.22)$$

where $\eta_{\mathrm{nor}}^{(\mathrm{DFG})} = [\omega_{\mathrm{O}}\kappa]^2$ is the normalised conversion efficiency, and κ is the nonlinear coupling coefficient for three-wave mixing given by Eq. (A.29). Hence, $\eta_{\mathrm{nor}}^{(\mathrm{DFG})}$ can be rewritten as:

$$\eta_{\mathrm{nor}}^{(\mathrm{DFG})} = [\omega_{\mathrm{O}}\kappa]^2 = \omega_{\mathrm{O}}^2 d^2 \frac{2\mu_0}{\mathcal{N}_{\mathrm{P}}\mathcal{N}_{\mathrm{T}}\mathcal{N}_{\mathrm{O}}c}\frac{1}{S_{\mathrm{ovl}}}. \quad (5.23)$$

Since $\omega_{\mathrm{SH}} \approx 2\omega_{\mathrm{O}}$, and the SHG [Eq. (3.24)] and the three-wave mixing [Eq. (A.29)] nonlinear coupling coefficients are similar, it follows that $\eta_{\mathrm{nor}}^{(\mathrm{DFG})} \approx 4\eta_{\mathrm{nor}}^{(\mathrm{SHG})}$. The expansion of the DFG wavevector mismatch in Taylor series can be written as follows:

$$\Delta\beta_{\mathrm{DFG}}(\Omega_{\mathrm{O}},\Omega_{\mathrm{P}}) = \Delta\beta_{\mathrm{DFG}}^{(0)} + \delta\nu_{\mathrm{T,O}}\Omega_{\mathrm{O}} + \delta\nu_{\mathrm{P,T}}\Omega_{\mathrm{P}} + \mathcal{O}(\Omega_{\mathrm{O}}^2,\Omega_{\mathrm{P}}^2), \quad (5.24)$$

where $\Delta\beta_{\mathrm{DFG}}^{(0)}$ is the QPM central frequencies wavevector mismatch for DFG, while $\delta\nu_{\mathrm{T,O}}$ and $\delta\nu_{\mathrm{P,T}}$ are the GVMs between the test and the output pulse and between the test and the pump pulses, respectively. Since the output and test pulses are only slightly different in frequency, their GVM is negligible with respect to the GVM between the signal and the pump. Hence, the Ω_{O}-dependent term in Eq. (5.24) which primarily determines the width of the output pulse spectrum can be neglected and Eq. (5.22) can be recast as:

$$\hat{A}_{\mathrm{O}}(L,\Omega) = \hat{A}'_{\mathrm{P}}(L,\Omega) * \hat{A}_{\mathrm{T}}^{*}(-\Omega), \quad (5.25)$$

having introduced an effective pump pulse

$$\hat{A}'_{\mathrm{P}}(L,\Omega) = G_{\mathrm{DFG}}(\Omega)\hat{A}_{\mathrm{P}}(\Omega) \quad (5.26)$$

with the transfer function given by:

$$G_{\mathrm{DFG}}(\Omega) = -i\sqrt{\eta_{\mathrm{nor}}^{(\mathrm{DFG})}}\int_0^L \exp\left[-i(\Delta\beta_{\mathrm{DFG}}^{(0)} + \delta\nu_{\mathrm{P,T}}\Omega)z\right]dz. \quad (5.27)$$

Notice the striking similarity of the above expression with Eq. (5.14), the SHG transfer function. The above equations imply that the effective pump pulse $\hat{A}'_{\mathrm{P}}(L,\Omega)$ acquires

a $\delta\nu_{\mathrm{P,T}}\frac{z}{2}$ time-shift with respect to the test pulse during propagation and progressively broadens owing to the temporal walk-off between the test and the pump pulses. When the test and the pump pulses completely walk through each other, the nonlinear interaction ceases and the output pulse does not continue to build up. Since $\delta\nu_{\mathrm{P,T}} \approx \delta\nu_{\mathrm{SHG}}$, the DFG transfer function $G_{\mathrm{DFG}}(\Omega)$ [Eq. (5.27)] is approximately the same as the SHG one (or, equivalently, SFG) $D_{\mathrm{SHG}}(\Omega)$ [Eq. (5.14)], i.e. $D_{\mathrm{SHG}}(\Omega) \approx G_{\mathrm{DFG}}(\Omega)$. Their filtering actions, however, are different. The SHG (SFG) transfer function acts on the convolution of the input pulses, and thus the temporal walk-off effect yields a broad output pulse. The DFG transfer function, on the other hand, only acts on the pump pulse [Eq. (5.26)]. Therefore, the temporal walk-off effect has a less dramatic effect on the output difference-frequency pulse.

5.4.2 Numerical Simulations

The numerical simulation for DFG in the time-domain is based on the same coupled-mode equations as that of SFG [Eq. (5.21), and appendix A], except for the initial conditions:

$$\begin{aligned}
\frac{\partial A_{\mathrm{T}}}{\partial z} + \frac{1}{u_{\mathrm{T}}}\frac{\partial A_{\mathrm{T}}}{\partial t} + i\frac{b_{\mathrm{T}}}{2}\frac{\partial^2 A_{\mathrm{T}}}{\partial t^2} &= 2i\omega_{\mathrm{T}}\kappa_{\mathrm{DFG}}A_{\mathrm{O}}^{*}A_{\mathrm{P}}\ \exp\left[i\Delta\beta_{\mathrm{DFG}}^{(0)}z\right], \\
\frac{\partial A_{\mathrm{P}}}{\partial z} + \frac{1}{u_{\mathrm{P}}}\frac{\partial A_{\mathrm{P}}}{\partial t} + i\frac{b_{\mathrm{P}}}{2}\frac{\partial^2 A_{\mathrm{P}}}{\partial t^2} &= 2i\omega_{\mathrm{P}}\kappa_{\mathrm{DFG}}A_{\mathrm{O}}A_{\mathrm{T}}\ \exp\left[-i\Delta\beta_{\mathrm{DFG}}^{(0)}z\right], \\
\frac{\partial A_{\mathrm{O}}}{\partial z} + \frac{1}{u_{\mathrm{O}}}\frac{\partial A_{\mathrm{O}}}{\partial t} + i\frac{b_{\mathrm{P}}}{2}\frac{\partial^2 A_{\mathrm{O}}}{\partial t^2} &= 2i\omega_{\mathrm{O}}\kappa_{\mathrm{DFG}}A_{\mathrm{T}}^{*}A_{\mathrm{P}}\ \exp\left[i\Delta\beta_{\mathrm{DFG}}^{(0)}z\right],
\end{aligned} \tag{5.28}$$

where $\kappa_{\mathrm{DFG}} = \kappa_{\mathrm{SFG}} \approx \kappa_{\mathrm{SHG}}$ is the DFG nonlinear coupling coefficient. Solving the above equations by the symmetric split-step Fourier method in the T pulse frame of reference results in Fig. 5.7, which shows the propagation of the three pulses involved in the interaction (P, T, and O). The propagation lengths have been normalised against the walk-off length, defined as $L_w = \frac{\tau_{\mathrm{P}}}{|\delta\nu_{\mathrm{P,T}}|}$. The wavelengths of the input pulses, which meet the phase-matching condition for the QPM period $\Lambda = 18.44\,\mu$m used in Fig. 5.3, are $\lambda_{\mathrm{T}} = 1.536\,\mu$m and $\lambda_{\mathrm{P}} = 770\,$nm. The input pump and test pulses are TL Gaussians of widths 1 ps. The test pulse peak power is 1 mW, whereas the pump pulse peak powers are 1 mW and 5 W which correspond to Figs. 5.7(a) and 5.7(b), respectively.

The power level of the pump pulse in Fig. 5.7(a) is sufficiently low, corresponding to the assumptions used in the frequency-domain treatment, i.e. there is no pump pulse depletion and no test pulse amplification. It can be easily seen that the temporal walk-off effect does not cause the broadening of the output DF pulse, but limits the conversion

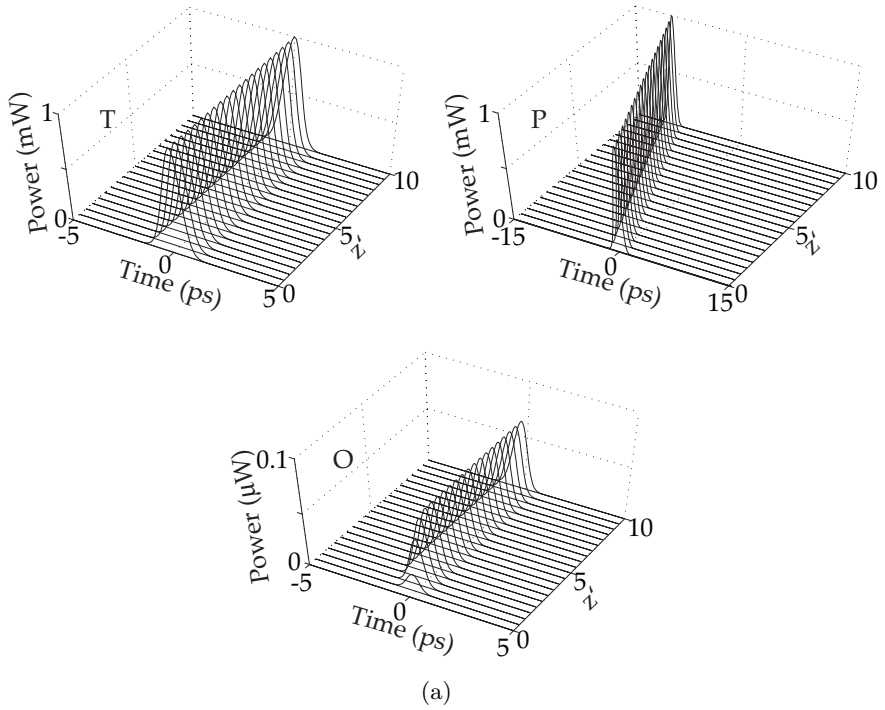

(a)

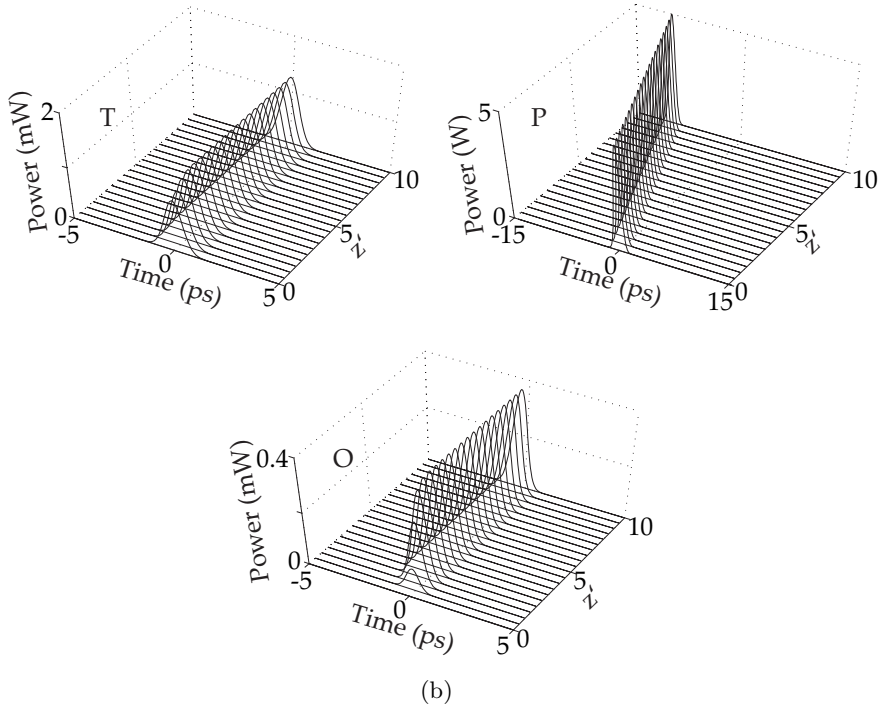

(b)

Figure 5.7: Results of numerical simulations for ultrashort pulse DFG. The figure shows the propagation of the test (T), pump (P) and output (O) pulses. The input T and P pulses are transform-limited Gaussians of widths 1 ps. The T pulse has a peak power of 1 mW, whereas the P pulse has a peak power of a) 1 mW, or b) 5 W. The device had a normalised efficiency of $\eta_{\mathrm{nor}} \approx 75\%[\mathrm{W\,cm^2}]^{-1}$. The wavelength of the input T and P pulses are $\lambda_{\mathrm{T}} = 1.536\,\mu$m and $\lambda_{\mathrm{P}} = 0.770\,\mu$m, respectively. The QPM period had been chosen such that the phase-matching condition is met.

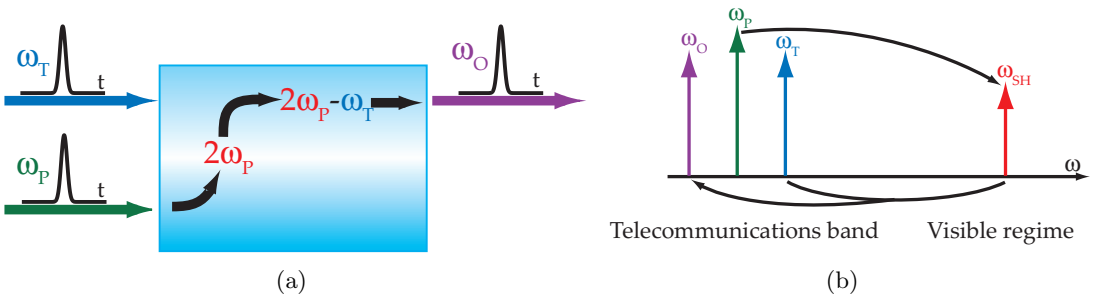

Figure 5.8: Illustrations of ultrashort pulse cascaded SHG:DFG in the QPM waveguide device. A test pulse with a central frequency ω_{T} and a pump pulse with central-frequency ω_{P}, which are slightly different from the degenerated frequency ω_{FF} in the telecommunications-band, are injected into the $\chi^{(2)}$ device. The pump is up-converted to its SH, which then generates an output pulse at $\omega_{\mathrm{O}} = 2\omega_{\mathrm{P}} - \omega_{\mathrm{T}}$ via DFG with the test pulse.

efficiency. As soon as the pump pulse is time-shifted with respect to the test and output DF pulses, which happens around one-walk-off length, the power transfer to the output DF pulse in the nonlinear interaction ceases to happen. On the other hand, the power level of the pump pulse in Fig. 5.7(b) causes some small amplification of the test pulse. Even so, the output DF pulse is undistorted by the temporal walk-off effect.

5.5 Cascaded SHG and DFG

Having analysed the SHG and DFG interactions separately, we can now consider the case when both interactions occur simultaneously, as depicted in Fig. 5.8. A pump pulse (at ω_{P}) and a test pulse (at ω_{T}), both in the telecommunications-band, are injected into the $\chi^{(2)}$ device. The pump is up-converted to its SH, which then generates an output pulse at $\omega_{\mathrm{O}} = 2\omega_{\mathrm{P}} - \omega_{\mathrm{T}}$ via DFG with the test pulse. To the best of our knowledge, detailed theoretical and numerical analyses of this interaction have not been the subject of any previous research work.

5.5.1 Frequency-Domain Treatment

The envelope of the output pulse in this interaction, after propagation over a length L, is similar to that of DFG interaction:

$$\hat{A}_{\mathrm{O}}(L,\Omega_{\mathrm{O}}) = -i\sqrt{\eta_{\mathrm{nor}}^{(\mathrm{DFG})}}\int_0^L dz\int_{-\infty}^{\infty}\hat{A}_{\mathrm{SH}}(\Omega_{\mathrm{SH}},z)\hat{A}_{\mathrm{T}}^{*}(\Omega_{\mathrm{SH}}-\Omega_{\mathrm{O}}) \times \exp\left[-i\left(\Delta\beta_{\mathrm{DFG}}^{(0)} + \delta\nu_{\mathrm{T,O}}\Omega_{\mathrm{O}}\right)z\right]d\Omega_{\mathrm{SH}}, \quad (5.29)$$

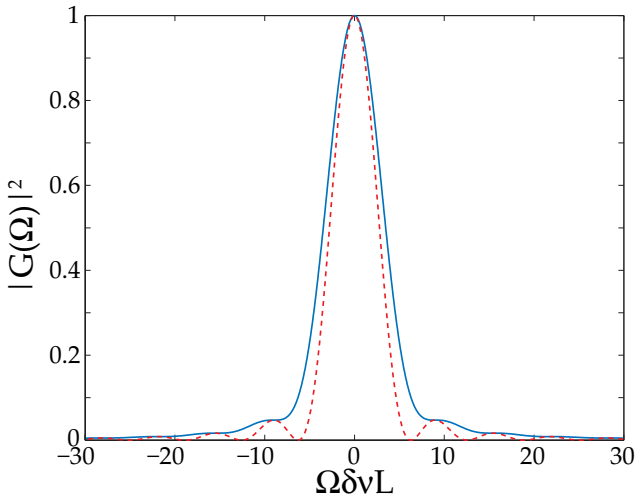

Figure 5.9: The cascaded [Eq. (5.33), solid blue line] and DFG [Eq. (5.27), dashed red line] transfer function. Compare with Fig. 3 in Ref. 14.

where $\hat{A}_{\mathrm{SH}}(\Omega_{\mathrm{SH}}, z)$ is the spatially dependent SH of the pump pulse. It is obtain by performing the integration over z instead of L in Eq. (5.10), resulting in a similar expression to Eq. (5.13):

$$\hat{A}_{\mathrm{SH}}(z, \Omega_{\mathrm{SH}}) = D_{\mathrm{SHG}}(z, \Omega_{\mathrm{SH}}) \left[\hat{A}_{\mathrm{P}}(\Omega_{\mathrm{SH}}) * \hat{A}_{\mathrm{P}}(\Omega_{\mathrm{SH}})\right], \tag{5.30}$$

where $D_{\mathrm{SHG}}(\Omega_{\mathrm{SH}}, z)$ is obtained by replacing L with z as the upper integration limit in Eq. (5.14). Substituting the above expression into Eq. (5.29) yields the following expression:

$$\hat{A}_{\mathrm{O}}(L, \Omega) = \hat{A}'_{\mathrm{SH}}(L, \Omega) * \hat{A}^{*}_{\mathrm{T}}(-\Omega), \tag{5.31}$$

where $\hat{A}'_{\mathrm{SH}}$, the effective pump for the DFG process (at $2\omega_{\mathrm{P}}$), is related to the envelope of the fundamental pulse (at ω_{P}) by:

$$\hat{A}'_{\mathrm{SH}} = G_{\mathrm{C}}(\Omega) \left[\hat{A}_{\mathrm{P}}(\Omega) * \hat{A}_{\mathrm{P}}(\Omega)\right]. \tag{5.32}$$

The SHG:DFG transfer function $G_{\mathrm{C}}(\Omega)$ takes the following form:

$$G_{\mathrm{C}}(\Omega) = -i\sqrt{\eta_{\mathrm{nor}}^{(\mathrm{DFG})}} \int_0^L D_{\mathrm{SHG}}(z, \Omega)\ \exp\left[-i(\Delta\beta_{\mathrm{DFG}}^{(0)} + \delta\nu_{\mathrm{SH,T}}\Omega)z\right] dz. \tag{5.33}$$

The above equation shows the distributed nature of the cascaded SHG:DFG interactions and the interplay between the temporal walk-off effects. Equation (5.33) also shows that the effective SH pulse acquires a $(\delta\nu_{\mathrm{SH,T}} + \delta\nu_{\mathrm{P,SH}}/2)\frac{z}{2}$ time-shift during its propagation.

The cascaded interaction inherits most of its properties from the DFG interaction, as suggested by the striking similarity between Eqs. (5.25) and (5.31). The important

difference concerns the effective DFG pump pulses as given by Eqs. (5.26) and (5.32). The effective pump pulse for the simple DFG interaction is the filtered input pump, whereas for the SHG:DFG cascaded interaction, it is the filtered autoconvolution of the pump pulse. For a comparison of the DFG and cascaded SHG:DFG filter functions, we have plotted in Fig. 5.9 the modulus-squared of the closed form of the transfer functions obtained by direct integration of Eqs. (5.27) and (5.33). It can be easily seen that $|G_{\mathrm{C}}(\Omega)|^2$ is broader than $|G_{\mathrm{DFG}}(\Omega)|^2$, and thus the effective SH pump pulse [Eq. (5.32)] is always narrower than the effective pump for the simple DFG [Eq. (5.26)]. Furthermore, since $D_{\mathrm{SHG}}(\Omega) \approx G_{\mathrm{DFG}}(\Omega)$, the effective SH pulse can be expected to be narrower than the SH pulse itself but still broader than the original pump pulse. Even so, the output pulse [Eq. (5.31)] is not broadened significantly owing to its small group velocity difference with the input signal pulse. This feature is at the origin of the robustness of the SHG:DFG FROG scheme, with respect to walk-off effects, that is to be discussed in the following chapter. In addition, the broadening of the effective SH pulse helps in extending the distance over which its nonlinear mixing with the test pulse can still efficiently take place.

5.5.2 Numerical Simulations

We again supplemented the frequency-domain treatment with numerical simulations based on the following full coupled-mode equations for the simultaneous SHG and DFG interactions in the time domain:

$$\begin{aligned}
\frac{\partial A_{\mathrm{P}}}{\partial z} + \frac{1}{u_{\mathrm{P}}}\frac{\partial A_{\mathrm{P}}}{\partial t} + i\frac{\beta_{\mathrm{P}}}{2}\frac{\partial^2 A_{\mathrm{P}}}{\partial t^2} &= i\omega_{\mathrm{P}}\kappa_{\mathrm{SHG}} A_{\mathrm{P}}^* A_{\mathrm{SH}} \exp\left[-i\Delta\beta_{\mathrm{SHG}}^{(0)} z\right], \\
\frac{\partial A_{\mathrm{SH}}}{\partial z} + \frac{1}{u_{\mathrm{SH}}}\frac{\partial A_{\mathrm{SH}}}{\partial t} + i\frac{\beta_{\mathrm{SH}}}{2}\frac{\partial^2 A_{\mathrm{SH}}}{\partial t^2} &= -i\omega_{\mathrm{SH}}\kappa_{\mathrm{SHG}} A_{\mathrm{P}}^2 \exp\left[-i\Delta\beta_{\mathrm{SHG}}^{(0)} z\right] \\
&\quad + i\omega_{\mathrm{SH}}\kappa_{\mathrm{DFG}} A_{\mathrm{P}} A_{\mathrm{T}} \exp\left[-i\Delta\beta_{\mathrm{DFG}}^{(0)} z\right], \qquad (5.34) \\
\frac{\partial A_{\mathrm{T}}}{\partial z} + \frac{1}{u_{\mathrm{T}}}\frac{\partial A_{\mathrm{T}}}{\partial t} + i\frac{\beta_{\mathrm{T}}}{2}\frac{\partial^2 A_{\mathrm{T}}}{\partial t^2} &= i\omega_{\mathrm{T}}\kappa_{\mathrm{DFG}} A_{\mathrm{O}}^* A_{\mathrm{SH}} \exp\left[-i\Delta\beta_{\mathrm{DFG}}^{(0)} z\right], \\
\frac{\partial A_{\mathrm{O}}}{\partial z} + \frac{1}{u_{\mathrm{O}}}\frac{\partial A_{\mathrm{O}}}{\partial t} + i\frac{\beta_{\mathrm{O}}}{2}\frac{\partial^2 A_{\mathrm{O}}}{\partial t^2} &= i\omega_{\mathrm{O}}\kappa_{\mathrm{DFG}} A_{\mathrm{T}}^* A_{\mathrm{SH}} \exp\left[-i\Delta\beta_{\mathrm{DFG}}^{(0)} z\right].
\end{aligned}$$

Solving the above set of coupled-mode equations as before yields Fig. 5.10, which shows the propagation of the four pulses (T, P, SH, O) involved in the cascaded SHG:DFG interactions. The propagation lengths have been normalised to the walk-off length, defined as $L_w = \frac{\tau_{\mathrm{P}}}{|\delta\nu_{\mathrm{SH,T}}|}$. Note that $|\delta\nu_{\mathrm{SH,T}}| \approx |\delta\nu_{\mathrm{SH,O}}| \approx |\delta\nu_{\mathrm{SH,P}}|$. The wavelengths

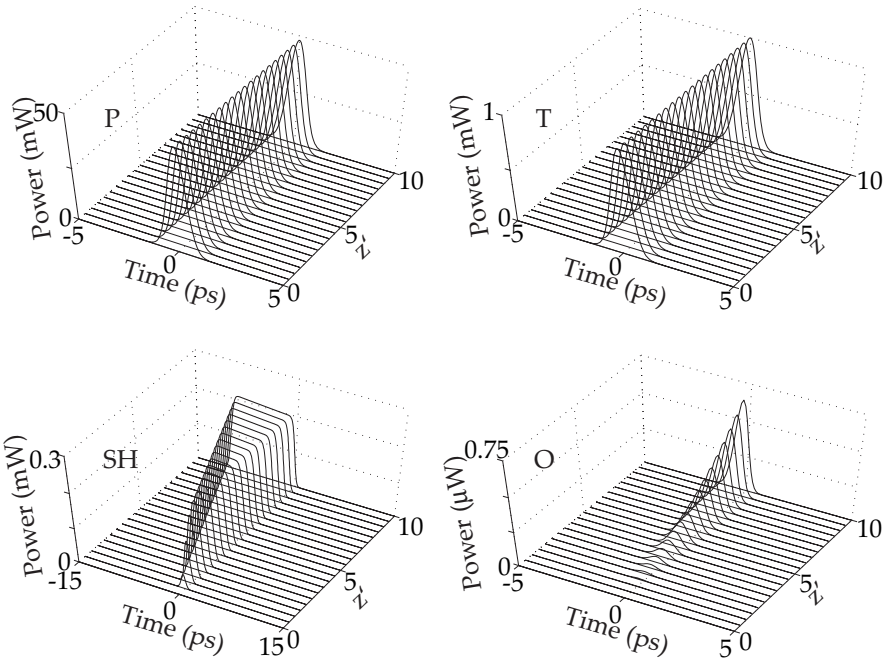

(a)

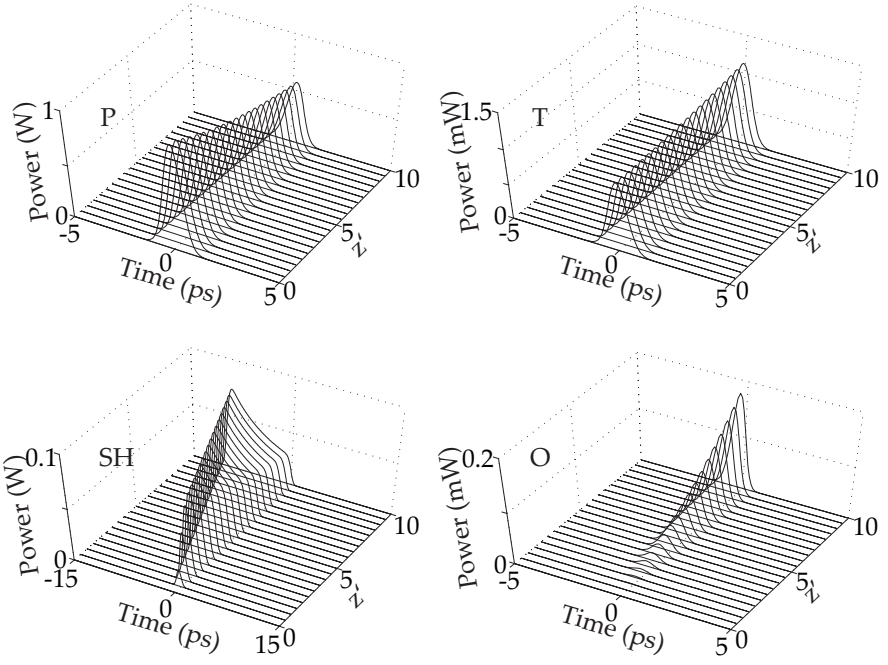

(b)

Figure 5.10: Results of numerical simulations for ultrashort pulse cascaded SHG:DFG. The figure shows the propagation of the pump (P), test (T), SH of pump (SH) and output (O) pulses. The input T and P pulses are transform-limited Gaussians of widths 1 ps. The T pulse has a peak power of 1 mW, whereas the P pulse has a peak power of a) 50 mW, or b) 1 W. The device had a normalised efficiency of $\eta_{\text{nor}} \approx 75\%[\text{W cm}^2]^{-1}$. The wavelength of the input T and P pulses are $\lambda_{\text{T}} = 1.536\,\mu$m and $\lambda_{\text{P}} = 1.540\,\mu$m, respectively. The QPM period was chosen such that the SHG interaction is phase-matched, whereas the DFG interaction has negligible phase-mismatch.

of the input pulses, which meet the phase-matching condition for the QPM period $\Lambda = 18.44\,\mu$m used in Fig. 5.3, are $\lambda_T = 1.536\,\mu$m and $\lambda_P = 1.540\,\mu$m.

We have used TL Gaussian pulses of widths 1 ps for the input test and pump pulses. The test pulse peak power is 1 mW, whereas the pump pulse peak powers are 50 mW and 1 W, which correspond to Figs. 5.10(a) and 5.10(b), respectively. The power level used in Fig. 5.10(a) would correspond to negligible pump depletion and negligible signal amplification, and thus the results of the numerical simulations can be directly compared with the frequency-domain analysis. Although the SH pulse is broadened in the interaction (see section 5.2), the output pulse is not. The broad SH pulse, which acts as the pump for the DFG process, guarantees its overlap with the input signal pulses, such that the DFG process does not cease to happen and the output pulse keeps growing. In contrast to the CW cascaded SHG:DFG scheme, whose overall efficiency can only be less than or equal to the efficiency of the simple DFG interaction, the ultrashort pulse cascaded SHG:DFG interaction can be more efficient than the simple DFG interaction in long devices.

The power level used in Fig. 5.10(b), on the other hand, causes the depletion of the pump pulse and the distortion of the SH pulse. It can also be seen that the signal pulse experiences small gain, and the output converted pulse in this case reaches much higher peak powers. Nevertheless, no significant distortion compared to the case of undepleted pump [Fig. 5.10(a)] can be observed.

5.6 Summary

The theoretical analyses and numerical simulations for the ultrashort pulse parametric interactions have been presented in this chapter. The frequency-domain analysis on the ultrashort pulse SHG[8] was extended to SFG and DFG single-step $\chi^{(2)}$ interactions, as well as to the cascaded SHG:DFG interaction. The devices chromatic dispersion significantly affects these ultrashort pulse parametric interactions, and manifests itself in the temporal walk-off effect. Figure 5.11, showing the width of the generated output pulses, summarises the implications of temporal walk-off effect on the ultrashort pulse parametric interactions considered in this chapter. For SHG and SFG, which are very similar, the temporal walk-off effect causes pulse broadening. For DFG, instead of broadening the output pulse, the temporal walk-off effect limits the conversion efficiency. The cascaded SHG:DFG inherits most of its properties from the DFG process, in the

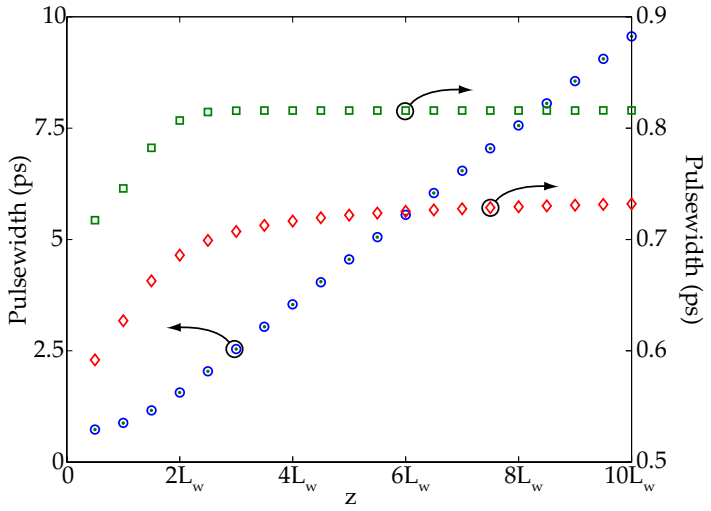

Figure 5.11: The generated output pulsewidths of the ultrashort pulse parametric interactions: SHG (blue circles), SFG (green dots), DFG (green squares), and cascaded SHG:DFG (red diamonds), as a function of the normalised propagation length.

sense that the temporal walk-off effect does not broaden the output pulse. Nevertheless, its conversion efficiency is not limited by the temporal walk-off effect.

References

[1] S. A. Akhmanov, A. S. Chirkin, K. N. Drabovich, A. I. Kovrigin, R. V. Khokhlov, and A. P. Sukhorukov, "Nonstationary Nonlinear Optical Effects and Ultrashort Light Pulse Formation," IEEE Journal of Quantum Electronics **QE-4**(10), 598–605 (1968).

[2] W. H. Glenn, "Second-Harmonic Generation by Picosecond Optical Pulses," IEEE Journal of Quantum Electronics **QE-5**(6), 284–290 (1969).

[3] A. M. Weiner, "Effect of Group Velocity Mismatch on the Measurement of Ultrashort Optical Pulses Via Second Harmonic Generation," IEEE Journal of Quantum Electronics **QE-19**(8), 1276–1283 (1983).

[4] E. Sidick, A. Knoesen, and A. Dienes, "Ultrashort-Pulse Second-Harmonic Generation in Quasi-Phase-Matched Dispersive Media," Optics Letters **19**(4), 266–268 (1994).

[5] E. Sidick, A. Knoesen, and A. Dienes, "Ultrashort-Pulse Second-Harmonic Generation. I. Transform-Limited Fundamental Pulses," Journal of the Optical Society of America B **12**(9), 1704–1712 (1995).

[6] E. Sidick, A. Dienes, and A. Knoesen, "Ultrashort-Pulse Second-Harmonic Generation. II. Non-Transform-Limited Fundamental Pulses," Journal of the Optical Society of America **12**(9), 1713–1722 (1995).

[7] E. Sidick, A. Knoesen, and A. Dienes, "Ultrashort-Pulse Second-Harmonic Generation in Quasi-Phase-Matched Stuctures," Pure and Applied Optics **5**(5), 709–722 (1996).

[8] G. Imeshev, M. A. Arbore, M. M. Fejer, A. Galvanauskas, M. Fermann, and D. Harter, "Ultrashort-Pulse Second Harmonic Generation with Longitudinally Nonuniform Quasi-Phase-Matching Gratings: Pulse Compression and Shaping," Journal of the Optical Society of America B **17**(2), 304–318 (2000).

[9] J. Prawiharjo, K. Gallo, N. G. R. Broderick, and D. J. Richardson, "Frequency-Resolved Optical Gating in the 1.55 μm-Band Via Cascaded $\chi^{(2)}$ Processes," Journal of the Optical Society of America **22**(9), 1985–1993 (2005).

[10] D. H. Jundt, "Temperature-Dependent Sellmeier Equation for The Index of Refraction, n_e, in Congruent Lithium Niobate," Optics Letters **22**(20), 1553 (1997).

[11] G. P. Agrawal, *Nonlinear Fiber Optics*, 3rd ed. (Academic Press, San Diego, 2001).

[12] J. Huang, J. R. Kurz, C. Langrock, A. M. Schober, and M. M. Fejer, "Quasi-Group-Velocity Matching Using Integrated-Optic Structures," Optics Letters **29**(21), 2482–2484 (2004).

[13] M. H. Chou, I. Brener, M. M. Fejer, E. E. Chaban, and S. B. Christman, "1.5-μm-Band Wavelength Conversion Based on Cascaded Second-Order Nonlinearity in $LiNbO_3$ Waveguides," IEEE Photonics Technology Letters **11**(6), 653–655 (1999).

[14] K. Gallo and G. Assanto, "Analysis of Lithium Niobate All-Optical Wavelength Shifters for the Third Spectral Window," Journal of the Optical Society of America B **16**(5), 741–753 (1999).

Chapter 6

Blind-Frequency-Resolved Optical Gating in a $LiNbO_3$ Quasi-Phase-Matched Waveguide Device

In chapter 3, it was shown that guided-wave geometries provide an efficiency enhancement over bulk materials, due to the coexistence of tight confinement and long interaction lengths. This efficiency enhancement will definitely benefit the FROG technique, described in the Chapter 2, increasing its measurement sensitivity. The implementation of FROG in a guided-wave geometry is nontrivial, mainly because it imposes a collinear geometry to the $\chi^{(2)}$ nonlinear interaction. We learnt from Chapter 2 that the implementation of SHG FROG in a collinear geometry yields an interferometric term [Eq. (2.9)], making its experimental implementation very challenging. Nevertheless, ultrasensitive fringe-resolved autocorrelation measurements have been demonstrated recently in a QPM $LiNbO_3$ waveguide.[1] Although the interferometric terms can be avoided using the simpler type-II SHG interaction,[2] it requires the waveguide to support both TE and TM polarisations. XFROG or blind-FROG configurations can provide an alternative solution for the implementation of the FROG technique in a guided-wave geometry.

In this chapter, we report the first, to our knowledge, implementation of the FROG technique, i.e. a SFG blind-FROG configuration, in a QPM $LiNbO_3$ waveguide device.[3] The choice for SFG over DFG is because of practical considerations. Although conceptually DFG blind-FROG is less restricted by the temporal walk-off effect compared to SFG blind-FROG, as pointed out in the previous chapter, its implementation in a wave-

guide device is restricted by the complexity in selectively coupling a laser beam in the 700 nm-regime into the fundamental mode of our waveguide. In addition, pulse sources of picoseconds width in that wavelength regime are not available in our laboratory. This experiment was done with help from Dr. Benn C. Thomsen, Michael A. F. Roelëns, and Paulo J. Almeida.

6.1 Experiments

For the SFG blind-FROG configuration, we need two pulses of different wavelengths, namely the signal and the probe pulses, in the telecommunications band. These pulses will be launched into our waveguide to generate sum-frequency (SF) pulses with a wavelength near 760 nm. A spectrogram will be measured by recording the SF pulse spectrum as a function of a time-delay introduced between the input pulses. The spectrogram for SFG blind-FROG is given by Eq. (2.21):

$$\Gamma^{(\text{SFG Blind-FROG})}(\Omega,\tau) \propto \left| \int_{-\infty}^{\infty} A(t)G(t-\tau)\exp\left(-i\Omega t\right)dt \right|^2, \tag{6.1}$$

where $A(t)$ and $G(t)$ are the complex amplitudes of the signal and probe pulses, respectively.

The device used in this experiment is the one described in Chapter 4. Due to the finite phase-matching bandwidth of our device and the fabrication uncertainties, we first had to perform SFG measurements to determine a suitable pair of phase-matching wavelengths for our FROG experiments, as described in Subsection 4.5.3. At a temperature of $105\,^0$C, we achieved phase-matching for wavelengths of 1533.0 nm and 1546.5 nm. Both wavelengths are within the tuning ranges of two short pulse sources available within our laboratory (as described below). In addition, the acceptance bandwidth of the ultrashort pulse interaction in our sample had to be considered when choosing the sources pulsewidths. As pointed out in Section 5.2, the acceptance bandwidth of ultrashort pulse SHG and, equivalently, SFG is the same as that of the CW SHG tuning curve. Hence, the SHG phase-matching bandwidth of 0.75 nm, which corresponds to a frequency bandwidth of 94 GHz for a phase-matched wavelength of 1538.9 nm at $105\,^0$C, has to be able to accommodate the convolution of the two input pulses, so that the spectrogram is not corrupted by the transfer function [Eq. (5.20)]. If a relatively long pulse, whose narrow spectrum can be considered as a Dirac delta function, is chosen to be one of the input pulses, the other input pulse spectral bandwidth is determined by the

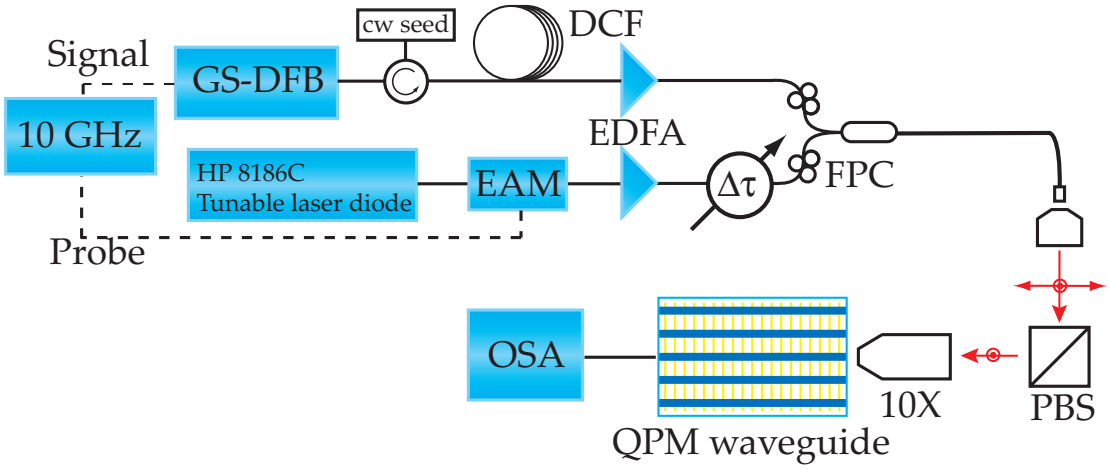

Figure 6.1: Schematic illustration of the SFG Blind-FROG experimental setup. Solid lines represent fibre links, whereas dashed lines are electronic connections.

acceptance bandwidth of the device.

A schematic of our SFG blind-FROG experimental setup is shown in Fig. 6.1. The signal pulses were generated by a gain-switched DFB laser diode (GS-DFB) operating at 1546.5 nm, whose output was linearly compressed with a length of dispersion compensation fibre (DCF). The spectral bandwidth of the GS-DFB laser was ~ 0.7 nm. A CW light seed was injected into the GS-DFB laser to reduce the timing jitter.[4] During our experiments we used three different lengths of DCF (95 m, 110 m, 125 m), whose GVD parameter is $b = +1.359 \times 10^{-19}\,\mathrm{s^2/m}$ at 1546.5 nm, in order to produce different pulse durations. Both probe and signal sources were driven at a repetition rate of 10 GHz from a common clock, thus ensuring synchronisation of the pulse trains.

The probe pulses were generated by external modulation of a tunable diode laser operating at 1533.0 nm using an electro-absorption modulator (EAM). The probe pulses were passed through a variable optical delay line fitted with a stepper motor, and were combined with the signal pulses via a 50:50 coupler. After amplification by EDFAs, both pulse trains had an average power of ~ 50 mW, corresponding to a pulse energy of ~ 5 pJ. The average power (energy) of both pulses at this point was reduced to ~ 22 mW (~ 2.2 pJ). The combined pulses were then coupled from the fiber into the PPLN waveguide using free-space optics. A bulk polariser was included within the setup to select the appropriate polarisation for the waveguide (TM in our case). The overall coupling efficiency into the waveguide was ~ -7 dB, limited mainly by mode-mismatch. The average launched power (energy) was ~ 4.3 mW (~ 430 fJ) for both input pulse

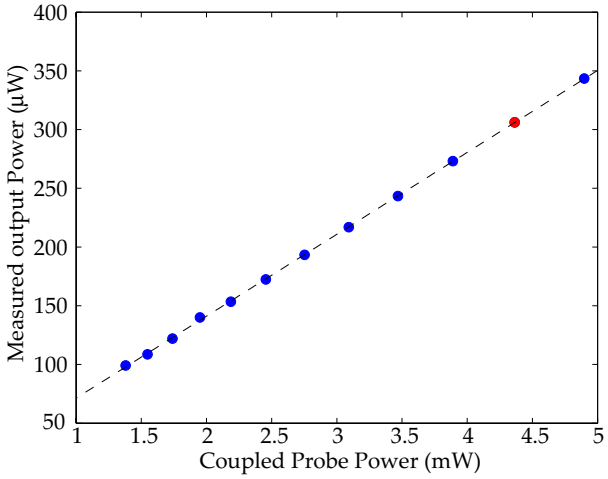

Figure 6.2: Output SF pulse power, after correcting for Fresnel reflection at the waveguide end-faces and microscope objective transmission, as a function of the coupled input probe pulse power. The red point shows our working point.

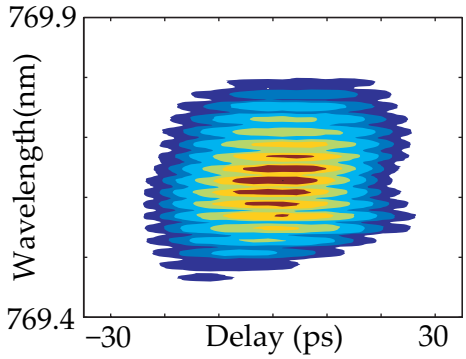

Figure 6.3: Typical measured spectrogram in SFG blind-FROG experiment. The frequency modulation is due to the 10 GHz repetition rate of the pulses.

trains.

Before taking the spectrograms, we had to check the validity of the linear relationship of Eq. (2.21). A 10× microscope objective was placed at the waveguide output to focus the SF pulse, which had a central wavelength of 769.7 nm, onto an InGaAs detector. Figure 6.2, showing the output of the SFG power as a function of the coupled input probe pulse power, confirms this essentially linear relationship. For our SFG blind-FROG experiment, a fibre was butt-coupled to the waveguide output to collect the SF pulses. At our working point, the average output SF power was $\sim 300\,\mu$W, about one-third of which was coupled into the collection fibre. The fibre was then connected to an "Advantest Q8384" optical spectrum analyser (OSA), operated at adaptive sweep mode without averaging, to record the spectrum of the SFG pulses.

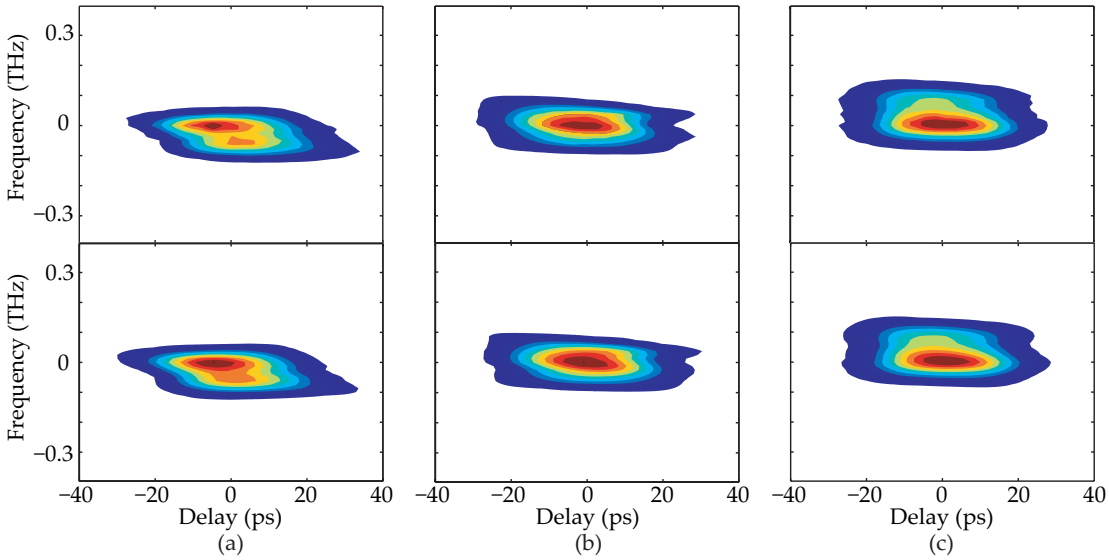

Figure 6.4: Interpolated (top) and retrieved (bottom) spectrograms for signal pulse compressed with (a) 95 m, (b) 110 m, and (c) 125 m long DCFs.

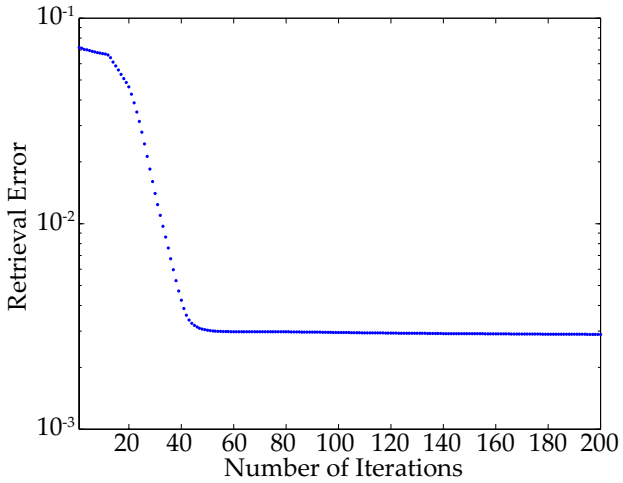

Figure 6.5: Typical FROG retrieval error [Eq. (2.24)] as a function of the number of iterations.

As the basis of the FROG technique, spectrogram measurements were performed by recording the spectrum of the generated SF pulses as a function of the time-delay between the input signal and probe pulses. Figure 6.3 shows a contour plot of the typical raw spectrogram data obtained in our experiments. The frequency modulation that appears in the spectrogram is due to the 10 GHz repetition rate of the pulses.

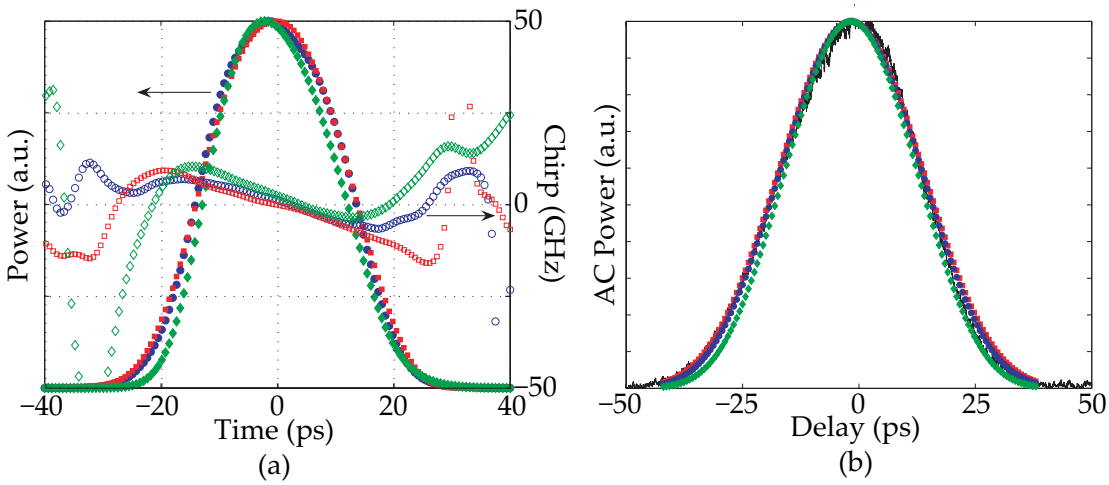

Figure 6.6: (a) Retrieved powers (solid markers, left ordinates) and chirps (empty markers, right ordinates) of the probe pulses. (b) Overlay of autocorrelation trace from a commercial device (solid line) and numerically generated autocorrelations of the retrieved probe pulses. The probe pulses in the figures were mixed with signal pulses compressed through 95 (green diamonds), 110 (red squares), and 125 m (blue circles) long DCFs.

6.2 Results and Discussions

Noise suppression of the measured spectrograms was achieved by background subtraction and low-pass filtering. They were then interpolated onto a Fourier grid with a temporal span equal to, or less than the pulse period before applying the retrieval algorithm described in Section 2.5. The top row of Fig. 6.4 shows a series of interpolated spectrograms for signal pulses compressed with the three different DCFs lengths. Although we did not impose a spectral constraint in the retrieval algorithm, no nontrivial ambiguities were observed. With a 128×128 spectrogram, the algorithm converged rapidly after 50-150 iterations to a FROG retrieval error [Eq. (2.24)] of less than 0.005 in all cases indicating good quality retrievals. Figure 6.5 shows the typical FROG retrieval error as a function of the number of iterations. The bottom row of Fig. 6.4 shows the retrieved spectrograms.

Figure 6.6(a) shows the retrieved intensities and chirps of the probe pulses. We found a reasonably consistent agreement between the retrieved probe pulses as we used the same probe pulse in all of our measurements. Slight discrepancies in the temporal shape among the retrieved pulses can be attributed to the sampling error induced by our particular motorised optical delay line, whereas the discrepancies in the chirp outside the main pulse arise from the retrieval uncertainty in the low intensities region. Additional comparison between the numerical autocorrelation of the retrieved probe pulses

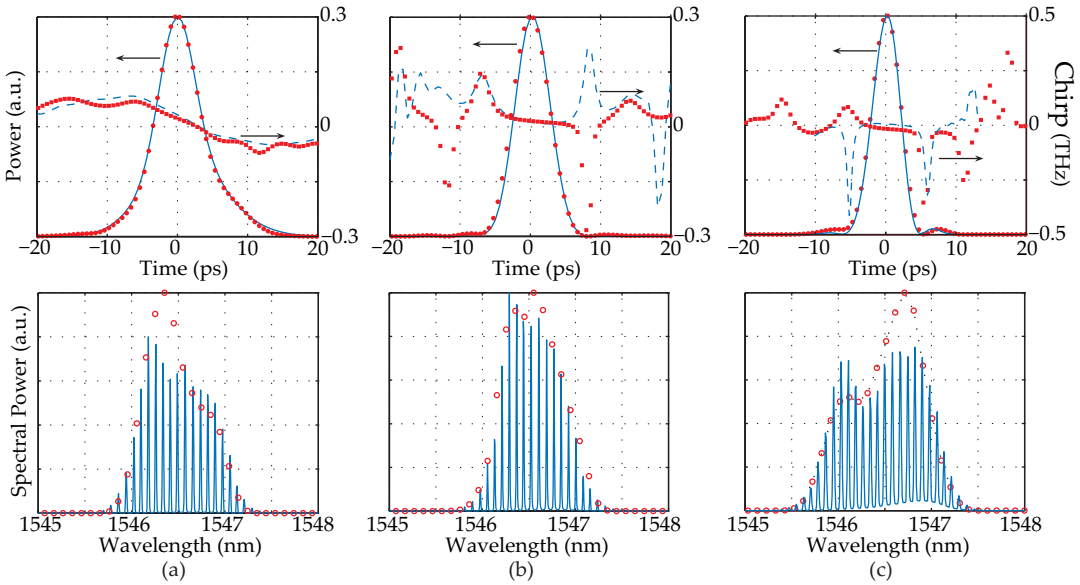

Figure 6.7: Top: Retrieved powers (red circles, left ordinates) and chirps (red squares, right ordinates) of the signal pulses compared with independent measurements made with a commercial SHG-FROG pulse analyser (blue lines). Bottom: Retrieved (red circles) and measured (blue lines) signal pulse spectra. The signal pulses were compressed with a) 95, b) 110, and c) 125 m long DCFs.

and their autocorrelation traces measured with a commercial autocorrelator, shown in Fig. 6.6(b), gave excellent agreement. In all cases, the width of the probe pulse is 25.5 ps. Finally, we note that the red-shift chirp (the frequency decreases with time across the pulse) observed in the retrieved probe pulse is known to be imposed by the EAM.[5]

The top row of Fig. 6.7 shows the retrieved powers and chirps of the signal pulses compressed with three different DCFs lengths. We compared the retrieved signal pulses with independent characterisations using a commercial SHG-FROG pulse analyser ("Southern Photonics"). Characterisations using the Southern Photonics device were done before the pulses were combined via a 50:50 coupler. The excellent agreement between them confirms the high reliability of our measurements in all cases. The measured width for the signal pulses compressed with 95, 110, and 125 m of DCFs are 7.5, 6.0, and 4.5 ps, respectively. Gain-switching in DFB lasers is known to cause a red-shifted chirp on the output pulse due to refractive index changes during optical pulse propagation,[6] and remains of this can be seen as the signal pulse was compressed with 95 m of DCF, suggesting the possibility of further compression using a longer DCF. Indeed, the amount of this red-shift chirp decreased when the signal pulse was compressed with 110 and 125 m long DCFs. The satellite pulses are evidence of residual nonlinear chirp

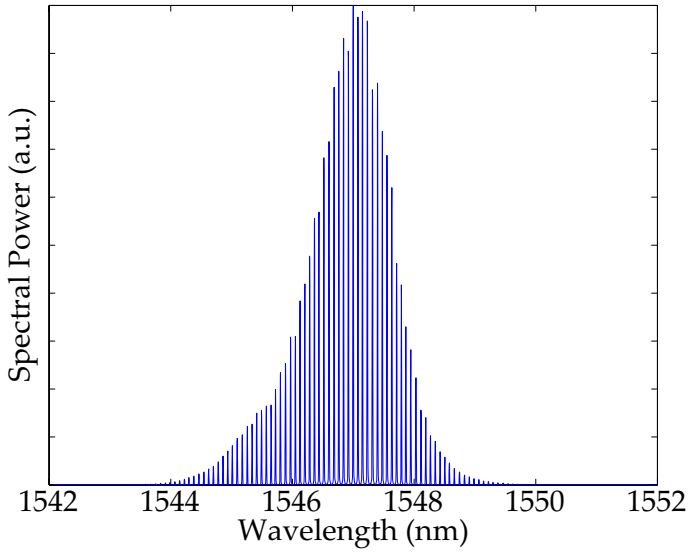

Figure 6.8: Mode-locked fibre laser (Pritel) spectrum.

on the edges of the GS-DFB pulse.[6]

Comparisons between the retrieved spectra of the signal pulses and direct measurements of the spectral envelopes taken from the OSA [bottom row of Fig. 6.7] yield good agreement. The fringes in the measured spectra are associated with the 10 GHz repetition rate of the pulse train. Since the retrieved spectra correspond to a single pulse, such fringes do not exist. Note also that the spectral shape is different for each compression fiber length due to the fact that we adjusted the GS-DFB laser drive and injection seeding conditions to minimise the pulse duration in each instance.

For the results in this experiment, the peak power of the coupled probe pulse is evaluated to be ~ 14 mW, whereas the peak powers of the coupled signal pulses compressed with 95, 110, and 125 m of DCF are ~ 54, 67, and 90 mW, respectively. These values correspond to a device sensitivity of $\sim 60\,\mathrm{mW}^2$. Reducing the input powers by a factor of 3 would still yield sufficient output power for a reasonable measurement, leading to an estimated device sensitivity of better than $\sim 6.7\,\mathrm{mW}^2$. It is worth noting that characterisations of both signal and probe pulses after the combining 50:50 coupler using the commercial SHG-FROG device were not possible due to the limited device sensitivity. In addition, the limited resolution of the commercial SHG-FROG device spectrometer made it difficult to obtain a reliable spectrogram.

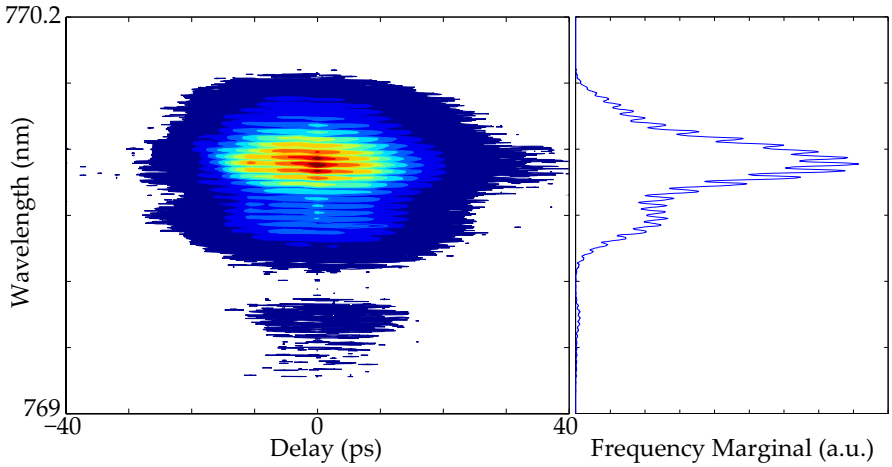

Figure 6.9: Measured spectrogram of mode-locked fibre laser signal pulse (left) and its frequency marginal (right).

6.3 Limitations

In our experiments, the spectral bandwidth of the GS-DFB laser was at the limit of the acceptance bandwidth of our device. We attempted to characterise signal pulses of shorter duration to observe the onset of temporal walk-off effects. In place of the GS-DFB laser, a mode-locked fibre laser (ML-FL), which operated at 1546.5 nm and had a duration of ~ 2 ps, was used. Its spectrum, shown in Fig. 6.8, had a full-width at half-maximum (FWHM) spectral bandwidth of ~ 1.5 nm. The ML-FL was amplified by an EDFA, resulting in an average power of ~ 9 mW after the combining 50:50 coupler.

As in the previous experiments, we measured the spectrogram by recording the SF pulse spectrum as a function of the time-delay between the input pulses. Figure 6.9 shows the measured spectrogram and its frequency marginal. Since the probe pulse spectrum can be considered a Dirac delta function, one expects the frequency marginal, which is the convolution of the input spectra [Eq. (2.17)], to be that of ML-FL spectrum (Fig. 6.8). However, Figure 6.9 clearly shows that the measured frequency marginal is not the expected one, confirming the presence of a filtering action by the device. The side-lobe in the shorter wavelength regime clearly shows the effect of a sinc-type transfer function [Eq. (5.14)] due to the temporal walk-off effect. We could not force the agreement between the measured and expected marginals, because there exist zero values in the spectral band of interests.

6.4 Summary

In conclusion, we have demonstrated the implementation of SFG blind-FROG in a QPM waveguide device. High quality simultaneous retrievals for short pulses of $\sim 4-7\,\mathrm{ps}$ durations and relatively long pulses of $\sim 25\,\mathrm{ps}$ durations with a coupled average power (energy) of 4.3 mW (430 fJ) were achieved. Such pulses could not be characterised by a commercial pulse analyser. The efficiency enhancement provided by the guided-wave geometry has been clearly demonstrated. The temporal resolution of the FROG technique, which is determined by the acceptance bandwidth of the device, limits the durations of pulses that can be characterised. This trade-off between the acceptance bandwidth and the efficiency (see Chapter 3) implies that the use of a shorter device may enable the characterisation of shorter duration pulses at the expense of lower efficiency. QPM engineering[7,8] can be used broaden the acceptance bandwidth, and thus increase the temporal resolution. However, the complexities in its design and fabrication are significant. Imperfect QPM engineering may yield a distorted transfer function, making a frequency marginal correction to the acquired spectrogram necessary.[8] In the next chapter, we shall present the analyses and the experimental demonstration of a novel FROG configuration based on cascaded $\chi^{(2)}:\chi^{(2)}$ interactions that provides a simple and elegant solution to this problem.

References

[1] S. D. Yang, A. M. Weiner, K. R. Parameswaran, and M. M. Fejer, "400-Photon-per-Pulse Ultrashort Pulse Autocorrelation Measurement with Aperiodically Poled Lithium Niobate Waveguides at 1.55 μm," Optics Letters **29**(17), 2070–2072 (2004).

[2] D. N. Fittinghoff, J. A. Squier, C. P. J. Barty, J. N. Sweetser, R. Trebino, and M. Müller, "Collinear Type II Second-Harmonic-Generation Frequency-Resolved Optical Gating for Use with High-Numerical-Aperture Objectives," Optics Letters **23**(13), 1046–1048 (1998).

[3] J. Prawiharjo, K. Gallo, B. C. Thomsen, M. A. F. Roelens, P. J. Almeida, N. G. R. Broderick, and D. J. Richardson, "Frequency Resolved Optical Gating in a Quasi-Phase-Matched $LiNbO_3$," IEEE Photonics Technology Letters **17**(4), 849–851 (2005).

[4] P. Gunning, J. K. Lucek, D. G. Moodie, K. Smith, R. P. Davey, S. V. Chernikov, M. J. Guy, J. R. Taylor, and A. S. Siddiqui, "Gainswitched DFB Laser Diode Pulse Source Using Continuous Wave Light Injection for Jitter Suppression and an Electroabsorption Modulator for Pedestal Suppression," Electronics Letters **32**(11), 1010–1011 (1996).

[5] D. G. Moodie, A. D. Ellis, and C. W. Ford, "Generation of 6.3 ps Optical Pulses at a 10 GHz Repetition Rate Using a Packaged Electroabsorption Modulator and Dispersion Compensating Fibre," Electronics Letters **30**(20), 1700–1701 (1994).

[6] P. Andersson and T. Andersson, "Chirp in Picosecond Pulses from Diode Lasers: Dependence on The Modulation Conditions and the Linewidth Enhancement Factor," IEEE Journal of Lightwave Technology **LT-4**(7), 795–798 (1986).

[7] G. Imeshev, M. A. Arbore, M. M. Fejer, A. Galvanauskas, M. Fermann, and D. Harter, "Ultrashort-Pulse Second Harmonic Generation with Longitudinally Nonuniform Quasi-Phase-Matching Gratings: Pulse Compression and Shaping," Journal of The Optical Society of America B **17**(2), 304–318 (2000).

[8] S. D. Yang, A. M. Weiner, K. R. Parameswaran, and M. M. Fejer, "Ultra-Sensitive Second-Harmonic Generation Frequency-Resolved Optical Gating by Aperiodically Poled $LiNbO_3$ Waveguides at 1.5 μm," Optics Letters **30**(16), 2164–2166 (2005).

Chapter 7

Cascaded $\chi^{(2)}$ Frequency-Resolved Optical Gating

The use of a waveguide device in a FROG configuration has been shown, in the previous chapter, to provide efficiency enhancement over bulk materials. However, as the interaction length is increased to gain further efficiency enhancement, the acceptance bandwidth decreases, thus limiting the temporal resolution. Therefore, there is a need to establish a trade-off between sensitivity and temporal resolution. It was mentioned before that engineering of the QPM structure[1–3] could be used to broaden the acceptance bandwidth without much sacrifice of the efficiency, providing a mean to improve this trade-off. However, the design and fabrication complexities involved are significant. Specifically, imperfect QPM engineering may result in a distorted transfer function, making necessary a frequency marginal correction to the acquired spectrogram.[3] Hence, there is a great interest in finding alternative solutions to this problem.

In this chapter, we propose, analyse, and experimentally demonstrate a novel FROG configuration based on cascaded $\chi^{(2)}$ interactions in a periodically-poled $LiNbO_3$ waveguide.[4,5] We will first describe the proposed configuration in Section 7.1, and then in Section 7.2, theoretically and numerically analyse it based on the ultrashort pulse cascaded SHG:DFG interaction studies in Section 5.5. Finally, in Section 7.3, a report on the experimental demonstration of the proposed configuration will be presented. The experiment were done with help from Francesca Parmigiani and Dr. Periklis Petropoulos.

7.1 Configuration Descriptions

The cascaded $\chi^{(2)}$ SHG:DFG FROG configuration we propose mimics a frequency non-degenerate four-wave-mixing process, in a QPM waveguide. This differs from the cascading configuration of Ref. 6, where SHG and degenerate down-conversion were used to mimic $\chi^{(3)}$ self-diffraction or polarisation-gate FROG configurations. In fact, the latter scheme is based on noncollinear interactions and could not be implemented in a channel waveguide nor in long devices.

The cascaded SHG:DFG interactions had been previously described in Section 5.5. A FROG configuration can be readily constructed based on these interactions, by introducing a time-delay between the test and the pump pulses at the input and recording the spectrum of the output pulse. Without *a priori* knowledge of the input pulses, a complete characterisation about the test pulse is still possible by using the retrieval algorithm described in Section 2.5. On the other hand, the gate pulse simultaneously retrieved in this way does not directly correspond to any measurable quantity (not the pump nor its second harmonic, strictly speaking), but it rather reflects the distributed nature of the cascaded SHG:DFG process.

7.2 Theoretical Considerations

The discussions on XFROG and blind-FROG configurations in Section 2.4 revealed that a DFG based configuration has a better temporal resolution compared to the SFG based one. The spectral filter function in SFG XFROG corrupts the information of the test pulse, especially for interaction lengths greater than the walk-off length [Eq. (5.14)]. On the contrary, the information of the test pulse in the DFG XFROG case is not corrupted by such a filter function [Eq. (5.25)]. The spectrogram of DFG XFROG/blind-FROG with a gate pulse at a higher frequency, taken from Eq. (2.21), is given by:

$$\Gamma^{(\text{DFG blind-FROG})}(\Omega,\tau) \propto \left| \int_{-\infty}^{\infty} A^*(t) G(t-\tau) \exp\left(-i\Omega t\right) dt \right|^2 . \tag{7.1}$$

As discussed in Section 2.4, $G(t)$ is not the input reference pulse, but it is filtered by the DFG transfer function [Eq. (5.27)].

In the cascaded SHG:DFG FROG configuration, the reference pulse is replaced by a pump pulse whose SH (generated inside the $\chi^{(2)}$ medium) gates the test pulse (See Fig. 5.8). The spectrogram is still given by Eq. (7.1), but with the gate pulse

being $\hat{A}'_{\mathrm{SH}}$ [Eq. (5.32)], the effective SH of the input pump pulse. When temporal walk-off effects are negligible, the gate pulse simply reduces to the square of the pump pulse, i.e. $G(t) = A_{\mathrm{P}}^2(t)$. Similar to the case of DFG XFROG, the output pulse in the SHG:DFG XFROG does not suffer from the spectral filter function, and thus high-quality retrieval of the test pulse can be guaranteed even for a device of several walk-off lengths. Therefore, the cascading scheme appears to be extremely well-suited for measuring picosecond or even subpicosecond signals in a few centimetre-long $LiNbO_3$ waveguide.

In principle, with negligible pump depletion, the gate pulse $G(t)$ could be obtained by fully characterising the pump pulse and then applying Eq. (5.33). However, this would require the exact knowledge of the transfer function $G_{\mathrm{C}}(\Omega)$, which is very difficult to determine precisely in practice. The blind-deconvolution algorithm (Section 2.5) provides a solution to this problem, as it can retrieve both the test and the gate pulses without any additional characterisation of the pump pulse, or of the $\chi^{(2)}$ device.

In order to evaluate the performance of the $\chi^{(2)} : \chi^{(2)}$ SHG:DFG blind-FROG technique we simulated the device via Eqs. (5.34) with two pulses at the input: the pump pulse at ω_{P} and the test pulse at ω_{T}. We then introduced a variable time-delay between the input pulses and finally obtained the spectrograms for the numerical FROG experiment by calculating the spectra of the output pulses around ω_{O} for each time-delay. The spectrogram can be easily interpolated onto a Fourier grid, and then fed into the retrieval algorithm, to retrieve the powers and the phases of both input pulses.

Figure 7.1 shows several examples of spectrograms generated in the numerical experiments. In all cases, a 1 ps-wide transform-limited (TL) Gaussian pulse with 50 mW peak power was used as the pump. The test pulses were: a) a TL Gaussian, b) a linearly-chirped Gaussian, c) a Gaussian with cubic spectral phase, and d) a Gaussian pulse with the typical chirp induced by self-phase-modulation (SPM) in a $\chi^{(3)}$ medium (such as a fibre link). The width of the first, second and last test pulses was $\delta t_{\mathrm{T}} = 1\,\mathrm{ps}$, whereas the third test pulse had a spectral bandwidth of $\delta f = 1\,\mathrm{THz}$. The device length was chosen to be $5L_w$, which would correspond to $\sim 1.6\,\mathrm{cm}$ in $LiNbO_3$. The intensity (left-hand ordinates) and chirp (right-hand ordinates) of the signal pulses retrieved by the blind-deconvolution algorithm from the spectrograms are overlayed with the input test pulses of the numerical FROG experiments in the bottom plots of Fig. 7.1. Despite the device length exceeding several walk-off lengths, the retrieval of the test pulses is

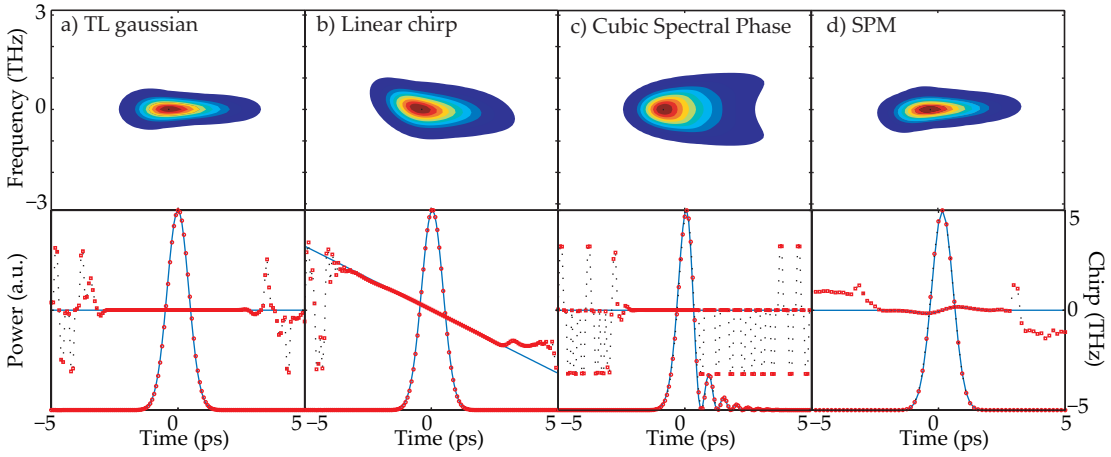

Figure 7.1: Top row: Generated spectrograms. Bottom row: The retrieved powers (red circles) and chirps (red squares) of the test pulses overlayed with the input for the simulations (blue lines). Various test pulses were used: a) a TL Gaussian, b) a linearly-chirped Gaussian, c) a Gaussian with cubic spectral phase, and d) a self-phase-modulated Gaussian pulse. We used a peak power of 1 mW for all of the test pulses, a 1 ps Gaussian pulse with a 50 mW peak power for the pump pulse. The device has a length of $5L_w$ with a normalised efficiency of $\eta_{\text{nor}} = 70\%[\text{W cm}^2]^{-1}$. The SHG interaction was exactly phase-matched, whereas the DFG interaction had a negligible phase-mismatch.

excellent.

It is interesting to compare the gate pulses retrieved by the blind-deconvolution algorithm from the numerically generated spectrograms with the calculations based on Eq. 5.32. Figure 7.2 shows the spectrograms corresponding to the input conditions of Fig. 7.1(a) at three different normalised propagation lengths. The bottom plots show the retrieved gate pulses (circles) together with the effective SH pulse calculated from Eq. 5.32 (solid lines). It can be easily observed that the retrieved gate pulses match perfectly the effective SH pulses. The integration over z in Eq. (5.33) yields a skewed effective SH pulse which results in a smeared spectrogram. Figure 7.3 shows the width of the retrieved gate pulse in Fig. 7.2 together with the width of the SH pulse. The gate pulse is narrower than the SH pulse, in accordance with the frequency-domain analysis in Section 5.5.

The retrieved gate pulse can be considered as a by-product of the characterisation. Unfortunately, no information about the input pump pulse can be extracted from it without exact knowledge of the transfer function $G_C(\Omega)$ [Eq. (5.33)]. The frequency-domain treatment [Eqs. (5.31) and (5.32)] shows that the output pulse is only related to the convolution of the test and the gate pulses, and thus the choice of the pump pulse $A(t)$ does not affect the test pulse retrieval quality, provided the pump wavelength meets

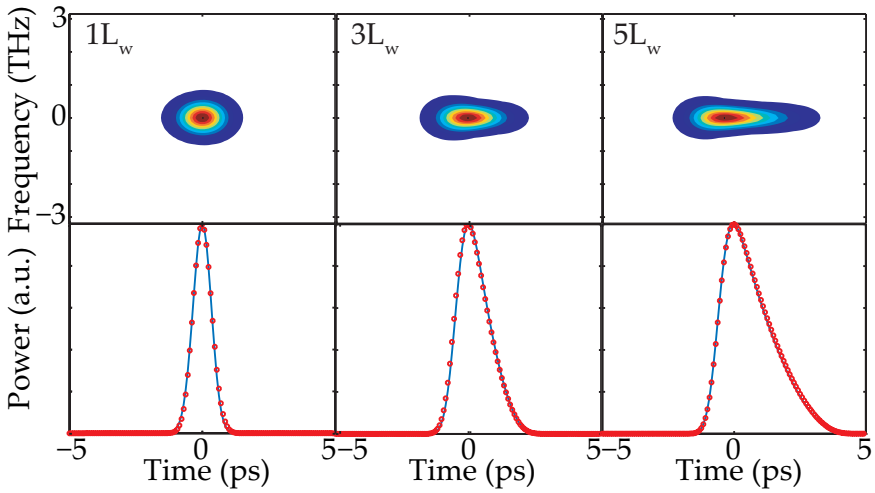

Figure 7.2: The spectrograms of TL Gaussian test and pump pulses at different normalised propagation lengths (top row) and their retrieved gate pulses (red circles) overlayed with the effective SH pulses (blue lines), calculated from Eq. 5.32. The input conditions are the same as in Fig. 7.1(a)

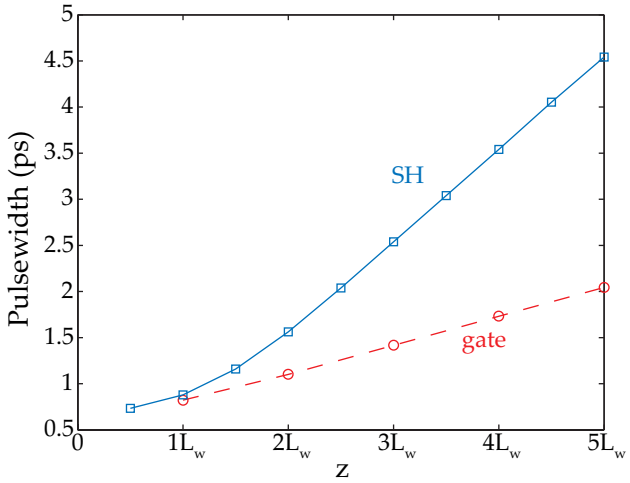

Figure 7.3: The widths of the retrieved gate pulse (circles - dashed line) and of the SH pulse (squares - solid line) as a function of the propagation length, for the case considered in Fig. 7.2.

the QPM condition for SHG ($\Delta\beta_{\mathrm{SHG}}^{(\mathrm{QPM})} = 0$, see Section 4). Numerical simulations using different kinds of pump pulses, including highly chirped ones, confirmed this feature.

The cascaded XFROG inherits most of its features from the DFG interaction and, most notably, the output pulse does not experience a spectral filter function which can degrade the time resolution. This does not imply, however, that the characterisation of ultrashort pulses is not restricted by the device length. As the length increases, the width of the SH and the gate pulses also increase, limiting the FROG temporal resolution for two reasons. First, the resolution with which the input signal pulse can be retrieved from the spectrogram is determined by the width of the gate pulse, which should be able to sample all the significant phase variations of the test pulse in the time-frequency domain.[7] Secondly, the quality of the retrieved test pulses is limited by the Nyquist sampling criterion. The Nyquist sampling criterion specifies a minimum number of points required to correctly represent a specific function in a certain temporal span. Therefore, in a temporal span determined by the gate pulse which is sampled at a specific number of points, the test pulses that can be correctly represented are limited.

The Wigner representation Eq. (2.18) can be used to assess the retrieval quality of both intensity and phase of the test pulses with a single parameter.[8] The retrieval quality can then be assessed by calculating the Wigner trace error between the retrieved pulse and the input pulse of the numerical FROG experiments. The Wigner trace error is defined as follows:

$$\varepsilon_W = \sqrt{\frac{\sum_{\omega,\tau}[W_{\mathrm{input}}(\omega,\tau) - \alpha W_{\mathrm{test}}(\omega,\tau)]^2}{\sum_{\omega,\tau}[W_{\mathrm{input}}(\omega,\tau)]^2}}, \tag{7.2}$$

where α is a scaling factor chosen so as to minimise the Wigner trace error. The Wigner representation as a time-frequency distribution is more sensitive than a spectrogram, and the trace error is independent of the computational matrix size.

Numerical simulations for a 1 ps Gaussian test pulse with a strong self-phase modulation [4 times of that shown in case (d)] of Fig. 7.1) with the same parameters used in Fig. 7.1 showed an almost flat Wigner trace error of about $\varepsilon_W \sim 0.004$ over $10L_w$ propagation lengths. Increasing the propagation length any further is not computationally convenient, thence in order to further explore the retrieval error in SHG:DFG blind-FROG, we fixed the device length at $5L_w$ (for 1 ps pulsewidth) and decreased the test pulsewidth instead. Figure 7.4 shows the Wigner trace error ε_W for both a TL Gaussian and a SPM Gaussian test pulse as a function of the test pulsewidth. The plot

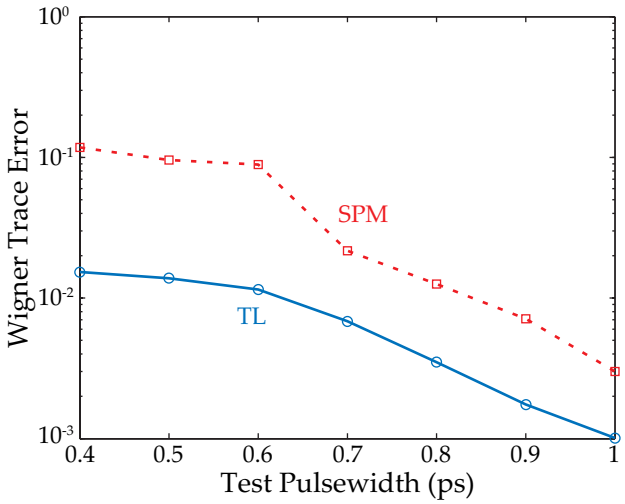

Figure 7.4: Wigner trace error as a function of pulsewidth for TL Gaussian (circles - solid line) and for self-phase-modulated Gaussian (squares - dashed line) test pulses.

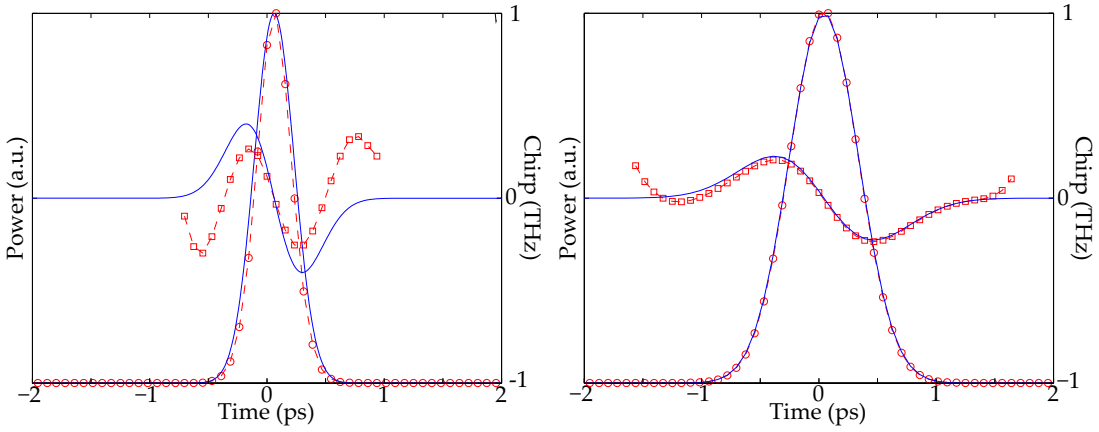

(a) 0.4 ps, $\varepsilon_W = 0.11$ (b) 0.7 ps, $\varepsilon_W = 0.01$

Figure 7.5: Comparisons of the intensities and chirps of retrieved test pulses (red markers) and the input pulse (blue markers) of different widths in the numerical simulations used to calculate the Wigner trace error in Fig. 7.4.

clearly shows a trend for the error to increase as the pulsewidth decreases in both cases (being higher for the SPM pulse case). According to our observations (see Fig. 7.5), a good quality pulse retrieval is described by a Wigner trace error of less than 0.05 (about half of the value used in Ref. 8). We can therefore conclude that by using a $5L_w$ long device, high-quality retrieval would still be possible for pulse durations down to 0.4 ps and 0.7 ps for the case of TL and SPM test pulses, respectively.

The frequency-domain treatment in Section 5.5 was developed under the assumption of negligible SHG pump depletion. Nevertheless, the fact that the pump pulse has little impact on the retrieval of the test pulse suggests that the cascaded FROG configuration could still work well even when the pump is depleted (and the gate is further distorted). Consistently, in our simulations we do not find any significant change in the Wigner trace error ($\varepsilon_W < 0.004$) of the retrieved test pulses when the pump peak power is varied by 3 orders of magnitude (from 50 mW to 50 W). The retrieved gate pulses, on the other hand, do not match the calculated effective SH pulse [Eq. (5.32)] as expected.

Currently available technologies allow the fabrication of several centimetres-long high-quality QPM waveguides. As an example for the implementation of our cascading FROG device, we can consider a 3.2 cm ($10L_w$) long device. This would be appropriate for the characterisation of a 1 ps test pulse with arbitrary chirp and a peak power of 1 mW. For a 1 ps pump pulse with a peak power of 5 W, an output pulse with a peak power of 2.8 mW is obtained, corresponding to an average power of 22 μW for the output pulse (assuming a 10 GHz repetition rate). As a comparison, using the same parameters and assuming an ideal coupling for the pump pulse, the DFG XFROG is less efficient due to temporal walk-off effects. The DFG interaction only yields an output pulse with a peak power of 0.4 mW, corresponding to an average power of 3 μW. The characterisation of the same test pulse using SFG XFROG could only be done using a $1L_w$ long device. In this case, an output pulse with a peak power of 0.7 mW, corresponding to an average power of 5.7 μW, would be obtained by using the same pump pulse as above. The above comparison is done for TL test and pump pulses. For chirped pulses, the device length for SFG XFROG would need to be shortened, thus the efficiency would be even lower.

Although the proposed cascading configuration can guarantee good efficiencies and better time resolutions than traditional single step XFROG techniques, a self-consistency check of the measured spectrograms is not possible in a real experiment (the self-consistency check is usually done by means of a frequency marginal Eq. (2.17), which

is the modulus-squared of Eq. (5.31)), due to the difficulties in the independent determination of the gate pulse.

We would also like to make a final remark on the retrieval procedure. It is well-known that the blind-FROG algorithm exhibits nontrivial ambiguities,[9,10] i.e. there might exist other pairs of pulses which yield a similar spectrogram. In order to solve this problem, additional constraints are normally employed, such as spectral constraints on both input pulses. The use of spectral constraints on both input pulses in the cascaded FROG configuration is not straightforward, as the spectrum of the gate pulse cannot be easily obtained. Nevertheless, recent investigations[10] show that a unique retrieval of the pulse pair is more likely for spectrograms that are not symmetric with respect to the delay τ. Figure 7.2 shows that the generated spectrogram of cascaded XFROG becomes more asymmetric as the propagation length increases. Indeed, in most cases, we obtained high quality retrievals (i.e. Wigner trace errors below threshold) without applying any spectral constraint. We had some difficulties in retrieving signal pulses with a linear chirp, but we could easily overcome them by applying the spectral constraint on the test pulse only. The use of a single spectral constraint on the test pulse did not make a significant change to the quality of the pulse retrieval in all the other cases, but it improved the convergence rate of the retrieval algorithm.

7.3 Experimental Realisations

The device used in this experiment is the one described in Chapter 4 and used in the previous chapter. In order to accommodate available sources in our laboratory, we had to shift the SHG phase-matching wavelength to 1541.9 nm by operating the waveguide device at a temperature of 121 ^{0}C. Figure 7.6 shows a schematic of our experimental setup. The output from a 10 GHz mode-locked fibre laser (ML-FL) operating at λ_P = 1541.9 nm was first gated down to 2.5 GHz by an electro-optics modulator (EOM), pre-amplified by an EDFA, and then split into two using a 90:10 coupler. The first path, which contains 10% of the power, was amplified by an EDFA to generate our pump pulse. An optical band-pass filter (BPF) with a 5 nm FWHM bandwidth was used to suppress the amplified spontaneous emission (ASE). A motorised variable optical delay line was included in this path. The remaining 90% of the pulse train was used to generate our test pulse. The pulse train was used as the control of a nonlinear optical loop mirror (NOLM) configuration, with the signal being a CW laser diode operating at λ_T = 1560 nm. The

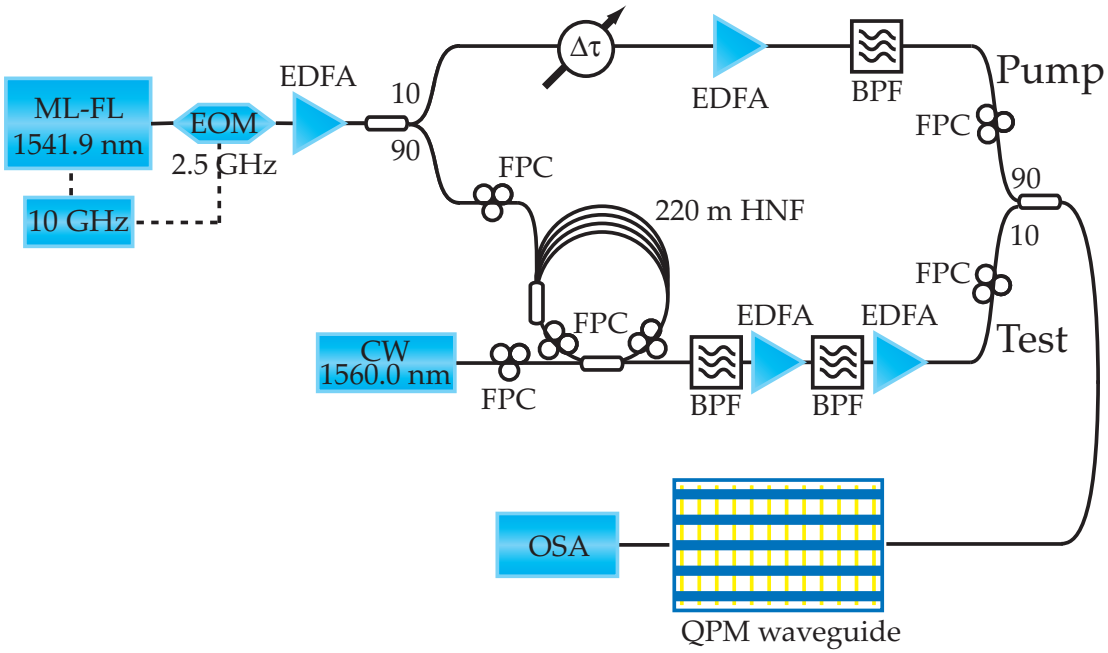

Figure 7.6: Schematic illustration of the cascaded SHG:DFG FROG experimental setup.

optical loop in the NOLM configuration was a 220 m highly-nonlinear fibre with a zero-dispersion-wavelength at 1550 nm and a GVD parameter of $b = -1.283 \times 10^{-23}\,\mathrm{s}^2/\mathrm{m}$ at 1555 nm. The control pulse of the NOLM was suppressed using two 3 nm FWHM optical bandpass filters arranged in a series, with an EDFA in between to preserve the integrity of the converted pulse train. Finally, another EDFA with a variable gain was placed after the last BPF. Since the NOLM configuration is polarisation sensitive, several fibre polarisation controllers (FPCs) were placed in appropriate places. Finally, 90% of the pump pulse and 10% of the test pulse were combined together, resulting in average powers (energies) of 100 mW (40 pJ) and $0.2 - 2$ mW ($80 - 800$ fJ), respectively, before being launched into the waveguide. Note that due to the polarisation sensitivity of the nonlinear interactions in the $LiNbO_3$ waveguides, the polarisations of the pump and test pulses were independently controlled by FPCs. The waveguide was fibre-coupled at both the input and the output, with a fibre-to-fibre throughput of ~ -11.5 dB, due to uncoated end-faces (~ -1.7 dB), intrinsic propagation loss (~ -2.6 dB), and fibre-waveguide mode mismatch (~ -7.2 dB). Therefore, the coupled average powers (energies) for pump and test pulses are 36 mW (15 pJ) and $72 - 720\,\mu$W ($29 - 290$ fJ), respectively.

The spectra at the output of the waveguides were measured by an "Advantest

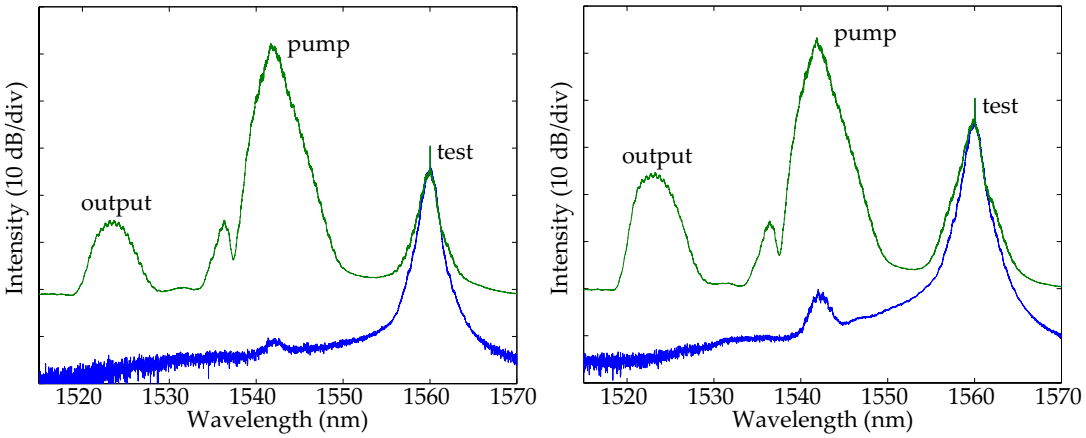

(a) 0.2 mW test pulse average power (b) 2 mW test pulse average power

Figure 7.7: Measured spectra at the output of the waveguide with (green lines) and without (blue lines) the presence of the pump pulse. With the presence of the pump pulse, the generated output pulse is shown at zero delay ($\tau = 0$).

Q8384" optical spectrum analyser (OSA), operated at normal sweep mode without averaging, and are shown in Fig. 7.7. This shows the spectra of the waveguide output with (green lines) and without (blue lines) the presence of the pump pulse, for test pulses with average powers of 0.2 and 2 mW. The presence of the pump pulse induces the cascaded SHG:DFG interaction, yielding the generated output pulse. There was no significant overlapping between the spectra of the test, the pump, and the generated output pulses. The narrow peak in the test pulse spectrum is a residual continuous-wave (CW) component from the NOLM, which has little contribution toward the nonlinear interactions, as no such component can be observed in the spectrum of the generated output pulse. We observed that the side-lobe structure on the shorter wavelength side in the pump pulse spectrum depends on its power and is an indication of SHG cascading self-phase modulation. Note that this does not affect the FROG measurement.

The internal conversion efficiency for both cases, defined as

$$\eta = \frac{U_{\mathrm{O}}}{U_{\mathrm{T}}} = \frac{\int_{-\infty}^{\infty} |A_{\mathrm{O}}(t)|^2 \, dt}{\int_{-\infty}^{\infty} |A_{\mathrm{T}}(t)|^2 \, dt}, \tag{7.3}$$

where $A_{\mathrm{T}}(t)$ and $A_{\mathrm{O}}(t)$ are the complex amplitude of the coupled test pulse and the generated output pulse, respectively, was estimated to be ~ -9 dB. We define the wavelength range of the output pulse between 1516 and 1533 nm, and the test pulse between 1554 and 1570 nm. The fact that the conversion efficiency is the same for both test pulse powers confirms the linearity of Eq. (7.1).

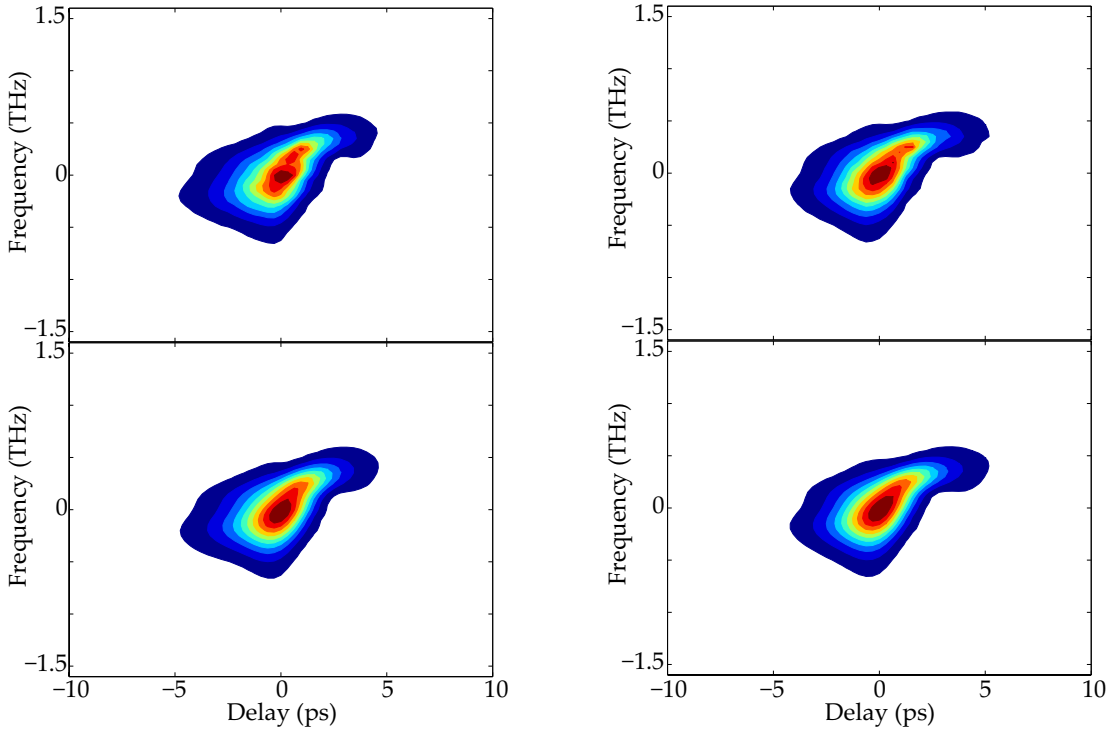

(a) 0.2 mW test pulse average power

(b) 2 mW test pulse average power

Figure 7.8: Measured (top) and retrieved (bottom) spectrograms for two different test pulse average powers.

The top row of Fig. 7.8 shows a measured spectrogram for test pulses of 0.2 and 2 mW average powers after an interpolation onto 64×64 Fourier grids. Noise suppression was achieved by background substraction only. Employment of the retrieval algorithm described in Section 2.5 to the interpolated spectrograms yielded the bottom row of Fig. 7.8. Although we did not impose a spectral constraint, no nontrivial ambiguities were observed. The algorithm converged rapidly after 50-150 iterations to a root-mean-square (rms) error of 0.009 and 0.006 for average powers of 0.2 and 2 mW, respectively, indicating a good quality retrieval.

Figure 7.9 shows the retrieved powers and chirps of the test pulses. The excellent agreement between the retrieved test pulses over a dynamic range of 10 dB ($0.2-2$ mW) can be easily observed. Independent measurements in the time and the spectral domains confirmed the high-quality pulse retrieval. Figure 7.10(a) shows the excellent agreement between the measured autocorrelation trace of the test pulses and the autocorrelation numerically generated from the retrieved test pulse temporal profiles. The independent autocorrelation measurements were done at the point before the recombining coupler.

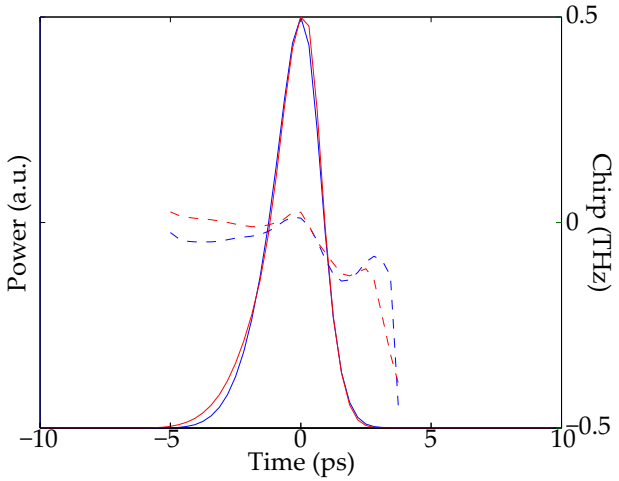

Figure 7.9: Retrieved powers and chirps of the test pulses of 0.2 mW (red) and 2 mW (blue) average powers.

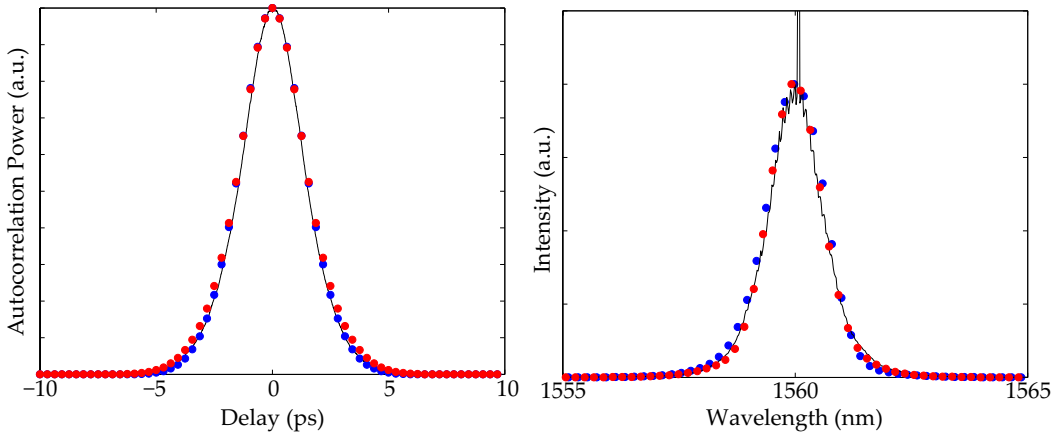

(a) (b)

Figure 7.10: a) Measured autocorrelation trace of the test pulse and numerically generated autocorrelation from the retrieved test pulse. b) Measured and retrieved spectrum of the test pulse. The retrieved test pulse had average powers of 0.2 mW (red) and 2 mW (blue).

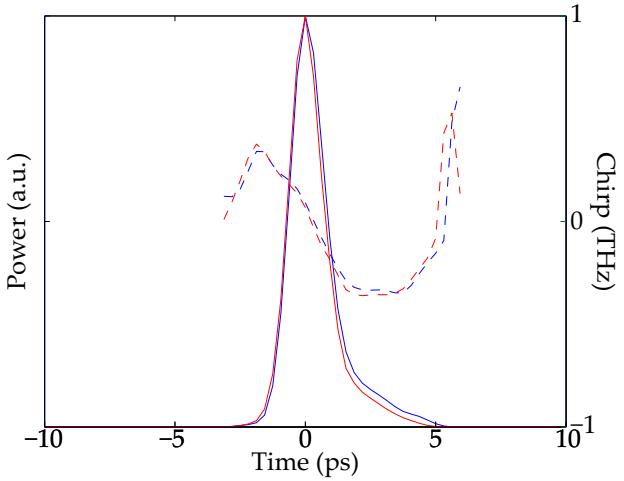

Figure 7.11: Retrieved powers and intensities of the gate pulses from the characterisation of test pulses of 0.2 mW (red) and 2 mW (blue) average powers.

Similarly, the measured and the retrieved spectra in Fig. 7.10(b) show an excellent agreement (over 30 dB range). The narrow peak in the measured test pulse spectrum is not present in the retrieved one, because the residual CW component hardly contributes toward the nonlinear interaction, as previously described. The temporal full-width at half-maximum (FWHM) of the retrieved pulse is 2.1 ps, whilst its spectral FWHM is 0.18 THz (1.5 nm), yielding a temporal-bandwidth product of 0.39. It is worth underlining that the acceptance bandwidth limitations of single-step $\chi^{(2)}$ FROG would have made it impossible to characterise test pulses down to these durations in the same device, as shown in the previous chapter.

It is also interesting to look at the retrieved gate pulse (Fig. 7.11). As it does not depend on the properties of the test pulse (see Section 7.2), once retrieved in one characterisation, it could be employed as a well-referenced pulse for characterisations of other pulses, just as it is normally done in XFROG configuration (Section 2.4). This could improve the speed of subsequent retrievals as well as provide self-consistency error checks via the frequency marginal.

7.4 Summary

The analysis of the cascaded SHG:DFG FROG configuration introduced in Section 5.5 revealed its superiority compared to SFG and DFG Blind-FROG. This theoretical prediction was experimentally verified by characterising a 2.1 ps pulse train with a coupled average power (energy) of 72 μW (29 fJ). Such pulses could not be characterised using

SFG blind-FROG as shown in the previous chapter due to the acceptance bandwidth limitations. The dramatic improvement in efficiency and temporal resolution of the cascaded scheme compared to single-step $\chi^{(2)}$ FROG configurations have been clearly shown. In principle, even the characterisations of subpicosecond pulses with arbitrary chirps would be possible this scheme.

References

[1] G. Imeshev, M. A. Arbore, M. M. Fejer, A. Galvanauskas, M. Fermann, and D. Harter, "Ultrashort-Pulse Second Harmonic Generation with Longitudinally Nonuniform Quasi-Phase-Matching Gratings: Pulse Compression and Shaping," Journal of The Optical Society of America B **17**(2), 304–318 (2000).

[2] S. D. Yang, A. M. Weiner, K. R. Parameswaran, and M. M. Fejer, "400-Photon-per-Pulse Ultrashort Pulse Autocorrelation Measurement with Aperiodically Poled Lithium Niobate Waveguides at 1.55 μm," Optics Letters **29**(17), 2070–2072 (2004).

[3] S. D. Yang, A. M. Weiner, K. R. Parameswaran, and M. M. Fejer, "Ultra-Sensitive Second-Harmonic Generation Frequency-Resolved Optical Gating by Aperiodically Poled $LiNbO_3$ Waveguides at 1.5 μm," Optics Letters **30**(16), 2164–2166 (2005).

[4] J. Prawiharjo, K. Gallo, N. G. R. Broderick, and D. J. Richardson, "Frequency-Resolved Optical Gating in the 1.55 μm-Band Via Cascaded $\chi^{(2)}$ Processes," Journal of the Optical Society of America B **22**(9), 1985–1993 (2005).

[5] J. Prawiharjo, F. Parmigiani, K. Gallo, P. Petropoulos, N. G. R. Broderick, and D. J. Richardson, "Cascaded $\chi^{(2)}$ Interaction Frequency-Resolved Optical Gating in a Periodically-Poled Lithium Niobate Waveguide," (2005). To appear in Optics Letters.

[6] A. Kwok, L. Jusinski, M. A. Krumbügel, J. N. Sweetser, D. N. Fittinghoff, and R. Trebino, "Frequency-Resolved Optical Gating Using Cascaded Second-Order Nonlinearities," IEEE Journal of Selected Topics on Quantum Electronics **4**(2), 271–277 (1998).

[7] L. Cohen, *Time-Frequency Analysis* (Prentice Hall, New Jersey, 1995).

[8] S. Yeremenko, A. Baltuška, M. Pshenichnikov, and D. Wiersma, "The Criterion of Pulse Reconstruction Quality Based on Wigner Representation," Applied Physics B **70**, S109–S117 (2000).

[9] K. W. DeLong, R. Trebino, and W. E. White, "Simultaneous Recovery of Two Ultrashort Laser Pulses from a Single Spectrogram," Journal of The Optical Society of America B **12**(12), 2463–2466 (1995).

[10] B. Seifert, H. Stolz, and M. Tasche, "Nontrivial Ambiguities for Blind Frequency-Resolved Optical Gating and The Problem of Uniqueness," Journal of The Optical Society of America B **21**(5), 1089–1097 (2004).

Chapter 8

Conclusions and Future Directions

This final chapter summarises the research work presented throughout this thesis, and presents its possible future directions.

8.1 Conclusions

Frequency-resolved optical gating is a well-established technique for the complete characterisation of ultrashort optical pulses, as reviewed in Chapter 2. The most commonly used configuration is based on the SHG interaction in bulk materials, due to its high efficiency compared to other schemes based on third-order nonlinear interactions. As shown in Chapter 3, the use of guided-wave geometry provides efficiency improvements due to tight optical confinements and long interaction lengths, whilst the QPM structure gives access to the $LiNbO_3$ highest nonlinear coefficient and guarantees a wider wavelength operation range by proper engineering of the gratings period. The properties of a QPM $LiNbO_3$ waveguide device, which was fabricated in the ORC, were presented in Chapter 4. This device was used throughout this research work.

This research work led to the first successful implementation a QPM Lithium Niobate waveguide for the FROG technique. The simultaneous complete characterisation of two ultrashort pulses of durations 4-7 ps and 25 ps in the 1.55 μm-band with a coupled energy of 430 fJ was presented in Chapter 6. The temporal walk-off between the interacting pulses in this interaction resulted in a finite acceptance bandwidth, and thus limited the temporal resolution of the measurement. As a result of this, we proposed a novel FROG configuration using cascaded SHG:DFG interactions. Theoretical and numerical analyses of this configuration in the first half of Chapter 7, based on the work in Chapter 5, revealed its robustness against the temporal walk-off effect. This configu-

ration overcomes the limited bandwidth of SFG and outperforms the efficiency of DFG. The second half of Chapter 7 shows the experimental realisation of this configuration, confirming the theoretical predictions. A 2.1 ps pulse train with a coupled average power (energy) of 72 μW (29 fJ) was successfully characterised in the experiments.

8.2 Future Directions

Several future directions from this research work can be readily envisaged. The novel FROG configuration presented in Chapter 7 can be used to characterise even shorter optical pulses, down to $\sim$ 500 fs according to our theoretical predictions, in the same device. In addition, the broad bandwidth of this configuration opens up a new possibility for the simultaneous characterisation of multiple pulses with different wavelengths, such as those in WDM systems.[1] Using SFG instead of SHG as the first step in the cascading scheme can also be beneficial, as it would allow an access to the spectral region taken by the single pump pulse in the cascaded SHG:DFG scheme.[2]

In terms of measurement sensitivity, a waveguide with a higher figure-of-merit and a lower propagation loss will definitely provide efficiency improvements. Furthermore, the use of appropriate tapering at the waveguide input/output will increase the amount of power transferred from the standard SMF. The extension of the partial characterisations of the fabrication processes presented in Section 4.3 should pave the way to a higher-quality QPM $LiNbO_3$ waveguide device.

Other interesting directions that can be taken in the future might involve implementing the FROG technique in novel devices, such as periodically- or hexagonally-poled $LiNbO_3$ slab waveguides.[3,4] Such device should have better efficiency than bulk materials, while still allowing noncollinear interactions, thus enabling sensitive measurement using the relatively simple noncollinear SHG for FROG technique. Other methods for achieving broad acceptance bandwidth in PPLN such as using pulse-front tilt and noncollinear interactions[5–7] are of particular interest for FROG applications.

References

[1] M. H. Chou, I. Brener, G. Lenz, R. Scotti, E. E. Chaban, J. Shmulovich, D. Phile, S. Kosinkski, K. R. Parameswaran, and M. M. Fejer, "Efficient Wide-Band and Tunable Midspan Spectral Inverter Using Cascaded Nonlinearitiess in $LiNbO_3$ Waveguides," IEEE Photonics Technology Letters **12**(1), 82–84 (2000).

[2] C. Q. Xu and B. Chen, "Cascaded Wavelength Conversions Based on Sum-Frequency Generation and Difference-Frequency Generation," Optics Letters **29**(3), 292–294 (2004).

[3] N. G. R. Broderick, G. W. Ross, H. L. Offerhaus, D. J. Richardson, and D. C. Hanna, "Hexagonally Poled Lithium Niobate: A Two-Dimensional Nonlinear Photonic Crystal," Physical Review Letters **84**(19), 4345–4348 (2000).

[4] K. Gallo, R. T. Bratfalean, A. C. Peacock, N. G. R. Broderick, C. B. E. Gawith, L. Ming, P. G. R. Smith, and D. J. Richardson, "Second-Harmonic Generation in Hexagonally-Poled Lithium Niobate Slab Waveguides," Electronics Letters **39**(1), 75–76 (2003).

[5] S. Ashihara, T. Shimura, and K. Kuroda, "Group-Velocity Matched Second-Harmonic Generation in Tilted Quasi-Phase-Matched Gratings," Journal of the Optical Society of America B **20**(5), 853–856 (2003).

[6] N. Fujioka, S. Ashihara, H. Ono, T. Shimura, and K. Kuroda, "Group-Velocity-Matched Noncollinear Second-Harmonic Generation in Quasi-Phase-Matching," Journal of the Optical Society of America B **22**(6), 1283–1289 (2005).

[7] A. M. Schober, M. Carbonneau-Lefort, and M. M. Fejer, "Broadband Quasi-Phase-Matched Second-Harmonic Generation of Ultrashort Optical Pulses with Spectral Angular Dispersion," Journal of the Optical Society of America B **22**(8), 1699–1713 (2005).

Appendix A

Coupled Mode Equations for Three-Wave Mixing

In this appendix, the coupled-mode equations for three-wave mixing in a QPM $LiNbO_3$ waveguide device is derived. We shall start our journey with the following wave equation derived from Maxwell's equations:

$$\nabla \times \nabla \times \mathbf{E}(\mathbf{r},t) + \frac{1}{c^2}\frac{\partial^2 \mathbf{E}(\mathbf{r},t)}{\partial t^2} = -\mu_0 \frac{\partial^2 \mathbf{P}(\mathbf{r},t)}{\partial t^2}. \tag{A.1}$$

It is often useful to separate the rapidly varying part of the electric and polarisation fields by writing:

$$\mathbf{E}(\mathbf{r},t) = \sum_j \mathbf{E}_j(\mathbf{r},t)\exp\left[-i\omega_j t\right] + \text{c.c.} \tag{A.2a}$$

$$\mathbf{P}(\mathbf{r},t) = \sum_j \mathbf{P}_j(\mathbf{r},t)\exp\left[-i\omega_j t\right] + \text{c.c}, \tag{A.2b}$$

where ω_j is the carrier frequency of the interacting waves. Fourier transform of the electric field $\mathbf{E}(\mathbf{r},t)$ is given by:

$$\begin{aligned}\mathcal{F}\left[\mathbf{E}(\mathbf{r},t)\right] = \mathbf{E}(\mathbf{r},\omega) &= \frac{1}{2\pi}\int_{-\infty}^{\infty}\mathbf{E}(\mathbf{r},t)\exp\left(i\omega t\right)dt \\ &= \frac{1}{2\pi}\sum_j\int_{-\infty}^{\infty}\mathbf{E}_j(\mathbf{r},t)\exp\left(i\Omega_j t\right)dt \\ &= \sum_j \mathbf{E}_j(\mathbf{r},\Omega_j),\end{aligned} \tag{A.3}$$

where $\Omega_j = \omega - \omega_j$ is the frequency detuning coordinate, and $\Omega_j \ll \omega_j$. Hence, we can rewrite the electric field as an inverse Fourier transform as follows:

$$\begin{aligned}\mathbf{E}(\mathbf{r},t) &= \sum_j \int_{-\infty}^{\infty} \mathbf{E}_j(\mathbf{r},\Omega_j)\exp(-i\omega t)dt \\ &= \sum_j \int_{-\infty}^{\infty} \mathbf{E}_j(\mathbf{r},\Omega_j)\exp[-i(\Omega_j+\omega_j)t]dt.\end{aligned} \tag{A.4}$$

Substituting the above equation into Eq. (A.1) results in:

$$\sum_j \left[\nabla\times\nabla\times\hat{\mathbf{E}}_j(\mathbf{r},\Omega_j) - \frac{(\Omega_j+\omega_j)^2}{c^2}\hat{\mathbf{E}}_j(\mathbf{r},\Omega_j)\right] = \sum_j \mu_0(\Omega_j+\omega_j)^2\hat{\mathbf{P}}_j(\mathbf{r},\Omega_j). \tag{A.5}$$

Separation of $\mathbf{P}$ into the linear and nonlinear part, i.e. $\mathbf{P} = \mathbf{P}^{\mathrm{L}} + \mathbf{P}^{\mathrm{NL}}$, results in

$$\sum_j \left[\nabla\times\nabla\times\hat{\mathbf{E}}(\mathbf{r},\Omega_j) - \frac{(\Omega_j+\omega_j)^2}{c^2}\varepsilon(x,y,\omega)\hat{\mathbf{E}}(\mathbf{r},\Omega_j)\right] = \sum_j \mu_0(\Omega_j+\omega_j)^2\hat{\mathbf{P}}^{\mathrm{NL}}(\mathbf{r},\Omega_j), \tag{A.6}$$

where $\varepsilon(x,y,\omega) = 1+\chi^{(1)}(x,y,\omega)$ is the relative permittivity of the waveguide structure. We will omit the subscript j in writing the equations whenever it is clear what the notations refer to.

We can rewrite the first term on the left-hand-side (LHS) of Eq. (A.6) as:

$$\nabla\times\nabla\times\hat{\mathbf{E}}(\mathbf{r},\Omega_j) = \nabla\left[\nabla\cdot\hat{\mathbf{E}}(\mathbf{r},\Omega_j)\right] - \nabla^2\hat{\mathbf{E}}(\mathbf{r},\Omega_j). \tag{A.7}$$

The first term can be readily evaluated from Eq. (3.1a), which in the absence of free charge, simply becomes

$$\nabla\cdot\hat{\mathbf{D}} = 0. \tag{A.8}$$

Utilising the constitutive relation [Eq. (3.2a)], the above expression can be recast as

$$\nabla\varepsilon\cdot\hat{\mathbf{E}} + \varepsilon\nabla\cdot\hat{\mathbf{E}} = 0. \tag{A.9}$$

For waveguides with a graded refractive index profile and a small refractive index increase, its derivative is negligible, i.e. $\nabla\varepsilon \approx 0$. Naturally, it follows that $\nabla\cdot\hat{\mathbf{E}} = 0$, such that Eq. (A.6) can be rewritten as follows

$$\sum_j \left[\nabla^2\hat{\mathbf{E}}(\mathbf{r},\Omega_j) + \frac{(\Omega_j+\omega_j)^2}{c^2}\varepsilon(x,y,\omega)\hat{\mathbf{E}}(\mathbf{r},\Omega_j)\right] = -\sum_j \mu_0(\Omega_j+\omega_j)^2\mathbf{P}_j^{\mathrm{NL}}(\mathbf{r},\Omega_j). \tag{A.10}$$

We can consider Eq. (A.10) as a linear wave equation (LHS only) with a nonlinear perturbation on the right-hand-side (RHS). We shall first find the solution for the linear part for a single frequency:

$$\nabla^2\mathbf{E}(\mathbf{r},\Omega_j)+\frac{(\Omega_j+\omega_j)^2}{c^2}\varepsilon(x,y,\omega)\mathbf{E}(\mathbf{r},\Omega_j)=0. \tag{A.11}$$

Since the waveguide structures we consider are symmetric along the $z-$coordinate, it is logical to solve the above equation via the separation of variables method and assume the following solution:

$$\hat{\mathbf{E}}(\mathbf{r},\Omega_j)=\mathbf{F}(x,y)\hat{\mathcal{A}}(z,\Omega_j). \tag{A.12}$$

Substitution of the above equation into the LHS of Eq. (A.10) yields the following two equations:

$$\left[\frac{\partial^2}{\partial x^2}+\frac{\partial^2}{\partial y^2}\right]\mathbf{F}(x,y)+\left[\frac{(\Omega_j+\omega_j)^2\varepsilon(x,y,\omega)}{c^2}-\beta^2(\omega)\right]\mathbf{F}(x,y)=0, \tag{A.13a}$$

$$\frac{\partial^2\hat{\mathcal{A}}(z,\Omega_j)}{\partial z^2}+\beta^2(\omega)\hat{\mathcal{A}}(z,\Omega_j)=0, \tag{A.13b}$$

with β being the separation of variable constant. The first of the above expression [Eq. (A.13a)] can be readily identified as the eigenvalue equation for the guided-wave mode profile. In such a structure, the electromagnetic radiation cannot travel freely, but exists as discrete entities $\mathbf{F}_q(x,y)$, with a propagation wavevector $\beta_q(\omega)$. Since the electromagnetic waves interact via nonlinear interaction, their envelope varies during propagation. It is then useful to separate the rapidly varying part of the amplitude as:

$$\hat{\mathcal{A}}(z,\Omega_j)=\hat{A}(z,\Omega_j)\exp\left[\pm i\beta(\omega_j)z\right], \tag{A.14}$$

where $\hat{A}(z,\Omega)$ is a slowly varying amplitude, and the plus-minus sign identifies the forward and backward propagating waves, respectively. Selecting the forward propagating wave and substituting the above solution into Eq. (A.13b) result in

$$\left\{\frac{\partial^2\hat{A}(z,\Omega_j)}{\partial z^2}+2i\beta(\omega_j)\frac{\partial\hat{A}(z,\Omega_j)}{\partial z}+\left[\beta^2(\omega)-\beta^2(\omega_j)\right]\hat{A}(z,\Omega_j)\right\}\exp\left[i\beta(\omega_j)z\right]=0. \tag{A.15}$$

We can expand the propagation wavevector $\beta(\omega)$ around the frequency ω_j as (see section 5.1):

$$\beta(\omega)=\beta(\omega_j)+\Omega_j\frac{1}{u_j}+\frac{1}{2}\Omega_j^2 b_j+\ldots, \tag{A.16}$$

such that the factor $\left[\beta^2(\omega) - \beta^2(\omega_j)\right]$ can be approximated as:

$$\left[\beta^2(\omega) - \beta^2(\omega_j)\right] = \left[\beta(\omega) - \beta(\omega_j)\right]\left[\beta(\omega) + \beta(\omega_j)\right] \approx 2\beta(\omega_j)\left[\Omega_j \frac{1}{u_j} + \frac{1}{2}\Omega_j^2 b_j\right]. \quad \text{(A.17)}$$

Next, by utilising the slowly-varying amplitude approximation:

$$\frac{\partial^2 \hat{A}(z,\omega)}{\partial z^2} \ll \left|\beta(\omega_j)\frac{\partial \hat{A}(z,\omega)}{\partial z}\right|, \quad \text{(A.18)}$$

Eq. (A.15) can be rewritten as:

$$\left\{ i\frac{\partial \hat{A}(z,\Omega_j)}{\partial z} + \left[\Omega_j \frac{1}{u_j} + \frac{1}{2}\Omega_j^2 b_j\right]\hat{A}(z,\Omega_j)\right\} 2\beta(\omega_j)\exp\left[i\beta(\omega_j)z\right] = 0. \quad \text{(A.19)}$$

Hence, we can rewrite the complete electric-field solution as follows:

$$\mathbf{E}(\mathbf{r},t) = \sum_q \sum_{j=1}^{3} C_j^{(q)} \mathbf{F}_j^{(q)}(x,y) A_j^{(q)}(z,t) \exp\left[i(\beta_j^{(q)} z - \omega_j t)\right] + \text{c.c}, \quad \text{(A.20)}$$

where we consider three interacting waves at distinct frequencies that satisfy $\omega_3 = \omega_1 + \omega_2$ or $\Omega_3 = \Omega_1 + \Omega_2$, $A_q^{(j)}(z,t) \in \mathbb{C}$ is a slowly-varying amplitude both in time and space, ω_j is the angular frequency, $\beta_j^{(q)} = \beta^{(q)}(\omega_j)$ is the propagation wavevector of mode number q in the waveguide, and $C_q^{(j)}$ is a normalisation constant such that

$$\frac{1}{2}\int_{x,y} \text{Re}\left[(\mathbf{E} \times \mathbf{H}^*) \cdot \hat{z}\right] dxdy = \mathcal{P}(z,t) = |A(z,t)|^2. \quad \text{(A.21)}$$

Evaluation of the above normalisation results in

$$C_j^{(q)} = \left[\frac{2\omega_j \mu_0}{\beta_j^{(q)} \int_{x,y} \left|\mathbf{F}^{(q)}(x,y)\right|^2 dxdy}\right]^{\frac{1}{2}}, \quad \text{(A.22)}$$

where the orthogonality of the mode profiles have been used:

$$\int_{x,y} \mathbf{F}^{(q)}(x,y) \cdot \left[\mathbf{F}^{(r)}(x,y)\right]^* dxdy \propto \delta_{qr}, \quad \text{(A.23)}$$

with δ_{qr} being a Kronecker delta function.

Having simplified the linear part of Eq. (A.10) to Eq. (A.19), we now evaluate the nonlinear term on the right-hand-side (RHS) of Eq. (A.10). The second-order nonlinear interaction that take place in the QPM $LiNbO_3$ waveguide device have been chosen in such a way to exploit d_{33}, the largest nonlinear coefficient of $LiNbO_3$. Therefore, the polarisations of the input waves must be parallel to the $z-$axis of $LiNbO_3$. The RHS of

Eq. (A.10) in frequency domain can be written explicitly for the polarisation wave at a frequency ω_3 as follows:

$$\mu_0\omega_3^2\mathbf{P}_3^{\mathrm{NL}}(\mathbf{r},\Omega_3) = \hat{\mathbf{x}}\frac{4d\omega_3^2}{c^2}\int_{-\infty}^{\infty} E_1(\mathbf{r},\Omega_1)E_2(\mathbf{r},\Omega_3-\Omega_1)d\Omega_1, \tag{A.24}$$

where we have used the relation $\Omega_2 = \Omega_3 - \Omega_1$, and the fact that $\Omega_3 \ll \omega_3$, in writing the above relation. Substituting the full electric-field solution [Eq. (A.20)] into the above equation yields

$$\begin{aligned}\mu_0\omega_3^2\mathbf{P}_3^{\mathrm{NL}}(\mathbf{r},\Omega_3) = \hat{\mathbf{x}}\frac{4d\omega_3^2}{c^2}\sum_{q,r}\left|\mathbf{F}_1^{(q)}(x,y)\right|\left|\mathbf{F}_2^{(r)}(x,y)\right| C_q^{(1)}C_2^{(r)} \\ \times\exp\left[i(\beta_1^{(q)}+\beta_2^{(r)})z\right]\int_{-\infty}^{\infty}\hat{A}_1^{(q)}(\mathbf{r},\Omega_1)\hat{A}_2^{(r)}(\mathbf{r},\Omega_3-\Omega_1)d\Omega_1,\end{aligned} \tag{A.25}$$

We can combine the evaluated linear and nonlinear parts of Eq. (A.10), Eq. (A.19) and Eq. (A.25), respectively, to yield the following equation for the wave at a central frequency ω_3:

$$\begin{aligned}\sum_q\left\{i\frac{\partial\hat{A}_3^{(q)}(z,\Omega_3)}{\partial z}+\left[\Omega_3\frac{1}{u_3}+\frac{1}{2}\Omega_3^2 b_3\right]\hat{A}_3^{(q)}(z,\Omega_3)\right\}\left|\mathbf{F}_3^{(q)}(x,y)\right| \\ = \frac{2d\omega_3^2}{\beta_3^{(q)}c^2}\sum_{q,r}\left|\mathbf{F}_1^{(q)}(x,y)\right|\left|\mathbf{F}_2^{(r)}(x,y)\right|\frac{C_1^{(q)}C_2^{(r)}}{C_3^{(q)}}\exp\left[i(\beta_1^{(q)}+\beta_2^{(r)}-\beta_3^{(q)})z\right] \\ \times\int_{-\infty}^{\infty}\hat{A}_1^{(q)}(\mathbf{r},\Omega_1)\hat{A}_2^{(r)}(\mathbf{r},\Omega_3-\Omega_1)d\Omega_1.\end{aligned} \tag{A.26}$$

Multiplying both sides of the above equation with $\left|\mathbf{F}_q^{(3)}(x,y)\right|$ and performing the integral over the $(x,y)-$surface result in

$$\begin{aligned}\frac{\partial\hat{A}_3(z,\Omega_3)}{\partial z}-i\left[\Omega_3\frac{1}{u_3}+\frac{1}{2}\Omega_3^2 b_3\right]\hat{A}_3(z,\Omega_3) \\ = 2i\omega_3\kappa\exp\left[-i\Delta\beta_0 z\right]\int_{-\infty}^{\infty}\hat{A}_1(\mathbf{r},\Omega_1)\hat{A}_2(\mathbf{r},\Omega_3-\Omega_1)d\Omega_1,\end{aligned} \tag{A.27}$$

where

$$\Delta\beta_0 = \beta_3 - \beta_1 - \beta_2 \tag{A.28}$$

is the central frequencies wavevector mismatch, and κ is the nonlinear coupling coefficient, given by

$$\kappa = d\sqrt{\frac{2\mu_0}{\mathcal{N}(\omega_1)\mathcal{N}(\omega_2)\mathcal{N}(\omega_3)c}}\sqrt{\frac{1}{S_{\mathrm{ovl}}}}, \tag{A.29}$$

with $\mathcal{N}$ being the effective index of certain modes of the waveguide, and

$$S_{\text{ovl}} = \frac{\int |\mathbf{F}_1|^2 \, dxdy \int |\mathbf{F}_2|^2 \, dxdy \int |\mathbf{F}_3|^2 \, dxdy}{\left(\int |\mathbf{F}_1| \, |\mathbf{F}_2| \, |\mathbf{F}_3| \, dxdy\right)^2} \tag{A.30}$$

being called the area overlap.

In writing Eq. (A.27), we assumed that the interaction is between fundamental modes, and thus have omitted the mode indices q, for two reasons. First, each discrete propagating mode satisfies different phase-matching conditions due to chromatic dispersion, so that we may consider them separately. Second, the expression of the area overlap [Eq. (A.30)] tells us that the highest coupling coefficient is obtained from interaction between fundamental modes. We now perform an inverse Fourier transform on Eq. (A.27) to yield:

$$\frac{\partial A_3}{\partial z} + \frac{1}{u_3}\frac{\partial A_3}{\partial t} + i\frac{b_3}{2}\frac{\partial^2 A_3}{\partial t^2} = 2i\omega_3 \kappa A_1 A_2 \, \exp\left[-i\Delta\beta_0 z\right]. \tag{A.31}$$

Following similar derivations for the waves at frequencies ω_1 and ω_2 yield the other two coupled-mode equations:

$$\frac{\partial A_1}{\partial z} + \frac{1}{u_1}\frac{\partial A_1}{\partial t} + i\frac{b_1}{2}\frac{\partial^2 A_1}{\partial t^2} = 2i\omega_1 \kappa A_2^* A_3 \, \exp\left[i\Delta\beta_0 z\right], \tag{A.32a}$$

$$\frac{\partial A_2}{\partial z} + \frac{1}{u_2}\frac{\partial A_2}{\partial t} + i\frac{b_2}{2}\frac{\partial^2 A_2}{\partial t^2} = 2i\omega_2 \kappa A_1^* A_3 \, \exp\left[i\Delta\beta_0 z\right], \tag{A.32b}$$

concluding the derivation of the coupled-mode equations for three-wave mixing.

Appendix B

List of Publications

B.1 Journal Publications

1. J. Prawiharjo, F. Parmigiani, K. Gallo, P. Petropoulos, N. G. R. Broderick, and D. J. Richardson, "Cascaded $\chi^{(2)}$ Interaction Frequency-Resolved Optical Gating in a Periodically-Poled Lithium Niobate Waveguide," (2005). To appear in Optics Letters.

2. J. Prawiharjo, K. Gallo, N. G. R. Broderick, and D. J. Richardson, "Frequency-Resolved Optical Gating in the 1.55 μm-Band Via Cascaded $\chi^{(2)}$ Processes," Journal of the Optical Society of America B **22**(9), 1985–1993 (2005).

3. J. Prawiharjo, K. Gallo, B. C. Thomsen, M. A. F. Roelens, P. J. Almeida, N. G. R. Broderick, and D. J. Richardson, "Frequency Resolved Optical Gating in a Quasi-Phase-Matched $LiNbO_3$," IEEE Photonics Technology Letters **17**(4), 849–851 (2005).

B.2 Conference Publications

1. J. Prawiharjo, F. Parmigiani, K. Gallo, P. Petropoulos, N. G. R. Broderick, and D. J. Richardson, "A Novel High-Resolution and High-Sensitivity FROG Configuration Based on Cascaded $\chi^{(2)}$ Interactions in a PPLN Waveguide," PDE-5, IQEC/CLEO Pacific Rim 2005, Tokyo, 11-15 July 2005 (Postdeadline)

2. J. Prawiharjo, K. Gallo, N. G. R. Broderick, and D. J. Richardson, "Frequency-Resolved Optical Gating in the 1.55 μm-Band via Cascaded $\chi^{(2)}$ Interactions," QWL2-1, IQEC/CLEO Pacific Rim 2005, Tokyo, 11-15 July 2005

3. J. Prawiharjo, K. Gallo, B. C. Thomsen, M. A. F. Roelens, P. J. Almeida, N. G. R. Broderick, and D. J. Richardson, "Blind-FROG in a Quasi-Phase-Matched $LiNbO_3$ Waveguide," JWA34, OFC 2005, Anaheim, 6-11 March 2005

4. J. Prawiharjo, K. Gallo, B. C. Thomsen, N. G. R. Broderick, and D. J. Richardson, "Optical Waveform Measurement Using a Waveguide Quasi-Phase-Matched Sum-Frequency-Generation Device," Summer School: New Concepts in Photonics and Optical Communications, Dijon, 21-25 June 2004

5. J Prawiharjo, K. Gallo, B. C. Thomsen, N. G. Broderick, and D. J. Richardson, "Optical Waveform Measurement Using a Waveguide Quasi-Phase-Matched Sum-Frequency-Generation Device," IoP: Nonlinear Optics in Communications, London, 30 June 2004

6. K. Gallo, J. Prawiharjo, N. G. R. Broderick, and D. J. Richardson, "Proton-Exchanged Waveguides for Photonic Applications in Lithium Niobate," ICTON 2004, Wroclaw, 4-8 July 2004 (Invited)

7. K. Gallo, C. B. E. Gawith, J. Prawiharjo, N. G. R. Broderick, P. G. R. Smith, S. Mailis, R. W. Eason, and D. J. Richardson, "UV-Written Channel Waveguides in Proton-Exchanged Lithium Niobate," CTuF, CLEO/IQEC 2004, San Francisco, 16-21 May 2004